

# **Use of Active Power Filter to Reduce the Effects of Harmonics in Solid Oxide Fuel Cells**

by

© Aparna Biswas, B.Tech.

A Thesis submitted to the  
School of Graduate Studies  
in partial fulfillment of the  
requirements for the degree of  
Master of Engineering

Faculty of Engineering and Applied Science  
Memorial University of Newfoundland

May 2016

St. John's, Newfoundland, Canada

# Abstract

The Solid Oxide Fuel Cell (SOFC) is a class of fuel cells that is capable of generating very high levels of power at high temperatures. SOFCs are used for stationary power generation and as Combined Heat and Power (CHP) systems. In spite of all the beneficial features of the SOFC, the propagation of ripple currents, due to nonlinear loads, is a challenging problem, as it interferes with the physical operation of the fuel cell.

The purpose of this thesis is to identify the cause of ripples and attempt to eliminate or reduce the ripple propagation through the use of Active Power Filters (APF). To this end, a systematic approach to modeling the fuel cell to account for its nonlinear behavior in the presence of current ripples is presented. A model of a small fuel cell power system which consists of a fuel cell, a DC-DC converter, a single-phase inverter and a nonlinear load is developed in MATLAB/Simulink environment. The extent of ripple propagation, due to variations in load magnitude and frequency, are identified using frequency spectrum analysis. In order to reduce the effects of ripple propagation, an APF is modeled to remove ripples from the DC fuel cell current. The emphasis of this thesis is based on the idea that small fuel cell systems cannot implement large passive filters to cancel the effects of ripple propagation and hence, the compact APF topology effectively protects the fuel cell from propagating ripples and improves its electrical performance.

# Acknowledgement

I would like to express my sincere gratitude to my supervisor, Dr. John Quaiocoe for his invaluable guidance without which this work could not have been completed.

I would also like to thank NSERC for financially investing in this research.

Finally, I would like to thank, Dr. Leonard Lye, Associate Dean of Graduate Studies, Ms. Moya Crocker, Secretary to the Associate Dean of Graduate Studies and Ms. Colleen Mahoney, Academic Program Assistant from the Office of the Associate Dean (Graduate) for their kind support in ensuring smooth operation of administrative aspects for my master's program.

# Table of Contents

<b>List of Figures</b>	<b>vi</b>
<b>List of Tables</b>	<b>x</b>
<b>List of Abbreviation</b>	<b>xi</b>
<b>List of Symbols</b>	<b>xii</b>
<b>1 Introduction</b> .....	<b>1</b>
1.1 Thesis Objectives.....	2
1.2 Thesis Organization.....	3
<b>2 Introduction to Fuel Cells and Literature Review</b> .....	<b>4</b>
2.1 Types of Fuel Cells.....	5
2.2 Types of Fuel Cell Models.....	8
2.3 Literature Review.....	9
2.4 Summary.....	12
<b>3 Fuel Cell Modeling</b> .....	<b>13</b>
3.1 Classical Approach to Fuel Cell Modeling.....	15
3.2 Fuel Cell Model Based on Equivalent Circuit.....	18
3.2.1 Maximum Voltage.....	20
3.2.2 Maximum Current Density.....	20

3.2.3	Fuel Utilization Rate.....	20
3.2.4	Area Specific Ionic Resistance.....	20
3.2.5	Area Specific Electronic Resistance.....	21
3.3	DC Properties of Fuel Cell.....	22
3.4	AC Properties of Fuel Cell.....	26
3.4.1	Double-layer Capacitance.....	26
3.4.2	Behaviour of Fuel Cell with Ripple Current.....	30
3.5	Summary.....	33
<b>4</b>	<b>Ripple Analysis of Solid Oxide Fuel Cell (SOFC).....</b>	<b>34</b>
4.1	Fuel Cell Power System.....	35
4.1.1	Stacked SOFC .....	35
4.1.2	SOFC Power Circuit.....	35
4.1.3	DC-DC Boost Converter.....	36
4.1.4	Inverter.....	39
4.1.5	Full-Bridge Diode Rectifier.....	43
4.2	Performance of the Fuel Cell System.....	44
4.2.1	The Fuel Cell System under Resistive Load.....	44
4.2.2	The Fuel Cell System under Nonlinear Load.....	48
4.3	Effect of Varying Load.....	53
4.3.1	Magnitude Variation.....	53
4.3.1.1	Load Value of 240 W.....	53
4.3.1.2	Load Value of 400 W.....	57
4.3.2	Frequency Variation.....	61
4.3.2.1	Frequency of 120 Hz.....	62
4.3.2.2	Frequency of 240 Hz.....	66
4.4	Summary.....	71
<b>5</b>	<b>Fuel Cell System with Active Power Filter (APF).....</b>	<b>72</b>
5.1	Introduction to Active Power Filters.....	73
5.1.1	Series APF.....	75

5.1.2	Shunt APF.....	75
5.1.3	Hybrid APF.....	75
5.1.4	Modified Shunt Active Power Filter.....	76
5.2	The APF Converter Topology.....	77
5.3	Generation of Switching Signal.....	79
5.4	Harmonic Extraction.....	81
5.5	Implementation of the Modified Shunt APF.....	84
5.5.1	Load Value of 160 Watts.....	87
5.5.2	Load Value of 240 Watts.....	92
5.5.3	Load Value of 400 Watts.....	97
5.6	Summary.....	103
<b>6</b>	<b>Conclusion.....</b>	<b>104</b>
6.1	Original Contribution.....	105
6.2	Future Work.....	106
	<b>References.....</b>	<b>108</b>
	<b>Appendix.....</b>	<b>116</b>
<b>A</b>	<b>SOFC Design Parameters.....</b>	<b>116</b>
<b>B</b>	<b>MATLAB Code for Single Cell SOFC at 800°C.....</b>	<b>118</b>
<b>C</b>	<b>Simulink Screenshots.....</b>	<b>120</b>
C.1	Simulink Simulation Parameters.....	120
C.2	DC-DC Boost Converter.....	121
C.3	Inverter.....	122
C.4	Full-bridge Diode Rectifier.....	123
C.5	Modified Shunt APF Converter.....	124
C.6	Fuel Cell Power System with Implemented Modified Shunt APF .....	125

# List of Figures

3.1	Generalized Solid Oxide Fuel Cell Structure.....	14
3.2	Fuel Cell Polarization Curve.....	16
3.3	SOFC Equivalent Electrical Circuit.....	18
3.4 (a)	Polarization Curve of SOFC at 800°C.....	23
3.4 (b)	Power Density Curve of SOFC at 800°C.....	23
3.5 (a)	Polarization Curve of SOFC at Three Different Temperatures.....	25
3.5 (b)	Power Density Curve of SOFC at Three Different Temperatures.....	25
3.6	Equivalent Fuel Cell Circuit Inclusive of Double-layer Capacitance.....	29
3.7	Polarization Curve of SOFC under Three Different Ripple Frequencies.....	31
3.8	Effects of Current Ripple on Power Extraction.....	32
4.1	Circuit for Ripple Analysis.....	36
4.2	DC-DC Boost Converter.....	37
4.3	Definition of Duty Ratio.....	37
4.4	Single-phase Full Bridge Inverter.....	40
4.5	The Fuel Cell System with a Resistive Load.....	44
4.6 (a)	Voltage Waveforms under Resistive Load of 160 W.....	46

4.6 (b)	Current Waveforms under Resistive Load of 160 W.....	47
4.7	Harmonic Analysis of Fuel Cell Current under Resistive Load.....	48
4.8 (a)	Voltage Waveforms under Nonlinear Load of 160 W.....	50
4.8 (b)	Current Waveforms under Nonlinear Load of 160 W.....	51
4.9	Harmonic Analysis of Fuel Cell Current under Nonlinear Load of 160 W.....	52
4.10 (a)	Voltage Waveforms under Nonlinear Load of 240 W.....	54
4.10 (b)	Current Waveforms under Nonlinear Load of 240 W.....	55
4.11	Harmonic Analysis of Fuel Cell Current under Nonlinear Load of 240 W.....	57
4.12 (a)	Voltage Waveforms under Nonlinear Load of 400 W.....	58
4.12 (b)	Current Waveforms under Nonlinear Load of 400 W.....	59
4.13	Harmonic Analysis of Fuel Cell Current under Nonlinear Load of 400 W.....	60
4.14 (a)	Voltage Waveforms at Inverter Operating at 120 Hz under Nonlinear Load of 160 W.....	63
4.14 (b)	Current Waveforms at Inverter Operating at 120 Hz under Nonlinear Load of 160 W.....	64
4.15	Harmonic Analysis of Fuel Cell Current under Nonlinear Load of 160 W and Operated at 120 Hz.....	65
4.16 (a)	Voltage Waveforms at Inverter Operating at 240 Hz under Nonlinear Load of 160 W.....	67
4.16 (b)	Current Waveforms at Inverter Operating at 240 Hz under Nonlinear Load of 160 W.....	68
4.17	Harmonic Analysis of Fuel Cell Current under Nonlinear Load of 160 W and Operated at 240 Hz.....	69

5.1	Various Active Power Filter Topologies.....	74
5.2	Modified Shunt Active Power Filter Circuit.....	78
5.3	Principle of Hysteresis Current Control.....	80
5.4	Structure of Hysteresis Current Controller.....	80
5.5	Algorithm for Harmonic Extraction.....	83
5.6	Extracted Harmonic Waveform from Fuel Cell Current under Nonlinear load of 160 W, 60 Hz.....	84
5.7	Fuel Cell System with Modified Shunt Active Filter.....	85
5.8	Extracted Fuel Cell Harmonic Current and Modified Shunt APF Current Output under nonlinear load of 160 Watts, 60 Hz.....	86
5.9 (a)	Voltage Waveforms under Nonlinear Load of 160 W after APF Implementation.....	88
5.9 (b)	Current Waveforms under Nonlinear Load of 160 W after APF Implementation.....	89
5.10	Harmonic Analysis of Fuel Cell Current under Nonlinear Load of 160 W.....	91
5.11 (a)	Voltage Waveforms under Nonlinear Load of 240 W after APF Implementation.....	93
5.11 (b)	Current Waveforms under Nonlinear Load of 240 W after APF Implementation.....	94
5.12	Harmonic Analysis of Fuel Cell Current under Nonlinear Load of 240 W.....	96
5.13 (a)	Voltage Waveforms under Nonlinear Load of 400 W after APF Implementation.....	98

5.13 (b)	Current Waveforms under Nonlinear Load of 400 W after APF Implementation.....	99
5.14	Harmonic Analysis of Fuel Cell Current under Nonlinear Load of 400 W.....	101
C.1	Simulink Schematic of DC-DC Boost Converter.....	121
C.2	Simulink Schematic of Single-phase Full-Bridge Inverter.....	122
C.3	Simulink Schematic of Full-Bridge Diode Rectifier.....	123
C.4	Simulink Schematic of Modified Shunt APF Converter.....	124
C.5	Simulink Schematic of Fuel Cell System with Implemented Modified Shunt APF.....	125

# List of Tables

2.1	Classification of Fuel Cells.....	6
4.1	DC-DC Boost Converter Parameters.....	39
4.2	Inverter Parameters.....	43
4.3	Nonlinear Load Parameters.....	43
4.4	DC and Second Harmonic Magnitudes of Fuel Cell Current under Three Nonlinear Loads.....	61
4.5	DC and Second Harmonic Magnitudes of Fuel Cell Current for Three Inverter Switching Frequencies.....	70
5.1	Modified Shunt APF Parameters.....	84
5.2	Harmonic Comparison Before and After APF Implementation for Three Nonlinear Load Conditions.....	102
A.1	YSZ Parameters.....	117
C.1	Simulink Solver Parameters.....	120

# List of Abbreviations

AC	Alternating Current
AFC	Alkaline Fuel Cell
APF	Active Power Filter
CHP	Combined Heat and Power System
DC	Direct Current
DMFC	Direct Methanol Fuel Cell
IGBT	Insulated Gate Bipolar Transistor
LC	Inductor Capacitor
MCFC	Molten Carbonate Fuel Cell
NSERC	National Science and Engineering Research Council of Canada
PAFC	Phosphoric Acid Fuel Cell
PEMFC	Proton Exchange Membrane Fuel Cell
PWM	Pulse Width Modulation
RC	Resistor Capacitor
SOFC	Solid Oxide Fuel Cell
SPWM	Sinusoidal Pulse Width Modulation

# List of Symbols

$\alpha$	Coefficient of Charge Transfer
$A$	Thermodynamic Coefficient
$A_{cell}$	Total Surface Area of Fuel Cell (Single Cell)
$A_e$	Surface Area of Electrode
$C$	Capacitance for Modified Shunt APF
$C_{APF}$	Modified Shunt APF Filter Capacitor
$C_b$	Triple-phase Boundary
$C_{DC}$	DC-DC Boost Converter Capacitor
$C_{GC}$	Gouy-Chapman Capacitance
$C_H$	Hemholtz Capacitance
$C_f$	Inverter Filter Capacitor
$C_{Load}$	Load Capacitor
$C_O$	Double-layer Capacitance
$C_\infty$	Bulk Concentration of Reactants
$\Delta I_2$	Estimated Boost Converter Output Ripple Current
$\Delta V_2$	Desired Boost Converter Output Ripple Voltage
$d$	DC-DC Boost Converter Duty Cycle
$D$	Diode
$\delta_a$	Thickness of Anode
$\delta_c$	Thickness of Cathode

$\delta_e$	Thickness of Electrolyte
$d_e$	Distance Between Electrodes
$\varepsilon$	Electrical Permittivity
$e$	Elementary Charge
$E$	Fuel Cell Load Voltage (Single Cell)
$E_C$	Double-layer Capacitive Voltage
$E_{Final}$	Fuel Cell Voltage Inclusive of Double-layer Capacitance (Single Cell)
$e_{hcc}$	Error Signal used in Hysteresis Current Control
$E_{max}$	Nernst Voltage
$E_{OCV}$	Open Circuit Voltage of Fuel Cell (Single Cell)
$E_0$	Thermodynamic Coefficient
$E_{SOFC}$	Fuel Cell Voltage Inclusive of All Losses (Single Cell)
$\phi$	Phase Difference Between Inverter Output Voltage and Output Current
$F$	Faraday's Constant
$f_{DC}$	Boost Converter Switching Frequency
$f_{ripple}$	Ripple Frequency
$\eta_{act}$	Activation Loss Voltage
$\eta_{con}$	Concentration Loss Voltage
$\eta_f$	Fuel Utilization Factor
$\eta_{ohm}$	Ohmic Loss Voltage
$i$	Actual Fuel Cell Current (Single Cell)
$i_1$	Fuel Cell Current
$i_2$	DC-DC Boost Converter Output Current
$i_3$	Inverter Output Current Before LC Filter
$i_4$	Inverter Output Current After LC Filter
$i_{APF}$	APF Output Current
$I_{max}$	Maximum Current Density Developed on Electrodes
$i_o$	Exchange Current
$i_r$	Current Reference for Hysteresis Current Control

$i_{ripple}$	Fuel Cell Ripple Current (Single Cell)
$i_s$	Second Harmonic Signal of Fuel Cell Current
$I_x$	Magnitude of Fuel Cell Second Harmonic
$K$	Chemical Equilibrium Constant
$k_B$	Boltzmann's Constant
$L_{APF}$	Modified Shunt APF Filter Inductor
$L_{DC}$	DC-DC Boost Converter Inductor
$L_f$	Inverter Filter Inductor
$n$	Number of moles of electrons transferred
$p_{H_2}$	Partial Pressure of Fuel
$p_{H_2O}$	Partial Pressure of Residual Water
$p_{O_2}^{1/2}$	Partial Pressure of Oxygen
$p_{ref}^{1/2}$	Referral Partial Pressure
$Q$	IGBT Switch
$R$	Gas Constant
$R_1$	Area Specific Ionic Resistance Due to Electrolyte and Electrode
$R_2$	Area Specific Electronic Resistance Due to Electrolyte and Electrode
$R_3$	Fuel Cell External Load (Single Cell)
$\rho_{electrode}$	Density of Electrodes
$R_{ct}$	Total Charge Transfer
$R_{Load}$	Load Resistor
$\sigma_2$	Total Electronic Conductivity
$\sigma_a$	Ionic Conductivity of Anode
$\sigma_c$	Ionic Conductivity of Cathode
$\sigma_e$	Ionic Conductivity of Electrolyte
$T$	Time
$T$	Temperature
$\theta$	Phase of Harmonic Component

$V_1$	Fuel Cell Voltage
$V_2$	DC-DC Boost Converter Output Voltage
$V_3$	Inverter Output RMS Voltage Before LC Filter
$V_4$	Inverter Output RMS Voltage After LC Filter
$[V_0]_{Bulk}$	Molar Fraction of Oxygen Vacancies
$\omega$	Inverter Operating Frequency
$\omega_r$	Ripple Frequency

# Chapter 1

## Introduction

In recent years, the demand for clean and sustainable energy has increased. Although renewable energy is an effective source of electricity, it still requires backup as the availability of natural energy sources varies frequently. Fuel cells are clean and sustainable energy sources that can not only be implemented as backup power sources for large renewable power supplies, but are also capable of being a major power source in micro grid systems. Fuel cells convert electrochemical energy into electrical and thermal energy. During this process, steam is the only residual component which, makes it an ideal choice when considering alternate and clean energy sources.

Due to the varied application of fuel cells, which ranges from hybrid vehicles to grid backup, it is important to analyze their performance under various load conditions. A fuel cell, unlike other linear power sources, exhibits nonlinear behavior under nonlinear load conditions. Due to the nonlinear nature of the power produced, it is essential to understand the impact of AC and DC loads separately and also to devise a method to linearize the power supply. Researchers

have established the phenomenon of ripple propagation when the fuel cell is operated under nonlinear loads. The propagating ripple current causes physical damage to the fuel cell which, not only lowers cell lifespan but, also causes power degradation. In order to improve the performance of the fuel cell and also to ensure a long cell lifespan, it is important to eliminate or reduce ripple propagation. This is the main objective of this thesis and is outlined in section 1.1

## **1.1 Thesis Objectives**

For the purpose of analysis, a fuel cell model is first developed. The fuel cell model is based on the material specifications of a Solid Oxide Fuel Cell (SOFC). As stated earlier, the main objective of this thesis is to analyze the effects of ripple propagation on a fuel cell and attempt to reduce or eliminate these ripples. To aid in the study of ripple propagation, a power system, using the modeled fuel cell as the power source, is constructed. Frequency spectrum analysis is used to estimate the extent to which the ripples affect the fuel cell voltage and current. It is assumed that the individual power stages of the system cannot be improved further and hence the propagating ripples need to be eliminated from the output of the fuel cell through other means. In this thesis, an Active Power Filter (APF) is used to remove the ripples from the fuel cell current. The goal is to allow the freedom to use any configuration for the DC-DC and DC-AC power stages of the system, while ensuring that the fuel cell is not affected by any harmonics present in the system. Though all the analysis will be carried out through simulations (MATLAB/Simulink), the fuel cell performance for both DC and AC load is verified against experimental results that have already been published in various journals.

## 1.2 Thesis Organization

The thesis objectives are outlined in Chapter 1 while providing short introduction for the other chapters.

The basic principles of a fuel cell are briefly introduced in Chapter 2, along with its classification. Chapter 2 also contains a discussion on research carried out in the field of fuel cell behaviour. A fuel cell model is developed in Chapter 3 and the effects of DC and AC load are briefly discussed. In Chapter 4, the process of ripple propagation and the effects of ripples on the modeled fuel cell under steady state conditions are analyzed. The effects of magnitude and frequency variations are also discussed in this chapter. A detailed discussion of APFs is carried out in Chapter 5. The type of control scheme that can be implemented for an APF used in a fuel cell powered system is discussed in this chapter. The chapter also includes the implementation and evaluation through simulation of an APF-based fuel cell system. Chapter 6 is the final chapter of this thesis in which the conclusions as well as recommendations for further work on this subject are presented.

# Chapter 2

## Introduction to Fuel Cells and Literature Review

With increased demands for clean and reliable energy, fuel cells have found a unique niche for scientific exploration and commercial production. The use of fuel cells in the automotive industry has already been well established with the launch of the Toyota Mirai and has prompted other automobile companies to take note of the immense efficiency of these power devices [1]. The Ramea hybrid energy project in Newfoundland, which uses hydrogen fuel cells as backup power sources, is an attempt to provide clean energy for a small community [2].

In general a fuel cell can operate up to 10 years with minimum maintenance. This makes the fuel cell a stable and reliable power source. Fuel cells operating at high temperatures have higher fuel flexibility and can operate on both carbon-based fuels as well as pure hydrogen, which increases commercialization and usability [3]. In this Chapter, various classifications and usage of fuel cell will be discussed. This Chapter will also discuss the potential problems facing the use of

fuel cells in commercial applications and the resolutions to these problems as adopted by other researchers.

## **2.1 Types of Fuel Cells**

The type of electrolyte determines the temperature at which the fuel cell can be operated. Based on the type of electrolyte, fuel cells are primarily classified into six categories. Table 2.1 provides a summary of the basic differences between fuel cells [4].

Table 2.1: Classification of Fuel Cells

<i>Type of Fuel Cell</i>	<i>Type of Cathode</i>	<i>Type of Anode</i>	<i>Type of Electrolyte</i>	<i>Temperature of Operation</i>	<i>Type of Catalyst</i>
<i>Proton Exchange Membrane</i>	<i>Pt on C</i>	<i>Pt on C</i>	<i>Perfluorosulfonic acid</i>	<i>90°C</i>	<i>Platinum</i>
<i>Direct Methanol</i>	<i>Pt - Ru</i>	<i>Pt - Ru</i>	<i>Polymer</i>	<i>50 – 120°C</i>	<i>Platinum</i>
<i>Alkaline</i>	<i>Pt - Au</i>	<i>Pt - Pd</i>	<i>KOH</i>	<i>100°C</i>	<i>Platinum</i>
<i>Phosphoric Acid</i>	<i>Pt on C</i>	<i>Pt on C</i>	<i>H<sub>3</sub>PO<sub>4</sub></i>	<i>200°C</i>	<i>Platinum</i>
<i>Molten Carbonate</i>	<i>Li doped NiO</i>	<i>Ni</i>	<i>Li<sub>2</sub>CO<sub>3</sub>, K<sub>2</sub>CO<sub>3</sub></i>	<i>650°C</i>	<i>Alloy of nonprecious metals</i>
<i>Solid Oxide</i>	<i>Sr doped LaMnO<sub>4</sub></i>	<i>Ni or Y<sub>2</sub>O<sub>3</sub></i>	<i>Y<sub>2</sub>O<sub>3</sub> stabilized ZrO<sub>2</sub></i>	<i>800 - 1000°C</i>	<i>Not Required</i>

Other than the specified categories, a new class of fuel cells has been recently introduced, the regenerative fuel cells [5]. Regenerative fuel cells have two stages of operation. The first stage acts like a normal fuel cell where electrical energy is produced from the chemical reactions due to the injected fuel. The second stage uses electrolysis to recombine the residual components to form the fuel that can be re-injected into the first stage of the regenerative fuel cell. Electrolysis is a highly energy consuming process and is also costly to develop. Ideally, the energy of the electrolytic stage is supplied by a separate energy source so as to not decrease the overall efficiency

of the first stage. This makes it ideal for use along with renewable energy sources such as solar, wind or hydro energy. Regenerative fuel cells can also act as energy storage devices in which the excess energy from renewable sources can be stored in the form of hydrogen or any readily available fuel [6].

The temperature of operation also determines the extent of usage for a given fuel cell. The Proton Exchange Membrane Fuel Cell (PEMFC) is the most commercially popular fuel cell. Its optimum temperature of operation and its compact stack structure increases its commercial usage. PEMFCs have been developed for both stationary and portable applications [7]. The Phosphoric Acid Fuel Cell (PAFC) was the first fuel cell to be commercialized and is ideal for stationary applications as it is highly stable and economically feasible [8]. The Direct Methanol Fuel Cell (DMFC) is a subcategory of the PEMFC, and though it does not produce a large amount of power, a small amount of power is produced over a long period of time [7]. Alkaline Fuel Cell (AFC) is the most developed fuel cell as it has 70% efficiency of operation. Due to this, it has been used by NASA for the Apollo space mission [9]. The Molten Carbonate Fuel Cell (MCFC) and the Solid Oxide Fuel Cell (SOFC) fuel cells operate at very high temperatures and are also capable of producing very high levels of power [10]. The higher temperature of operation reduces the cost of catalysts. Due to the high temperature, both MCFC and SOFC, though widely used in high power stationary applications, do not find much use for portable applications. However, recently SOFCs have been developed for portable chargers [11].

## 2.2 Types of Fuel Cell Models

In order to test the performance of a fuel cell as the main or the alternate source of power, it is neither economic nor safe to use an actual fuel cell. In the case of high temperature fuel cells, the use of an actual fuel cell, in order to investigate its performance, requires additional infrastructure and precautionary measurements. It is economic to develop fuel cell models or simulators for these investigations.

Any fuel cell model is primarily based on its electrochemical reactions. Though all fuel cells convert hydrogen or hydrocarbon molecules to produce energy and water molecules, the amount of energy produced depends on the physical attributes of the specified fuel cell. The type of electrolyte, electrode, temperature of operation and pressure within the container are the primary parameters that influence the amount of voltage produced by a fuel cell. The basic equations for an electrochemical reaction follow the principles of thermodynamics, fluid dynamics and mass transfer. Mechanistic models are developed using real time computation of all the electrochemical equations attributed to the specified fuel cell [12], [13]. The mechanistic model can also be developed to include water, air and fuel management system. Although the mechanistic models have immense potential, only a few models have been developed that depict the dynamic characteristic of the fuel cell as this involves further computation which might slow down the simulation process.

For empirical models, the complex electrochemical equations are either represented as a simple mathematical equation or as an equivalent circuit. These empirical models are simpler to implement and are also more useful in studying the dynamic electrical properties of a fuel cell. Due to its simplicity the empirical fuel cell model is extensively used [14], [15]. Since empirical models are simplified mathematical representations, they can be used to study both DC and AC

state of operation. During the DC steady state of operation all the physical parameters are kept constant so that various parametric dependencies, such as diffusion rate and pressure versus temperature performance, can be investigated. In order to study the AC characteristics of the fuel cell, dynamic models are preferred [16]. The simplest approach to develop a dynamic model is to create an equivalent AC circuit for the fuel cell [17], [18].

Cheddie et al. [19] have reviewed the various fuel cell models and described the pros and cons of each method. Detailed discussion on the fuel cell model used in this thesis is given in Chapter 3.

## **2.3 Literature Review**

Due to the increasing demand for alternate energy sources the frequency of fuel cell research has increased considerably in the last few decades. In February 2015, FCO Power Inc. announced plans to mass produce their new SOFC unit, called the Printed Fuel Cell, which is only 3cm in thickness and can generate 700 W [20]. FCO Power aims to commercialize this new product in the 2020 Tokyo Olympics. Several SOFC prototypes have already been implemented in various European Countries, as part of the Ene-field program which implements fuel cells as part of Combined Heat and Power Systems (CHP) [21]. The Ene-field program is an echo of its Japanese counterpart, the Ene-farm program. SOFCs are ideal for CHP applications as they operate at high temperatures and the excess heat and water can be easily directed for residential use.

The most relevant research revolves around the improvement of solid oxide materials so as to operate SOFCs at lower temperatures. Liu et al. [22], Leng et al. [23] and other researchers

have developed better solid oxides that enable the fuel cell to operate between 500°C to 700°C, which is lower than the normal assigned temperature for SOFCs of 800°C to 1000°C [24].

While fuel cells have proven to be stable and reliable power sources, they perform poorly against nonlinear loads as opposed to DC loads. Schneck et al. [25] conducted a research on the impact of DC and AC loads on the physical and electrical parameters of a PEMFC. They concluded that though the fuel cell might exhibit slight decrease/increase of output voltage with respect to increasing/decreasing DC load current, the fuel cell output voltage and current retain their DC characteristics. DC loads also cause minimum variations in the fuel cell operating parameters. Hence, using a DC load allows the fuel cell to operate at the most optimum conditions. This however is not true for AC loads, where the propagation of ripples destabilizes the operating conditions of the fuel cell and also causes the fuel cell to behave as a nonlinear power source.

An extensive study of system interactions along with ripple propagation carried out by Acharya et al. [26] concluded that the propagation of ripples also caused the system parameters, i.e. temperature, pressure, etc. to vary. A fuel cell's stability is determined by the extent to which the system parameters are maintained at a constant value. Hence, such variations can not only decrease the fuel cell's lifespan, but can also raise safety concerns for high temperature fuel cells, such as SOFC. Ripple propagation for stationary power systems can be smoothed using large capacitors; but, for automotive systems, ripple propagation is a major concern as constant power levels are essential for efficient operation. Chiu et al. [27] discuss the effects of ripple propagation for automotive applications for fuel cells.

Kim et al. [28], [29] have studied the effects of constant load change for a PEMFC. The studies have revealed that fuel cell electrical efficiency is inversely related to the magnitude of load ripples. Similar studies have also been conducted by Ferrero et al. [30] and other researchers

[31], [32]. The presence of ripples causes physical damage to the fuel cell and also lowers its lifespan. The studies conducted by Gemmen [33] and several other researchers have detailed the exact process of cell degradation [34] - [36].

In order to reduce the presence of current ripples in the fuel cell output current, many different approaches have been suggested. There are two possible solutions to reduce ripple propagation. The amount of propagating ripples can be reduced by improving the individual power stages. With lesser load harmonics, the magnitude of propagating ripples will also be greatly reduced. Zhu et al. [37] have suggested inverter control to lower the input current harmonics and hence reduce the ripple propagation. Similar research has been conducted by Kim et al. [38] to reduce the propagation of ripples. Auld et al. [39] have also proposed the use of active power filter at the load to minimize load ripples and hence minimize the propagation of ripples.

The second method by which ripples can be reduced is by means of filters that are combined as part of the converter stage. This implies that the converter, either boost or buck, is modified to include an active power filter which switches the converter to not only remove the propagating harmonics from the fuel cell input, but also accomplishes boost or buck functionalities. One such example is the active power filter proposed by Mazumdar et al. [40]. A two-level active power filter, which removes both low and high frequency harmonics is included as the input stage of a boost converter. Itoh et al. [41] have suggested a DC center-tap converter topology to act as an active filter. Kwon et al. [42] have proposed an improved boost converter stage that removes the load ripples for a large grid connected fuel cell. Similar work has been conducted by several other researchers [43], [44]. Although the use of modified converter has resulted in novel circuit designs, the added filter makes the entire power system bulky, which is

not suitable for smaller power systems, where other than power stability, compact circuits are also equally important.

For low temperature fuel cells, the effect of ripple propagation can be easily studied by using a single fuel cell. But for high temperature fuel cells, such as SOFC, experimental analysis is difficult, as even a single SOFC unit would require the same safety guidelines as would an entire stack of high temperature fuel cells. Hence the best solution, is to simulate and study the behaviour using fuel cell models.

## **2.4 Summary**

The classification of various fuel cells has been presented. A short discussion on the importance of fuel cell modeling and the distinction between the previously established models has also been discussed. It has been established that fuel cells behave like nonlinear sources in the presence of nonlinear or AC loads. The presence of nonlinear loads can disrupt regular fuel cell operation and can also shorten the cell lifespan. Hence, it becomes important to analyse the cause of such nonlinearity and provide solutions that will allow the fuel cell to provide stable power levels for a longer period of time. Various methodologies, as proposed by other researchers, to remove or minimize nonlinearity of fuel cells have been introduced in this chapter.

# Chapter 3

## Fuel Cell Modeling

Fuel cells are electrochemical devices. The electrochemical process involves the oxidation of fuel to release energy and water if the fuel used is hydrogen, or humidified carbon dioxide if a carbon based fuel is used. In the previous Chapter, fuel cell classification and applications were briefly discussed along with various drawbacks and their proposed solutions. The focus of this Chapter is to identify the physical parameters of a Solid Oxide Fuel cell (SOFC) and describe a numerical modeling approach that can be later on used for further analysis.

SOFC can use both carbon based fuels and hydrogen; however, maximum energy is produced by the oxidation of hydrogen [45]-[47]. In addition, oxidation of hydrogen is easier to model numerically. Hence, hydrogen is selected as the fuel for modeling the SOFC. The most important parameters concerning a fuel cell's operation are fuel pressure, temperature, fuel volume, and air volume. The conductivity of the electrode and electrolyte are also important although, the conductivity is also partially dependent on temperature. A generalized structure of a SOFC is shown in Figure 3.1.

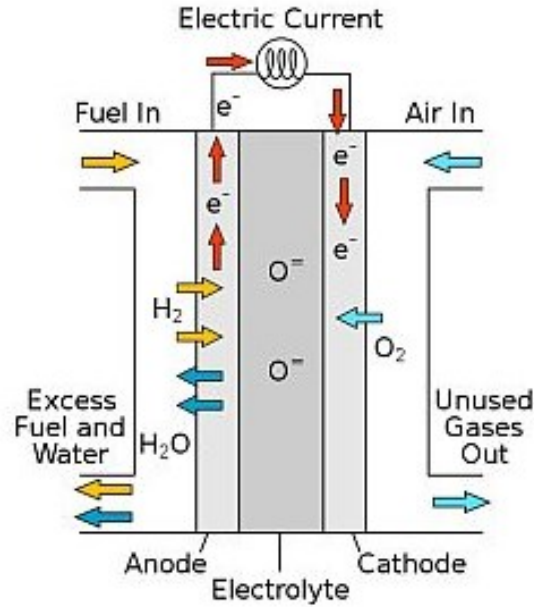


Figure 3.1: Generalized Solid Oxide Fuel Cell Structure

The number of electrons that are transferred across the electrodes is dependent on the stoichiometric process within the cell. The stoichiometric process is described by two separate equations, on either electrode. For the SOFC, as given in Figure 3.1, using hydrogen as fuel, the equations at the anode and cathode are described below:

Equation at the anode:



Equation at the cathode:



The fuel cell voltage is typically described by the Nernst equation as given in (3.3)

$$E_{max} = \frac{R.T}{2.F} \ln K - \frac{R.T}{2.F} \ln \frac{p_{H_2} \cdot p_{O_2}^{1/2}}{p_{H_2O} \cdot p_{ref}^{1/2}} \quad (3.3)$$

where,  $R$  is Gas constant ( $8.315 * 10^{-5} \text{ m}^3\text{BarK}^{-1}\text{mol}^{-1}$ ),  $T$  is temperature in Kelvin,  $F$  is Faraday's constant ( $96485 \text{ Cmol}^{-1}$ ),  $p_{H_2}$  is partial pressure of fuel in Bar,  $p_{O_2}^{1/2}$  is the partial pressure of oxygen in Bar;  $p_{H_2O}$  is the partial pressure of residual water in Bar; and  $p_{ref}^{1/2}$  is the referral partial pressure, assumed to be 1 Bar.  $K$  is the chemical equilibrium constant and can be calculated using equation (3.4)

$$K = A. e^{\frac{-E_0}{R.T}} \quad (3.4)$$

The constants  $A$  and  $E_0$  are obtained from thermodynamic tables depending on the type of reactants involved in the process. The Nernst voltage is the maximum voltage or ideal voltage that can be obtained from the fuel cell in the absence of any losses.

### 3.1 Classical Approach to Fuel Cell Modeling

Traditionally, fuel cell modeling is based on the approximation of the current-voltage curve, also called the polarization curve, obtained from experimental studies. The polarization curve is divided into three regions: activation loss (region a), ohmic loss (region b) and concentration loss (region c) as shown in Figure 3.2.

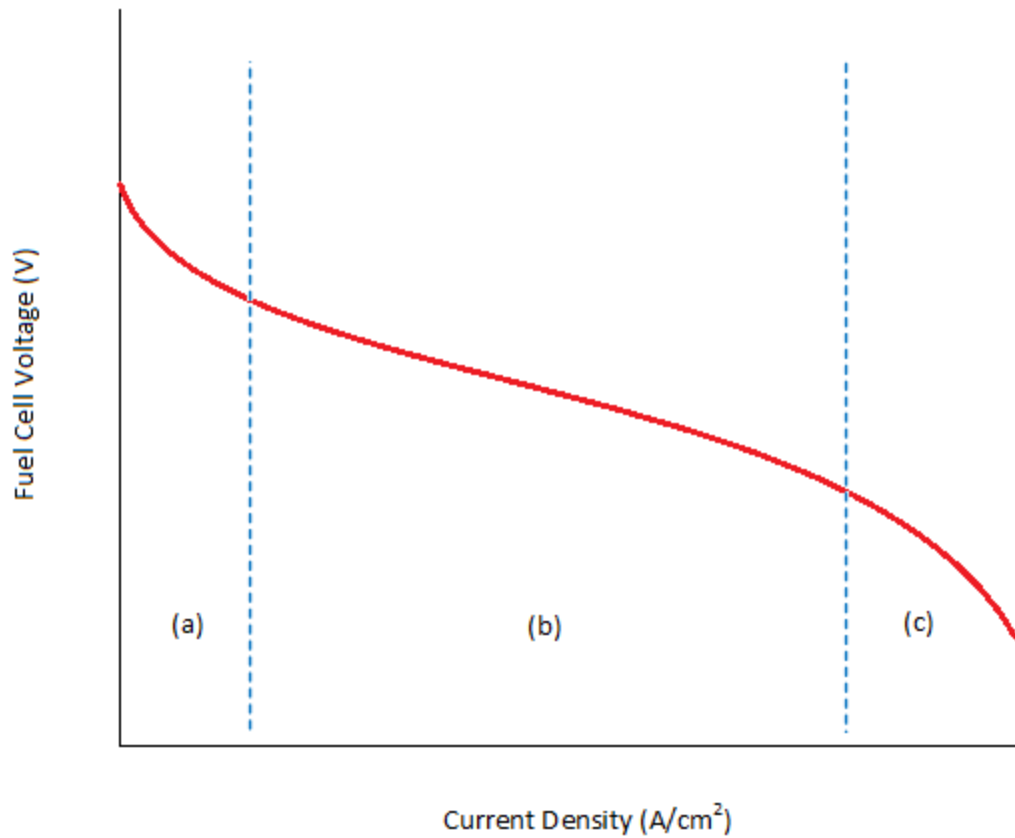


Figure 3.2: Fuel Cell Polarization Curve (a) Activation Loss (b) Ohmic Loss (c) Concentration Loss

These losses, when subtracted from the Nernst voltage, provide the actual fuel cell voltage. Hence, the cell voltage is made up of four elements as given in equation (3.5)

$$E = E_{max} - \eta_{act} - \eta_{ohm} - \eta_{con} \quad (3.5)$$

where,  $E_{max}$  is the Nernst Voltage as given in equation (3.3),  $\eta_{act}$  is activation loss voltage,  $\eta_{ohm}$  is ohmic loss voltage, and  $\eta_{con}$  refers to concentration loss voltage.

The activation loss refers to the energy consumed by the fuel cell to necessitate the transfer of electrons from the electrode to the electrolyte. It is calculated by the Butler-Volmer equation [48] and is linearized to the form of Tafel equation as given in (3.6)

$$\eta_{activation} = \left(\frac{RT}{\alpha nF}\right) \ln(i_o) - \left(\frac{RT}{\alpha nF}\right) \ln(i) \quad (3.6)$$

where,  $\alpha$  is the coefficient of charge transfer,  $n$  is the number of moles of electrons transferred,  $i_o$  is the exchange current and  $i$  is the actual fuel cell current.

The ohmic loss occurs due to the resistance offered by the electrolyte and electrode to the flow of ions and electrons, respectively. It is largely dependent on the temperature at which the fuel cell is operated and the material used for constructing the electrical components of the cell [49]. The ohmic loss is represented by the simplified equation

$$\eta_{ohmic} = \text{cell internal resistance} * \text{fuel cell current} \quad (3.7)$$

As noted before, the cell internal resistance is a function of temperature.

Lastly, the resistance offered by the electrolyte to the movement of reactants through the electrolyte is termed as the concentration loss [50]. This loss is also a material dependent parameter and can be expressed as

$$\eta_{Concentration} = \left(\frac{RT}{nF}\right) \ln \frac{C_b}{C_\infty} \quad (3.8)$$

where,  $C_b$  is the triple-phase boundary and  $C_\infty$  is the bulk concentration of the reactants.

## 3.2 Fuel Cell Modeling Based on Equivalent Circuit

The classical approach to fuel cell modeling involves complex calculations and is accurate for a particular parametric condition. The results cannot be extrapolated for other conditions. Santarelli et al. [51] suggested a method that takes into account the interactions between each changing parameter. The method produces a more definitive fuel cell model that can accurately predict the cell voltage at any parametric change. The SOFC generates electricity by releasing oxygen ions that move through the solid electrolyte. Hence, the fuel cell operation can be explained through an electric circuit as shown in Figure 3.3.

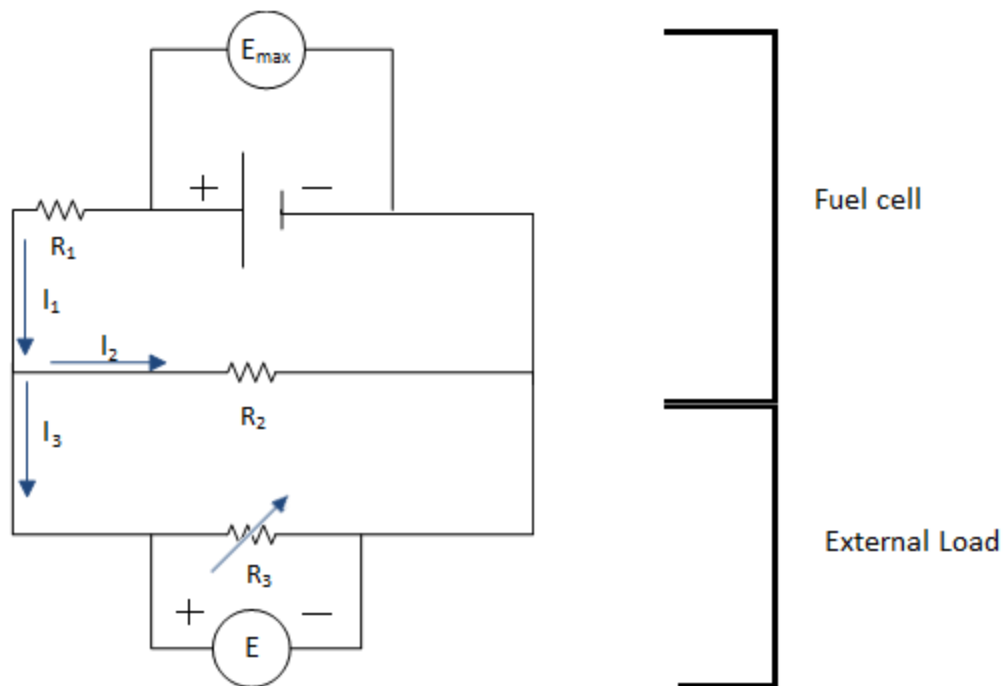


Figure 3.3: SOFC Equivalent Electrical Circuit

Figure 3.3 shows two different resistive values which represent two different values of internal resistance, ionic ( $R_1$ ) and electronic ( $R_2$ ) resistance.  $R_3$  represents the external load. The voltages  $E_{max}$  and  $E$  represent the Nernst voltage and the load voltage due to the external load  $R_3$ . Using Ohm's and Kirchhoff's laws, equations (3.9) – (3.11) are obtained.

$$I_1 = \frac{E_{max} - E}{R_1} \quad (3.9)$$

$$I_2 = \frac{E}{R_2} \quad (3.10)$$

$$I_1 = I_2 + I_3 \quad (3.11)$$

Electrical dependence can be correlated to gas flow using the fuel utilization factor denoted by  $\eta_f$ . The fuel utilization factor is related to the current drawn from the cell using equation (3.12)

$$I_3 = (i_{max} - I_2) \cdot \eta_f \quad (3.12)$$

where,  $i_{max}$  represents the maximum current density developed on the electrodes. Using equations (3.11) and (3.12) the equation for the cell voltage is obtained as

$$E = E_{SOFC} = \frac{E_{max} - i_{max} \cdot R_1 \cdot \eta_f}{\frac{R_1}{R_2}(1 - \eta_f) + 1} \quad (3.13)$$

The maximum current drawn is a function of the fuel flow rate and is given by (3.14)

$$i_{max} = \frac{2 \cdot F \cdot n_{H_2, equivalent}}{A_{cell}} \quad (3.14)$$

where,  $n_{H_2, equivalent}$  is the equivalent fuel molar flow rate and  $A_{cell}$  is the total cell surface area.

From equation (3.13) it is clear that the SOFC voltage is dependent on five main parameters, which are described in the following sections.

### 3.2.1 Maximum Voltage ( $E_{max}$ )

This is the Nernst voltage and is calculated solely based on the physical parameters of temperature and pressures of both fuel and air in the container as given by equation (3.3).

### 3.2.2 Maximum Current Density ( $i_{max}$ )

Maximum current density, as given by equation (3.14), correlates the current from the fuel cell to the fuel flow rate.

### 3.2.3 Fuel Utilization Factor ( $\eta_f$ )

Fuel utilization factor is calculated based on the inlet and outlet fuel flow rates and is represented by equation (3.15)

$$\eta_f = 1 - \frac{n_{H_2, \text{equivalent}, \text{out}}}{n_{H_2, \text{equivalent}, \text{in}}} \quad (3.15)$$

where,  $n_{H_2, \text{equivalent}, \text{out}}$  is the outlet fuel flow rate and  $n_{H_2, \text{equivalent}, \text{in}}$  is the inlet fuel flow rate.

### 3.2.4 Area Specific Ionic Resistance

The area specific ionic resistance is the sum of the individual ionic resistances of the electrodes and the electrolyte and is expressed as:

$$R_1 = \frac{\delta_e}{\sigma_e} + \frac{\delta_a}{\sigma_a} + \frac{\delta_c}{\sigma_c} \quad (3.16)$$

where,  $\delta_e$ ,  $\delta_a$  and  $\delta_c$  represent the thickness of electrolyte, anode and cathode respectively. The ionic conductivity of electrolyte, anode and cathode are represented by  $\sigma_e$ ,  $\sigma_a$  and  $\sigma_c$  respectively. For a solid-oxide electrolyte, the ionic conductivity is temperature dependent and is expressed as:

$$\sigma_e = \sigma_0 \cdot e^{\frac{-E_{act}}{R.T}} \quad (3.17)$$

where,  $\sigma_0$  and  $E_{act}$  are material dependent factors. Extensive data for the same is available from various research publications [52].

### 3.2.5 Area Specific Electronic Resistance

Solid oxides are not only ionic conductors but also electronic conductors which gives rise to electronic resistance. Electronic resistance does not have a significant impact on cell voltage or fuel utilization rate and it can be calculated as:

$$R_2 = \frac{\delta_e}{\sigma_2} \quad (3.18)$$

where,  $\delta_e$  is electrolyte thickness and  $\sigma_2$  is electronic conductivity. Electronic conductivity can be further expressed as a function of the open circuit voltage ( $E_{OCV}$ ) and the Nernst voltage as given in (3.19)

$$\sigma_2 = \delta_e \cdot \frac{E_{max} - E_{OCV}}{R_1 \cdot E_{OCV}} \quad (3.19)$$

where, substituting  $\eta_f = 0$  in equation (3.13),  $E_{OCV}$  can be defined as

$$E_{OCV} = \frac{E_{max}}{\frac{R_1}{R_2} + 1} \quad (3.20)$$

As is the case of ionic conductivity, electronic conductivity is also a material dependent property and can be obtained accurately from published results for solid oxides [52]. The conductivity properties of solid oxide materials is a field of intense research and has been used extensively in this thesis to calculate various parameters required to develop the SOFC model [53]-[56].

In order to complete the fuel cell model, it was necessary to gather relative data regarding the cell's material properties. Using the material properties of an experimental SOFC, as used by Virkar et al. [57], the SOFC model was duly developed. The parameters are presented in detail in Appendix A.

### **3.3 DC Properties of Fuel Cell**

The DC properties of a fuel cell are described by its polarization (voltage versus current density) and power density curves. Current density refers to the spread of electrons over the electrode surface. As opposed to the classical approach of fuel cell modeling, the method proposed by Santerelli et al. [51] has the advantage of concentrating solely on the material losses for solid oxides and hence increasing the accuracy of the model and eliminating the need to calculate losses separately. The adopted SOFC model also accounts for temperature, pressure and fuel/air flow variations with regards to material losses and hence, the same SOFC model can effectively estimate the DC behaviour of SOFCs of varying electrode/electrolytic mediums. In order to validate the SOFC model, the results from the developed model are compared against experimental results, as published by Virkar et al. [57]. The fuel cell is simulated at 800°C under constant fuel pressure, fuel and air flow rates. Figures 3.4 (a) and 3.4 (b) compares the obtained results against the results in [57]. The simulated result, as obtained from the fuel cell model is depicted by the blue line, while the experimental result, as published by Virkar et al. [57] is shown by the red dots.

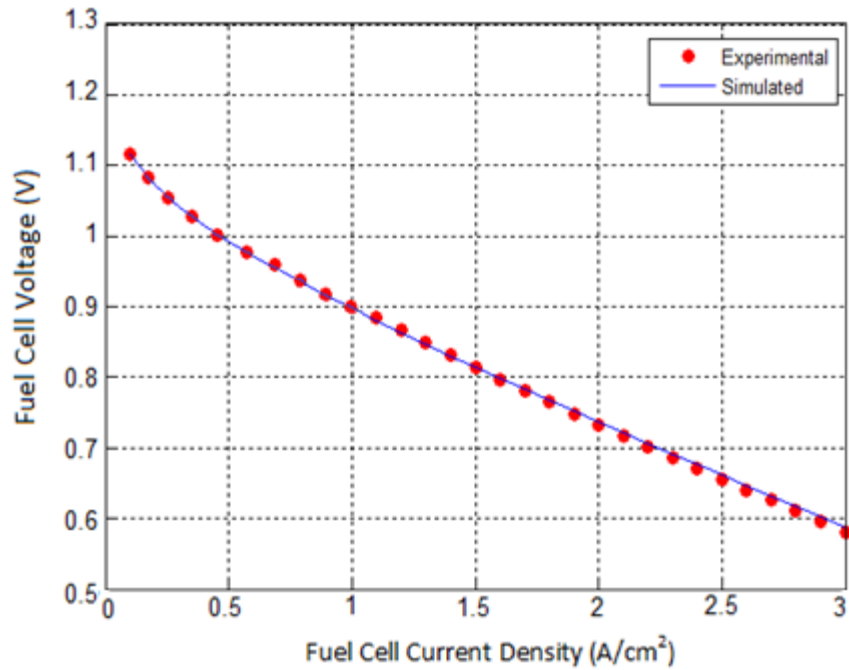


Figure 3.4 (a): Polarization Curve of SOFC at 800°C

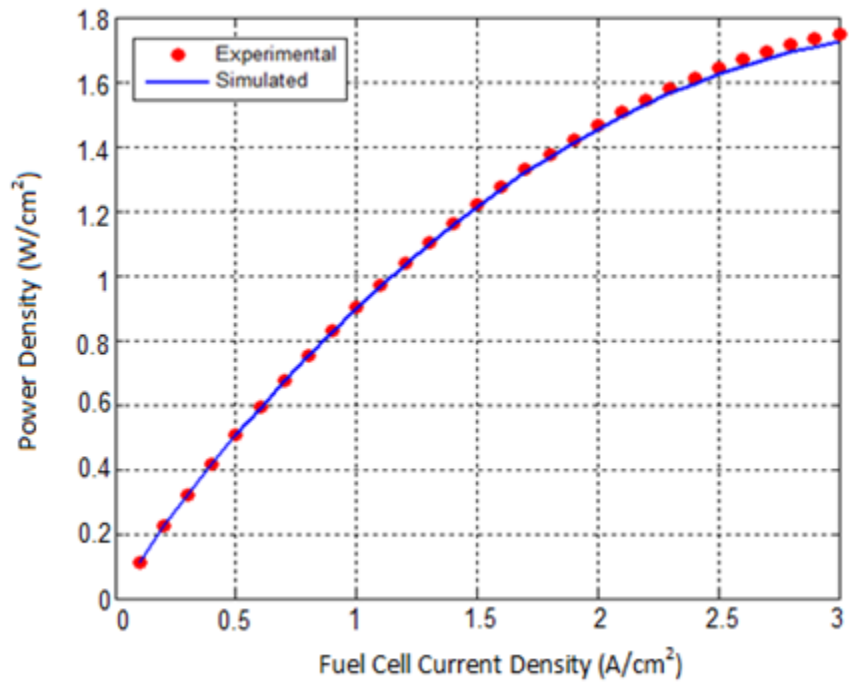


Figure 3.4 (b): Power Density Curve of SOFC at 800°C

The polarization curve (Figure 3.4 (a)) shows that the simulated results closely follow the experimental results. This is true for the power density curve (Figure 3.4 (b)) as well. Hence, the developed SOFC model is proven valid. The validity of the fuel cell model is further tested at three different temperatures. At different temperatures, the area specific ionic and electronic resistances being temperature-dependent vary and hence, result in the polarization and power density curves shown in Figures 3.5 (a) and 3.5 (b).

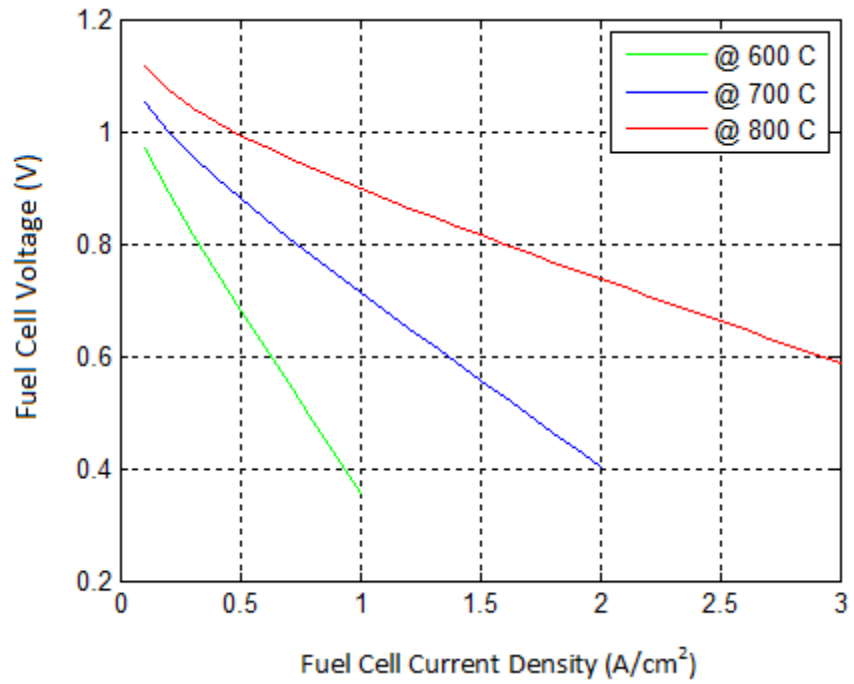


Figure 3.5 (a): Polarization Curve of SOFC at Three Different Temperatures

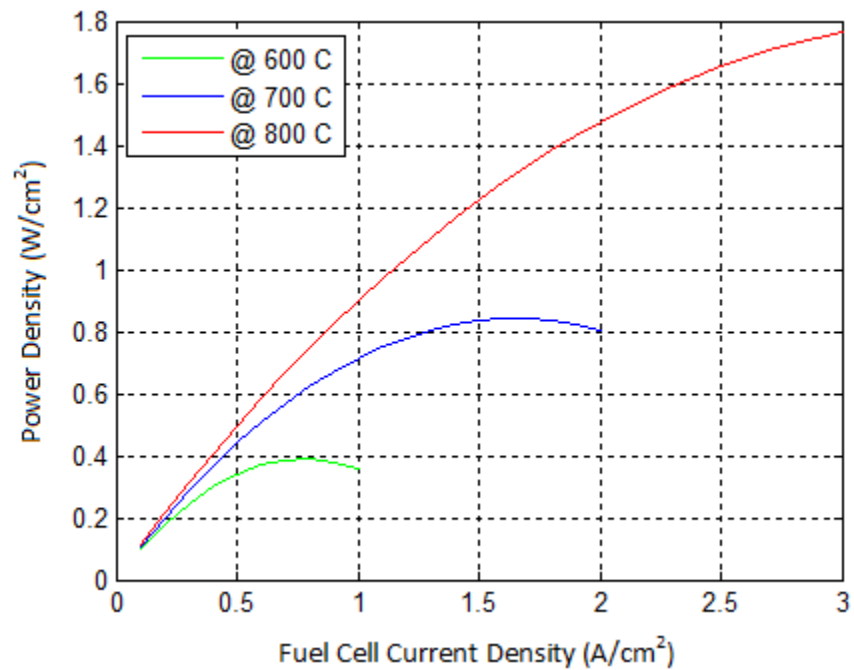


Figure 3.5 (b): Power Density Curve of SOFC at Three Different Temperatures

From the polarization curve, shown in Figure 3.5 (a), it can be concluded that the fuel cell produces maximum voltage at high temperature and low current density. It can also be concluded that the fuel cell is capable of producing voltage for larger values of current density only at high temperatures. The power density curve (Figure 3.5 (b)), shows that at higher temperatures the fuel cell produces maximum power at high current density. Hence, the modeled SOFC is capable of reacting to temperature changes and reproducing the fuel cell's actual behavior effectively.

## **3.4 AC Properties of the Fuel Cell**

In order to examine the AC properties of the fuel cell a complete fuel cell model that describes the behavior of ripples on the fuel cell output current needs to be developed. Though a fuel cell is a DC device, it exhibits nonlinear behavior due to the presence of current ripples. The nonlinear behavior is a result of the interaction between the current ripples and a phenomenon that gives rise to charge double layer or a double-layer capacitance. The double-layer capacitance is described below.

### **3.4.1 Double-layer Capacitance**

In electrochemical systems, the charge double-layer is formed due to two phenomena [49]. The first is the diffusion of gaseous fuel across the electrolytic medium, which is similar to the diffusion effect in semiconductors. The second and the most predominant phenomenon is the presence of charge difference around the electrodes, due to the reaction of electrons with the electrodes and the ions in the electrolyte, in the presence of an applied voltage. The probability of the reaction depends on the density of the charges, which is determined by the fuel utilization ratio,

which in turn is directly proportional to the produced current. With high density of charges higher current can be produced. However, the accumulation of charges causes an abrupt change in the fuel cell output voltage, which is termed as “activation overvoltage” [58]. The activation overvoltage is a load sensitive parameter and explains the difference in behavior once the fuel cell is connected to a nonlinear load.

The double-layer phenomenon is further explained by segregating the cause of the double-layer into two electrochemical processes. The first electrochemical process is termed as the Helmholtz double-layer and is represented by a capacitance caused when the electrodes release ions which are repelled by the co-ions, while being attracted by the oppositely charged ions on the other electrode. This forms a charge double-layer while being separated by a solid electrolyte [59]. The capacitor value can be evaluated using equation (3.21):

$$C_H = \varepsilon \frac{A_e}{d_e} \quad (3.21)$$

where,  $\varepsilon$  is the electrical permittivity of electrode (between 1 to 60 F/cm),  $A_e$  is the electrode surface area ( $\text{cm}^2$ ) and  $d_e$  is the distance between the electrodes (cm).

The second electrochemical process is called the diffuse double-layer in which, the change in concentration of the counter ions near a charged surface follows the Boltzmann distribution. The concentration of anions and cations decreases with distance from the surface of the electrolyte-electrode contact. This phenomenon is called the Gouy-Chapman double-layer [35] and is given in equation (3.22):

$$C_{GC} = 4e \sqrt{\frac{\pi \varepsilon \rho_{electrode}}{k_B T} [V_0]_{Bulk} (1 - [V_0]_{Bulk})} \quad (3.22)$$

where,  $e$  is the elementary charge ( $1.60217657 \times 10^{-19}$  coulombs),  $\rho_{electrode}$  is the density of electrode ( $\text{cm}^{-6}$ ),  $[v_0]_{Bulk}$  is molar fraction of oxygen vacancies (0.07835),  $k_B$  is Boltzmann's constant ( $1.3806488 \times 10^{-23}$  J/K).

The two charge layers are in series and the overall capacitance can be calculated as [60]:

$$\frac{1}{C_O} = \frac{1}{C_H} + \frac{1}{C_{GC}} \quad (3.23)$$

The double-layer capacitance is calculated as a constant value using equations (3.21)-(3.23). The double-layer capacitance acts as a super capacitor and stores charge. The circuit diagram in Figure 3.3 depicts the losses in terms of ionic and electronic resistance. For a solid oxide fuel cell, the double-layer capacitance is a phenomenon attributed to the material properties of the electrode and the phenomenon of total charge transfer resistance. The total charge transfer is an electrochemical property of the electrolyte/electrode pair and can be defined by:

$$R_{ct} = \frac{RT}{nFi_{max}} \quad (3.24)$$

where,  $R$  is Gas Constant ( $8.315 \times 10^{-5} \text{ m}^3\text{BarK}^{-1}\text{mol}^{-1}$ ),  $F$  is Faraday's Constant ( $96485 \text{ Cmol}^{-1}$ ) and  $n$  is the number of electrons.

Condensing Figure 3.3 to a single voltage source, inclusive of all losses, the double-layer capacitance can be modeled in series with the voltage source. This has been given in Figure 3.6.

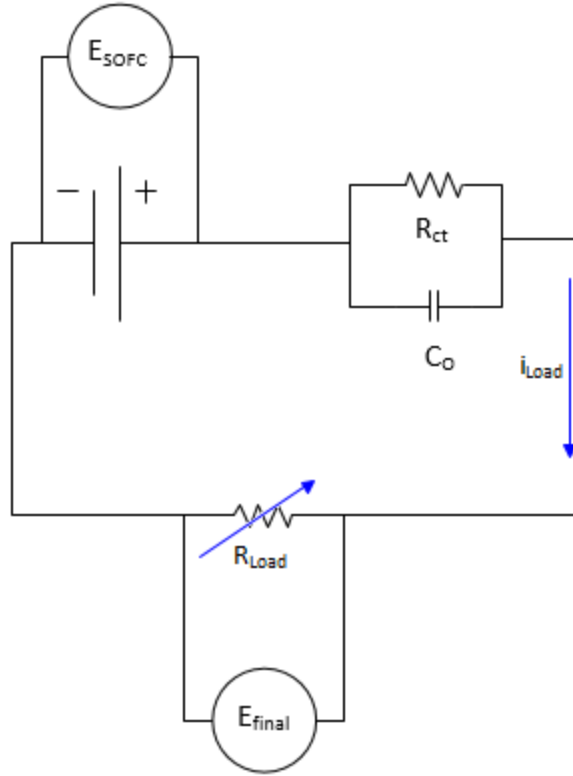


Figure 3.6: Equivalent Fuel Cell Circuit Inclusive of Double-layer Capacitance

If  $i_{ripple}$  is the ripple current,  $E_{SOFC}$  is the SOFC voltage (as given by equation (3.13)), and  $Y_o$  is the total admittance due to the double-layer capacitance and the total charge transfer resistance, the capacitive voltage is given by:

$$E_C = \frac{i_{ripple}}{Y_o} \quad (3.25)$$

where,

$$Y_o = \frac{1}{R_{ct}} + j\omega_r C_o \quad (3.26)$$

and,

$$\omega_r = 2\pi f_{ripple} \quad (3.27)$$

where,  $f_{ripple}$  is the ripple frequency.

Thus, the final fuel cell voltage is given as:

$$E_{Final} = E_{SOFC} - E_C \quad (3.28)$$

### 3.4.2 Behavior of Fuel Cell with Ripple Currents

The presence of this capacitive element is more pronounced when the fuel cell is connected to a power stage that uses switching devices, as the ripples produced by these devices propagate to the fuel cell, as explained by equation (3.25). This causes the cell voltage to fluctuate. The presence of these ripples also causes a phase delay between the fuel cell voltage and current signal.

Figure 3.7 shows the effect of ripple currents at three frequencies on the polarization curve of a unit fuel cell. Three ripple components have been superimposed on the DC fuel cell current of the modeled SOFC. Though the ripple components have different frequencies, they have the same magnitude, which is 25% of the maximum DC value.

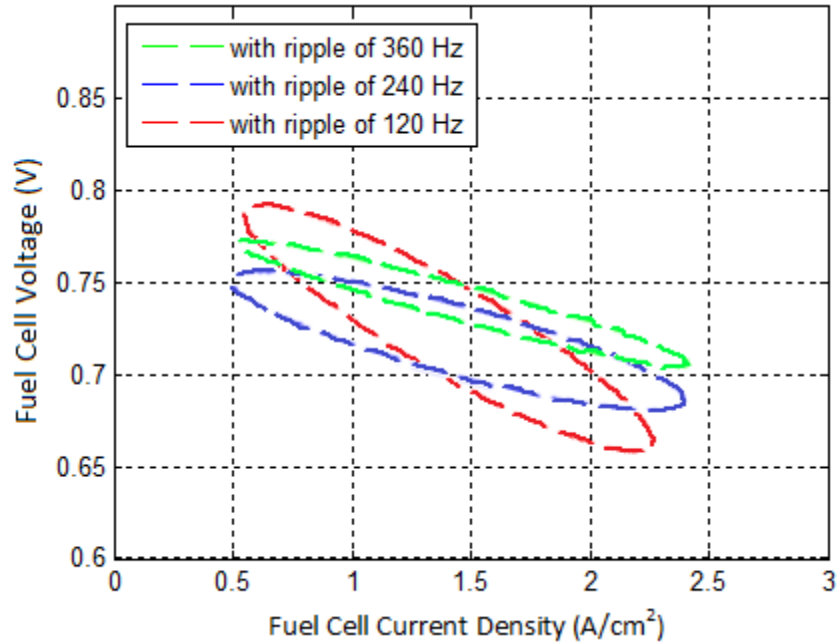


Figure 3.7: Polarization Curve of SOFC under Three Different Ripple Frequencies

In the presence of the ripple components, the voltage magnitude has decreased. The hysteresis trajectory denotes the presence of a phase difference between the current and voltage components. The total admittance, due to the double-layer capacitance and total charge transfer resistance is related to the frequency of the ripple superimposed on the fuel cell current. From equation (3.26) it is clear that the admittance increases at higher frequencies, which in turn decreases the impedance offered by the double-layer capacitance. This results in reduced phase difference between the voltage and current components. This is exhibited by the hysteresis trajectory in Figure 3.7 which shows that the phase angle has greatly reduced for the current signals containing ripple components of 240 and 360 Hz. The decrease in phase difference reduces the trajectory slope and the amplitude of the hysteresis trajectory. The reduced slope angle allows for maximum power extraction, as the hysteresis trajectory then starts to resemble a straight line, which depicts ideal DC operation. It can be concluded that with increasing ripple frequency, the

impedance should greatly reduce and this should increase the magnitude of voltage that can be produced by the fuel cell.

In terms of power, the amount of power that can be extracted from the fuel cell is affected by both magnitude and frequency of the propagating ripple. Figure 3.8 shows the effect of ripple currents on the extracted power from the fuel cell. The extracted power is expressed as a percentage of the maximum DC power, which for the fuel cell considered is 1.8 W/cm<sup>2</sup>.

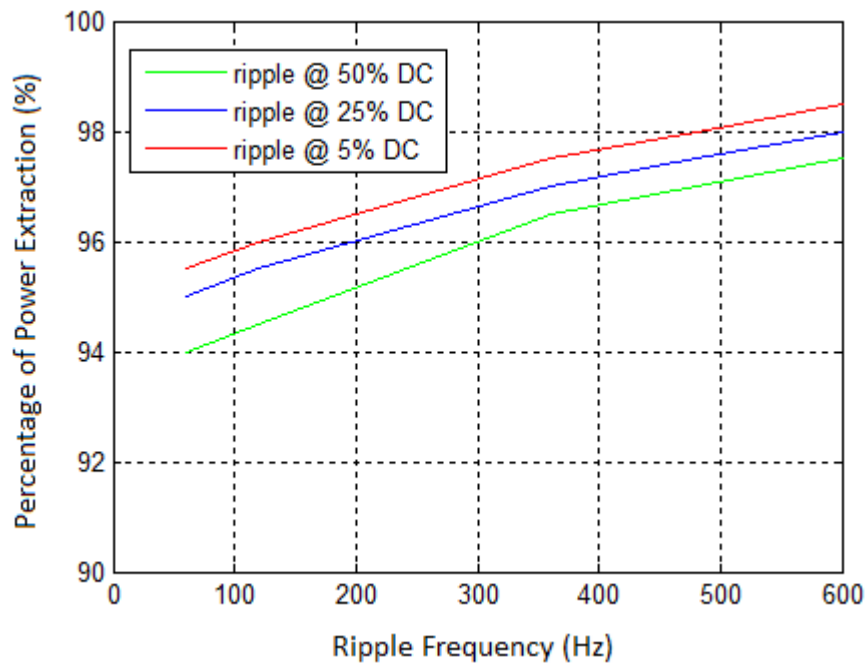


Figure 3.8: Effects of Current Ripple on Power Extraction

The curves in Figure 3.8 indicate that along with the frequency of current ripples, the magnitude of the ripples can also have an impact on the fuel cell. The magnitude of ripple current has a more pronounced effect at lower frequencies as compared to higher frequency ripple current. This in turn confirms the analysis conducted on the Lissajou curve in Figure 3.7.

The prolonged presence of low frequency ripples corrodes the electrolyte and lowers the lifespan of the fuel cell [32], [35], [61]. Low frequency ripples are more harmful for the fuel cell

as compared to high frequency ripples. Biesheuvel et al. [33] conducted a study on the physical degradation of fuel cells due to the presence of ripple current and concluded that lower frequency current ripples wear down the electrolytic medium and reduce the cell lifespan while interfering with the cells ability to operate at constant pressure and temperature. However, minimal or no signs of electrolytic degradation are observed if the frequency of the current ripples is high.

### **3.5 Summary**

The fundamentals of fuel cell modeling are the same for various categories of fuel cells. The cell characteristics are distinct due to the materials used in its construction. Though the classical approach to fuel cell modeling is accurate in predicting the behavior of an actual fuel cell under constant cell parameters, it does not provide an insight into the behavior of the fuel cell if any of the cell parameters are varied. The fuel cell model used in this work overcomes this drawback and effectively predicts the cells behavior under constantly varying cell parameters. In order to achieve this accuracy the fuel cell model is based on the individual material losses. The fuel cell model is further extended to include the effects of the double-layer capacitance that results in nonlinear behavior due to ripple propagation. The double-layer capacitance is described by two separate electrochemical processes which are largely material dependent. Once the capacitance is incorporated into the fuel cell model, it becomes possible to observe the effect of ripple current on the maximum power extraction of the fuel cell. The model confirms that the propagating ripples produce a phase difference between the fuel cell voltage and current components and degrades the cell's power rating. It is observed that the higher the ripple frequency, the less impact the ripples have on the maximum power extraction.

## **Chapter 4**

# **Ripple Analysis of Solid Oxide Fuel Cell**

As discussed in Chapter 3, the phenomenon of double-layer capacitance explains the propagation of current ripples in the fuel cell, while the literature review presented in Chapter 2 confirms that the presence of ripples has detrimental effects on the fuel cell both electrically and from the perspective of the cell's lifespan. In order to appreciate fully the electrical effects, it is important to concentrate on the behavior of the fuel cell waveforms, when it is connected to a nonlinear load through a DC-DC converter and inverter. In this chapter, a fuel cell power system is discussed with detailed analysis of each stage of the power circuit in the presence of a nonlinear load. The main focus of this chapter is to identify the presence of propagating ripples and the effect these ripples have on the fuel cell's voltage and current waveforms.

## **4.1 Fuel Cell Power System**

### **4.1.1 Stacked SOFC**

A single unit SOFC can generate a maximum of 1 V at a current density of 0.1 A/cm<sup>2</sup>, which is a very low value to power any electrical circuit. The fuel cell power can be increased by connecting single units of fuel cell in series or parallel. This process is termed as stacking. Since the research carried out in this thesis is based on simulations, an electrical stacking model using series and parallel connections of single units of fuel cell is used. Using a series connection of 48 single unit fuel cells, an SOFC fuel cell with an output voltage of 46.5 V is obtained. Nine units of the series connection are then connected in parallel to provide a fuel cell output current of 8.6 A. The SOFC fuel cell output voltage and current were arbitrarily chosen to represent a 400 W fuel cell. It is assumed that the physical parameters, such as temperature, fuel pressure, fuel volume and air volume are the same and kept constant in each single unit fuel cell so that the stacked fuel cell voltage and current remain constant. The physical parameters of the modeled SOFC stack are the same as the unit cell modeled in Chapter 3, as given in Appendix A. The stacked model was found to be an adequate numerical model for the purpose of investigating ripple current. However, it should be pointed out that stacking for an SOFC is a complex process, as the fuel cell's container should also be capable of withstanding the high temperature required for the electrochemical process while being inert to the chemical activity within it [62].

### **4.1.2 SOFC Power Circuit**

The stacked SOFC can be implemented for various applications such as standalone power systems, automotive power circuits and part of a hybrid power system along with other renewable

energy sources. As the focus of this chapter, is to identify the exact nature of ripple propagation, a standalone power system is considered for further analysis. In most practical standalone power system scenarios, the fuel cell is expected to power AC devices of voltage ratings higher than 46 V. Though the fuel cell voltage can be increased by further increasing the stack size, it is more convenient to use a boost converter. Following the boost converter, a DC-AC converter (inverter), is required to convert the cell DC voltage to AC and supply it to the required linear or nonlinear load. Figure 4.1 shows the circuit of a typical standalone fuel cell power circuit. Each power stage is described in the following sections followed by a waveform analysis.

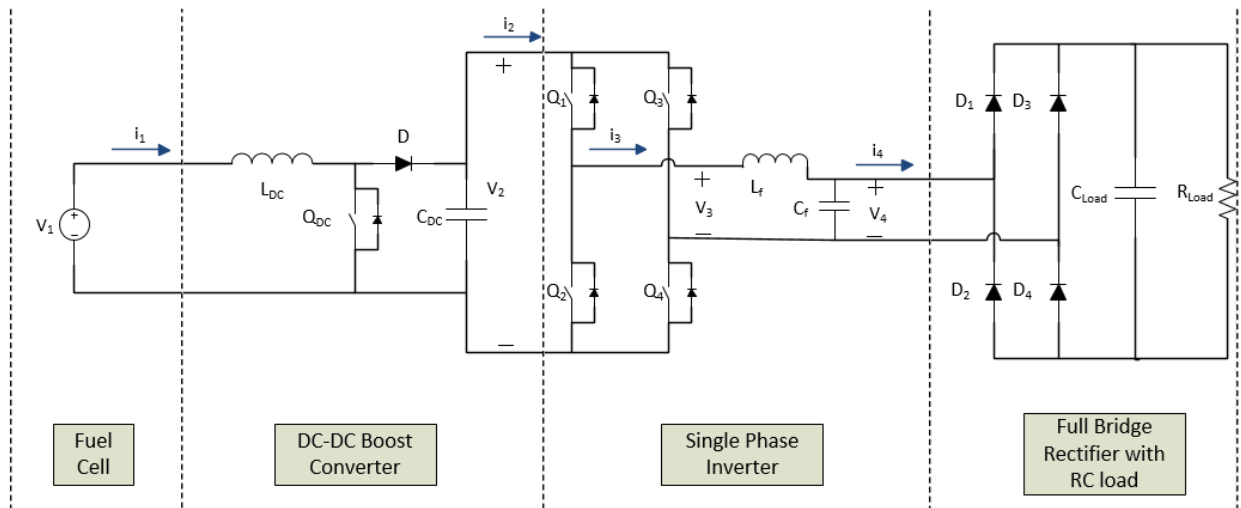


Figure 4.1: Circuit for Ripple Analysis

### 4.1.3 DC-DC Boost Converter

The Boost Converter is a DC-DC power converter with an output voltage greater than its input voltage [63]. It belongs to the class of switched mode power supplies.

The basic topology of the DC-DC boost converter is shown in Fig. 4.2. The inductor ( $L_{DC}$ ) stores energy when the switch ( $Q_{DC}$ ) is “ON.” The diode ( $D$ ), being reverse biased, isolates the

inductor from the output stage. When the switch is turned “OFF”, the energy stored in the inductor and of the source is transferred to the output capacitor, resulting in an output voltage higher than the input voltage. This operation is dependent on the duty ratio ( $d$ ) of the switching signal, which is defined as the ratio of the ON duration of the switch to the time period of the switching cycle.

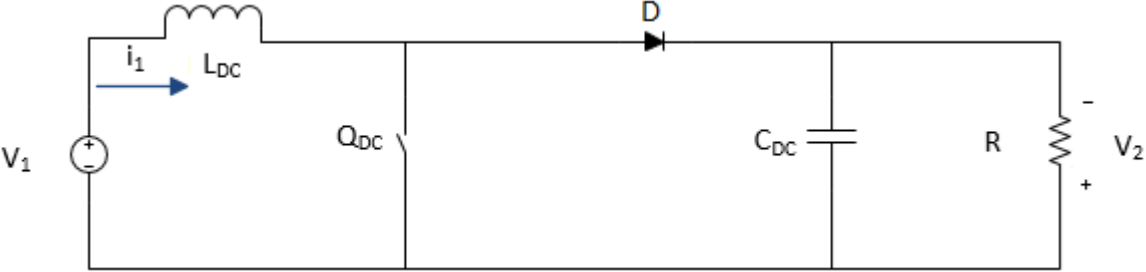


Figure 4.2: DC-DC Boost Converter

The converter operation is directly related to the “duty ratio” of the switching signal. Referring to Figure 4.3, the duty ratio can be numerically expressed as:

$$d = \frac{t_{on}}{T_s} \tag{4.1}$$

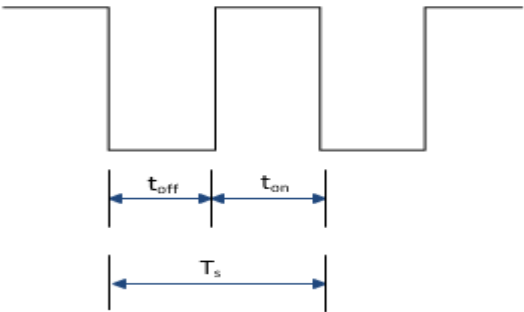


Figure 4.3: Definition of Duty Ratio

where,  $t_{on}$  is the time period during which the switch  $Q_{DC}$  is “ON” while  $T_s$  is the time period for one switching cycle.

If  $V_2$  is the output voltage and  $V_1$  is the input voltage, then the input and output voltages are related to the duty ratio (d) as:

$$\frac{V_2}{V_1} = \frac{1}{1-d} \quad (4.2)$$

In general, DC-DC converters are operated at higher frequencies. This allows the use of physically smaller values of inductor and filter capacitors. Hence, the frequency and parameter selection are both considered while implementing the boost converter. In this thesis, an IGBT boost converter was implemented.

The inductor and capacitor values were calculated by using the required duty cycle and input/output voltage characteristics [63]. The input inductor can be calculated as:

$$L_{DC} = \frac{V_1 * (V_2 - V_1)}{\Delta I_2 * f_{DC} * V_2} \quad (4.3)$$

where,  $L_{DC}$  is the input inductor,  $f_{DC}$  is the switching frequency and  $\Delta I_2$  is the estimated current ripple.

Similarly, the output capacitor is calculated as:

$$C_{DC} = \frac{i_2 * d}{f_{DC} * \Delta V_2} \quad (4.4)$$

where,  $C_{DC}$  is the output capacitor and  $\Delta V_2$  is the desired output voltage ripple.

The estimated passive parameters are recorded along with the voltage/current and switching parameters in Table 4.1.

Table 4.1: DC-DC Boost Converter Parameters

<i>Parameter</i>	<i>Value</i>
$L_{DC}$	622 mH
$C_{DC}$	2.2 mF
$V_1$	46.5 V
$i_i$	8.6 A
<i>Duty Cycle (d)</i>	0.535
<i>Switching Frequency</i>	1000 Hz

#### 4.1.4 Inverter

The inverter converts DC power to AC power. Inverters are classified based on the output waveform, which can be square, quasi-sine or sinusoidal [64]. Since a sine wave output is used by most electrical devices, the sine wave inverter is the most preferred design. A square wave inverter output can be converted to a sine output using suitable passive filters.

Figure 4.4 shows a single-phase full bridge inverter. Using bipolar PWM switching scheme, the diagonally opposite switches are switched in pairs. The bipolar switching pattern produces an output voltage which ranges from zero to  $+V_2$  and zero to  $-V_2$ .

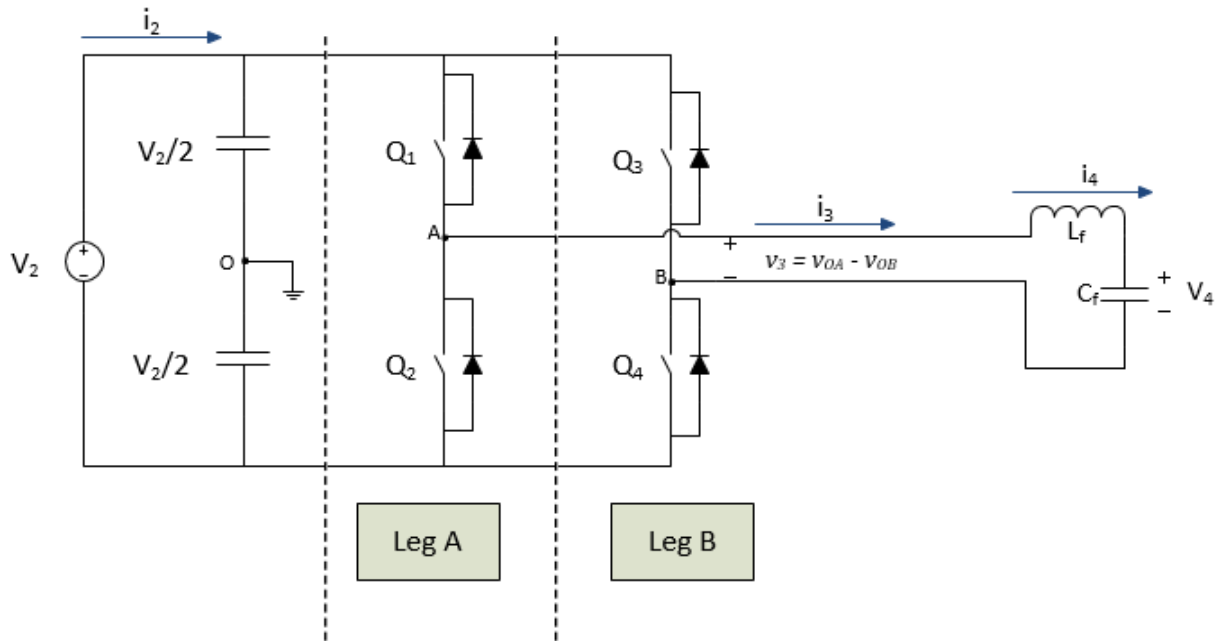


Figure 4.4: Single Phase Full Bridge Inverter

If  $V_2$  is the input voltage,

Voltage output from A:

$$v_{OA} = \frac{1}{2} V_2 \quad (4.5)$$

Voltage output from B:

$$v_{OB} = -\frac{1}{2} V_2 = -v_{OA} \quad (4.6)$$

The sum total output voltage is given by:

$$v_3 = v_{OA} - v_{OB} = 2v_{OA} \quad (4.7)$$

With the use of LC filter, the square wave output of the inverter is converted to a sinusoidal signal. If  $v_4$  is the sinusoidal output of the inverter, the fundamental component of the output voltage ( $v_{41}$ ) is given by:

$$v_{41} = v_4 = \sqrt{2}V_4 \sin \omega_1 t \quad (4.8)$$

where,  $\omega_1$  is the fundamental frequency and  $V_4$  is the RMS voltage.

In the presence of a nonresistive load, the output current would be out of phase with the output voltage. If  $\phi$  is the phase angle by which the current is out of phase with respect to the output voltage, then the fundamental component of the output current ( $i_{41}$ ) is given by:

$$i_{41} = \sqrt{2}I_4 \sin(\omega_1 t - \phi) \quad (4.9)$$

where,  $I_4$  is the RMS inverter current.

Assuming no power is lost or stored by the filter, the input power should be equal to the output power. Hence,

$$V_2 i_2^* = v_{41} i_{41} \quad (4.10)$$

where,  $i_2^*$  is the DC side current that consists of the DC component and ripple frequencies.

Using equations (4.8)-(4.10), the input current is given by:

$$i_2^* = I_2 - \sqrt{2}I_{22} \cos(2\omega_1 t - \phi) \quad (4.11)$$

where,

$$I_2 = \frac{V_4 I_4}{V_2} \cos \phi \quad (4.12)$$

and

$$I_{22} = \frac{1}{\sqrt{2}} \frac{V_4 I_4}{V_2} \quad (4.13)$$

From equation (4.11) it is observed that, in the presence of a nonresistive load, the DC source current of the inverter, also referred to as the DC link current, is composed of a DC signal ( $I_2$ ) and the second harmonic component of the inverter output current. The second order component is referred to as the source ripple and is usually smoothed out by a source capacitor. The details of such nonlinearity in inverters have been extensively discussed in the literature for single phase inverter systems [65]-[68]. As concluded by Cross et al. [69], the DC link current is present for both nonlinear and unbalanced loads.

Other than passive filters, the DC link current can be minimized by using control schemes to control the output of the inverter so that minimal DC link current is produced [70]. Ripple propagation due to nonlinear or unbalanced load is not a phenomenon that is only confined to fuel cells. Most renewable energy sources exhibit similar ripple propagation [71]-[74].

As explained in the previous chapter, due to the double-layer capacitance, the propagating second harmonic component, from an inverter, can degrade the cell's performance both physically and electrically. A full-bridge single-phase inverter has been implemented to enable the study of ripple propagation for the modeled SOFC. Table 4.2 records the inverter parameters as used in this thesis.

Table 4.2: Inverter Parameters

<b>Parameter</b>	<b>Value</b>
$L_f$	2 mH
$C_f$	30 $\mu F$
$V_2$	100 V
$i_2$	4 A
SPWM	Modulating = 60 Hz
	Carrier = 1000 Hz

### 4.1.5 Full-bridge Diode Rectifier

In this thesis, a full-bridge diode rectifier has been used as a nonlinear load. The rectifier is followed by a parallel connection of a capacitor and a resistor as the load of the rectifier. The RC parameters are given in Table 4.3.

Table 4.3: Nonlinear Load Parameters

<b>Load Magnitude</b>	<b>RC Values</b>
160 Watts	$R_{Load} = 66 \Omega$ ; $C_{Load} = 10\mu F$
240 Watts	$R_{Load} = 42 \Omega$ ; $C_{Load} = 10\mu F$
400 Watts	$R_{Load} = 23 \Omega$ ; $C_{Load} = 10\mu F$

## 4.2 Performance of the Fuel Cell System

The fuel cell system, as simulated in MATLAB/Simulink environment, is used to determine the extent of ripple propagation for a resistive load and a nonlinear load.

### 4.2.1 Fuel Cell System under Resistive Load

The fuel cell system with a resistive load is shown in Figure 4.5. A resistive load of 160 Watts is selected.

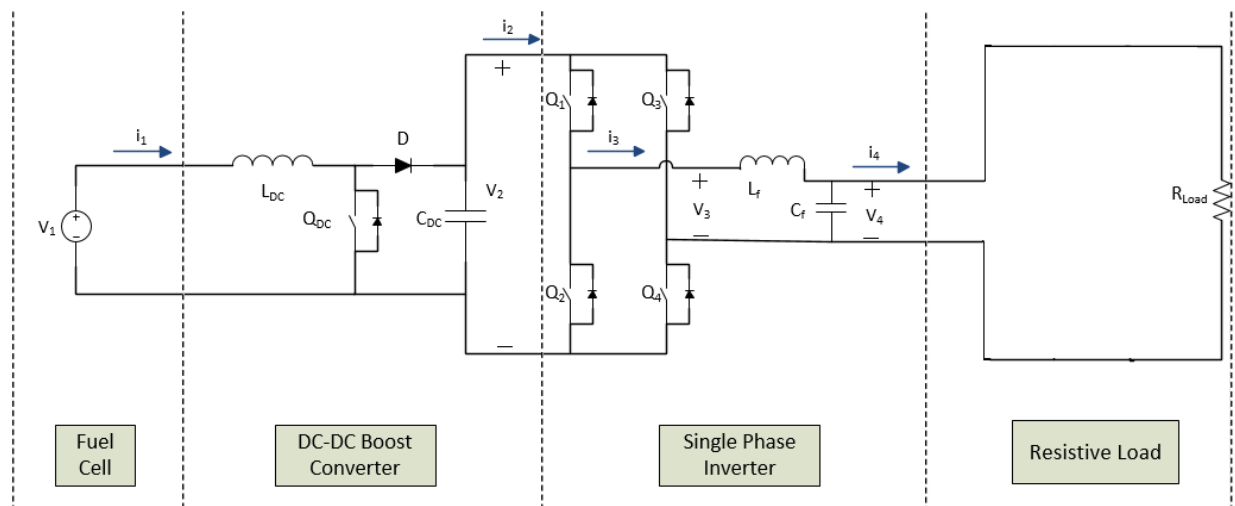


Figure 4.5: The Fuel Cell System with a Resistive Load

Figure 4.6 (a) shows the steady state voltage waveforms while Figure 4.6 (b) shows the steady state current waveforms at various stages in the system.

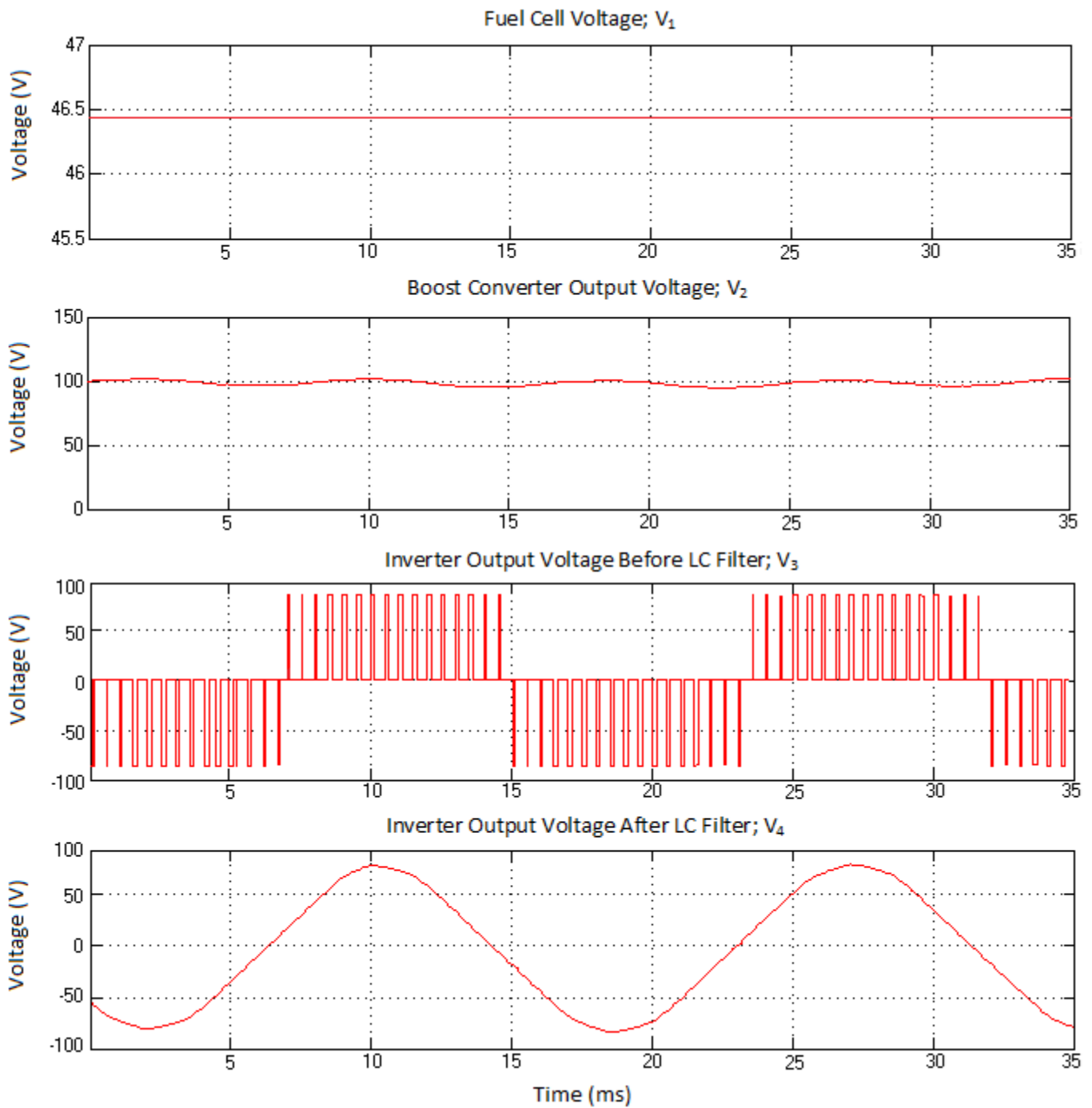


Figure 4.6 (a): Voltage Waveforms under Resistive Load of 160 W

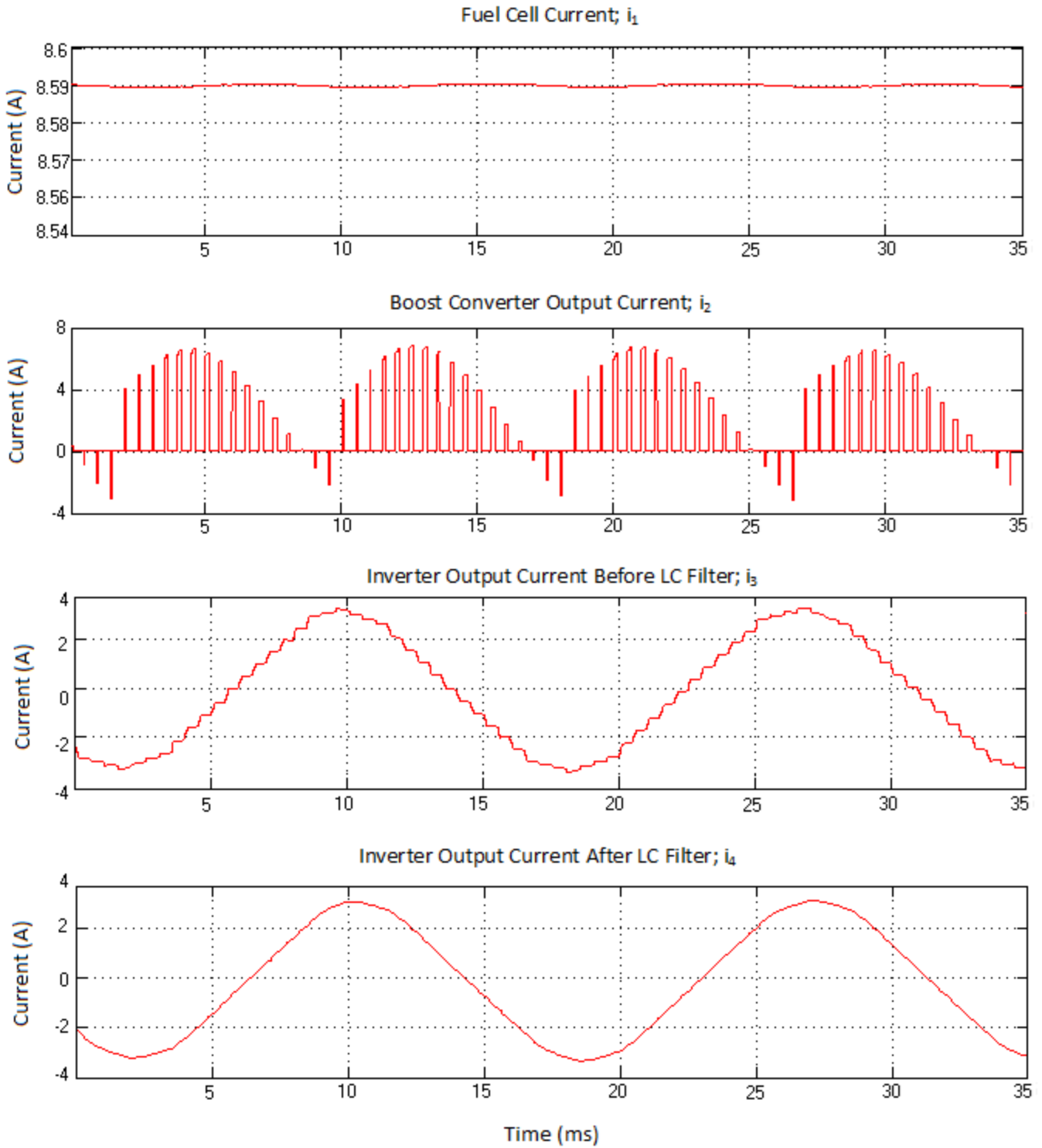


Figure 4.6 (b): Current Waveforms under Resistive Load of 160 W

Upon observing the voltage waveforms, the fuel cell voltage appears to be devoid of any harmonic ripples and shows an almost ideal DC waveform. The boost converter voltage appears to have a low frequency ripple superimposed on top of the actual waveform.

As expected, the boost converter output current contains harmonics at twice the frequency of the inverter output current. This shows the presence of second harmonic components overlaid on top of the high frequency current. The boost converter output capacitor filters out high frequency currents but, some of the second order harmonic currents appear at the input of the boost converter, which propagates to the fuel cell source. Hence, the fuel cell current, which should ideally be a DC signal, contains ripples. Since the magnitude of the current ripples is low, they are not observed on the fuel cell voltage waveform.

When analyzing the effects of ripple propagation, it is better to analyze the current waveforms as they would clearly reflect the presence of harmonics and would show deviation from ideal behavior. Figure 4.7 shows the frequency spectrum analysis of the fuel cell current with resistive load.

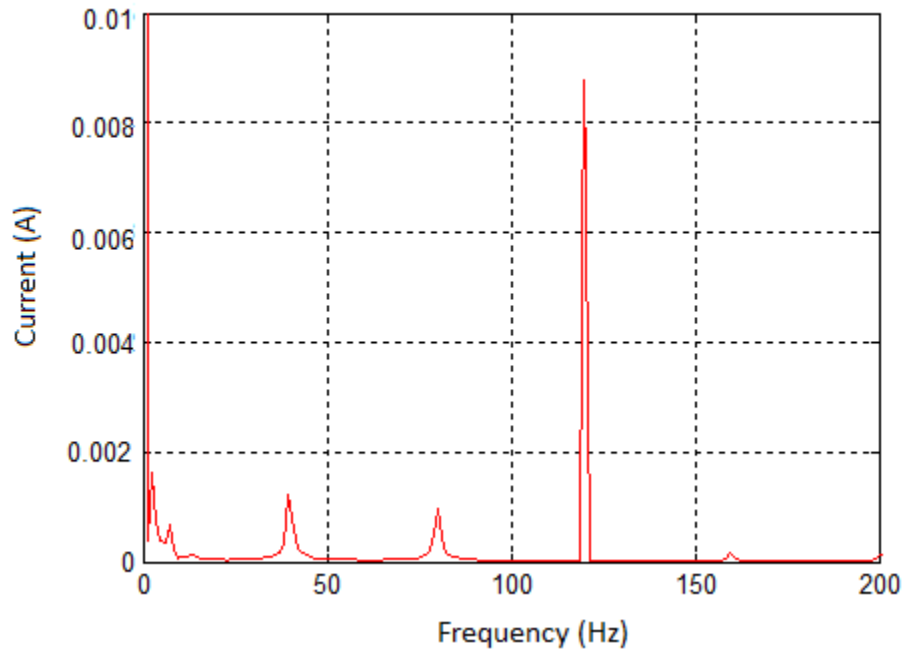


Figure 4.7: Harmonic Analysis of Fuel Cell Current under Resistive Load

Other than the second harmonic, measured at 0.009 A, minor beat frequencies between the second harmonics and the switching frequency are also observed. Though the magnitude of the ripples on the fuel cell current is very low, it demonstrates the phenomenon of ripple propagation in a fuel cell system.

### 4.2.2 The Fuel Cell System under Nonlinear Load

The resistive load in Figure 4.5 is replaced with a nonlinear load, as shown in Figure 4.1. In this instance, a full-bridge rectifier, followed by an RC load of 160 W, is used to emulate a nonlinear load. The parameters of the nonlinear load are specified in Table 4.3. Unlike a resistive load, nonlinear loads draw current of adequate harmonic contents and reactive power, with a crest factor even lower than the sine wave output of the inverter or AC mains [75]. This causes magnitude variation as well as distorting the shape of the source current to the nonlinear load. As

the magnitude of the load increases, the amount of current drawn by the load increases while higher magnitudes of harmonic and reactive components are added to the AC source. Due to this, the AC source current appears as a pulsed waveform.

The first nonlinear load simulation is for 160 W. Figure 4.8 (a) shows the voltage waveforms, while the current waveforms are shown in Figure 4.8 (b).

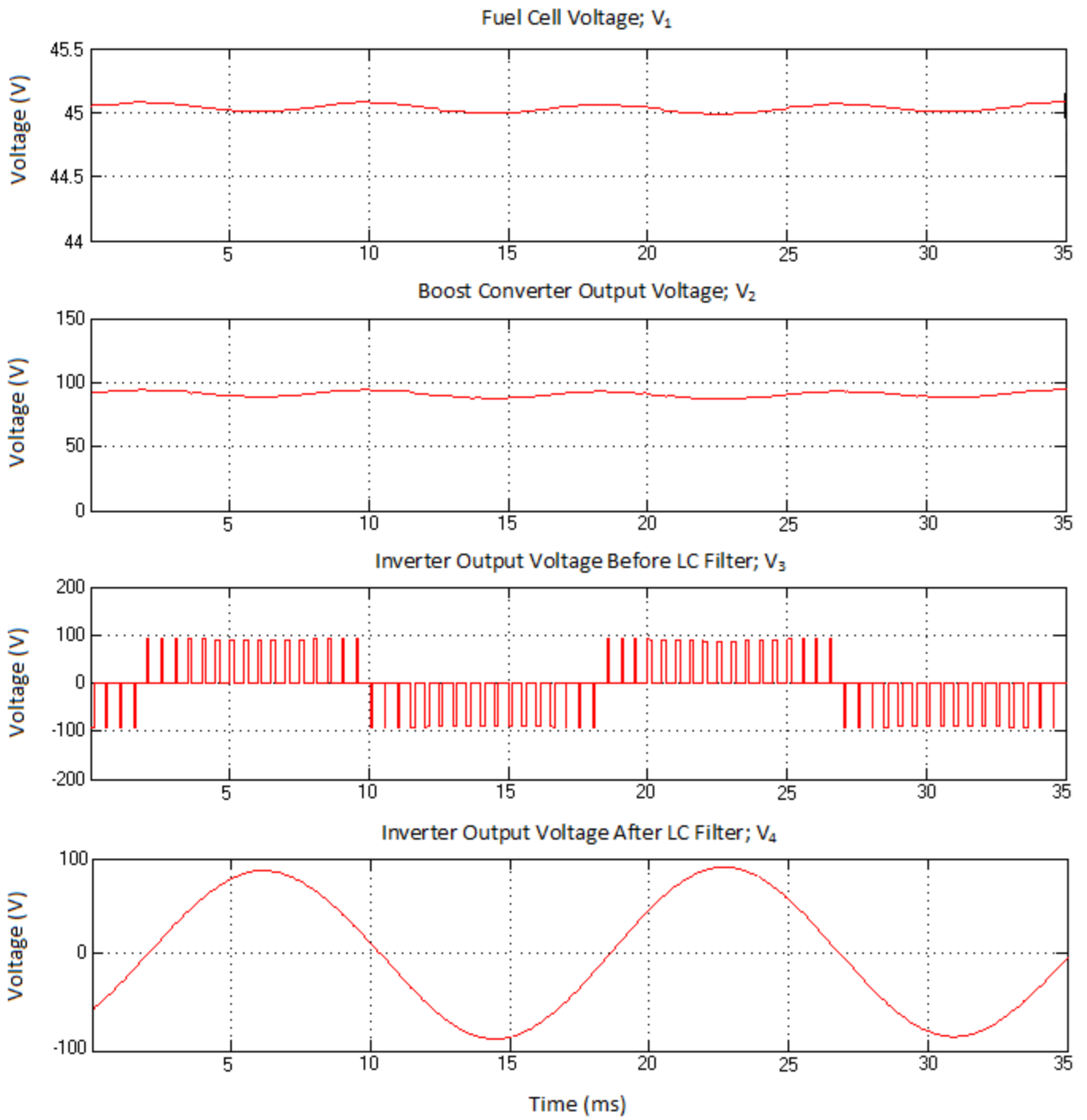


Figure 4.8 (a): Voltage Waveforms under Nonlinear Load of 160 W

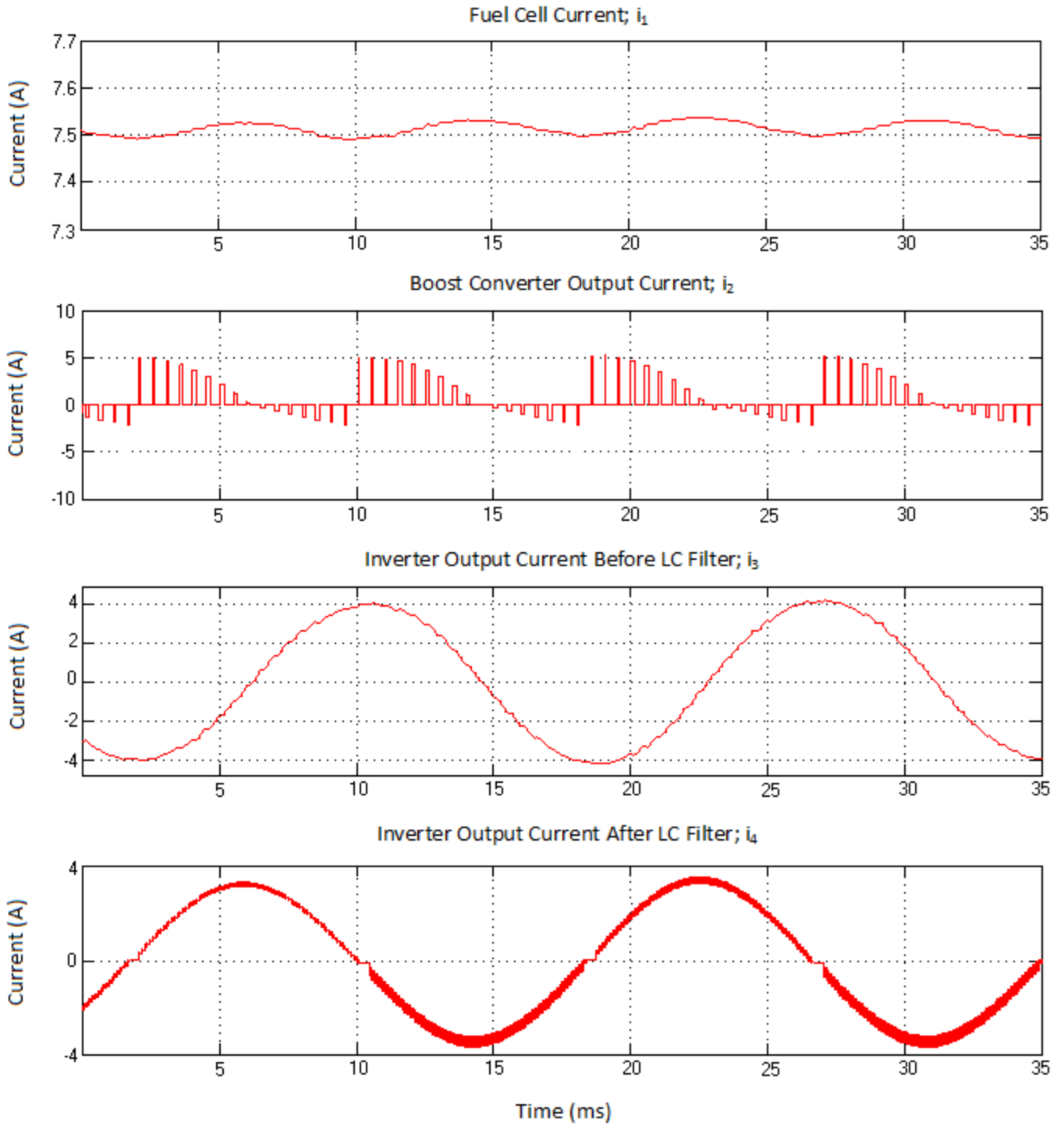


Figure 4.8 (b): Current Waveforms under Nonlinear Load of 160 W

The fuel cell voltage in Figure 4.8 (a) clearly shows the presence of a low frequency component superimposed on the DC waveform, causing the slightly sinusoidal appearance. This is once again observed in the boost converter output voltage.

The inverter load current shows distortions that are caused by the presence of the nonlinear load. The harmonic distortions are also present in the boost converter current and the fuel cell current waveforms. The nonlinear load has greatly reduced the magnitude of the fuel cell current. This can be explained by the equations in section 4.1.4, which describe the overall DC source current as comprising a DC component and a ripple component. This is confirmed by the harmonic analysis of the fuel cell current, shown in Figure 4.9.

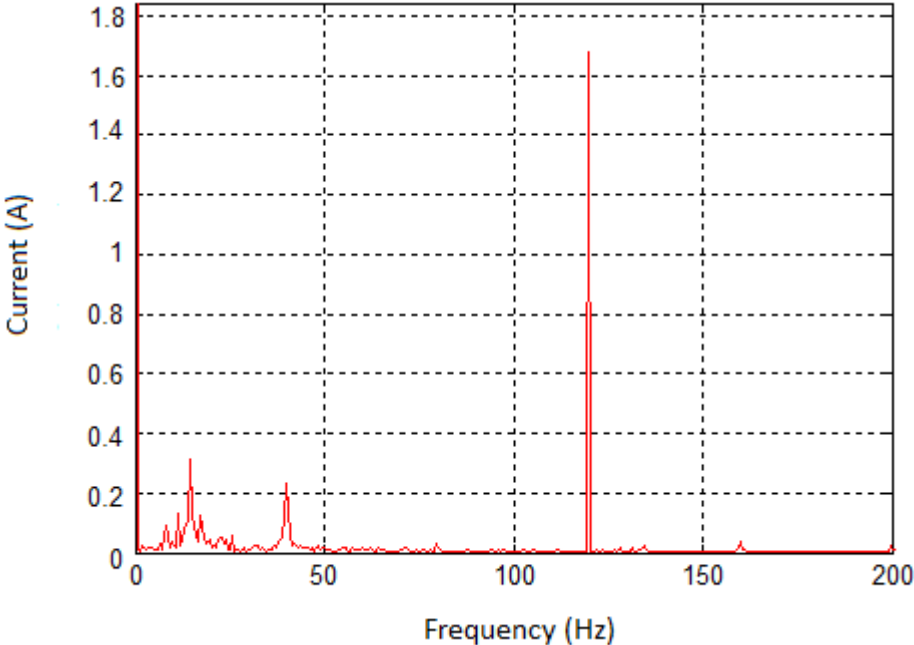


Figure 4.9: Harmonic Analysis of Fuel Cell Current under Nonlinear Load of 160 W

The harmonic analysis shows that the fuel cell current contains a 120 Hz harmonic current and other minor frequency harmonics, which are less than 0.3 A in magnitude. The overall fuel

cell current is reduced to 7.5 A and the second harmonic component is 20.18 % of the DC component.

In order to determine the extent of ripple propagation, the load should be varied in terms of magnitude and frequency. This is discussed in the following section (Section 4.3).

## **4.3 Effect of Varying Load**

### **4.3.1 Magnitude Variation**

The effect of magnitude variation is studied by increasing the nonlinear load to 240 Watts and 400 Watts. The simulation is carried out for each load condition using the circuit diagram as shown in Figure 4.1. The load parameters are given in Table 4.3.

#### ***4.3.1.1 Load value of 240 Watts***

Figure 4.10 (a) shows the system voltage waveforms for steady state conditions. The current waveforms are shown in Figure 4.10 (b).

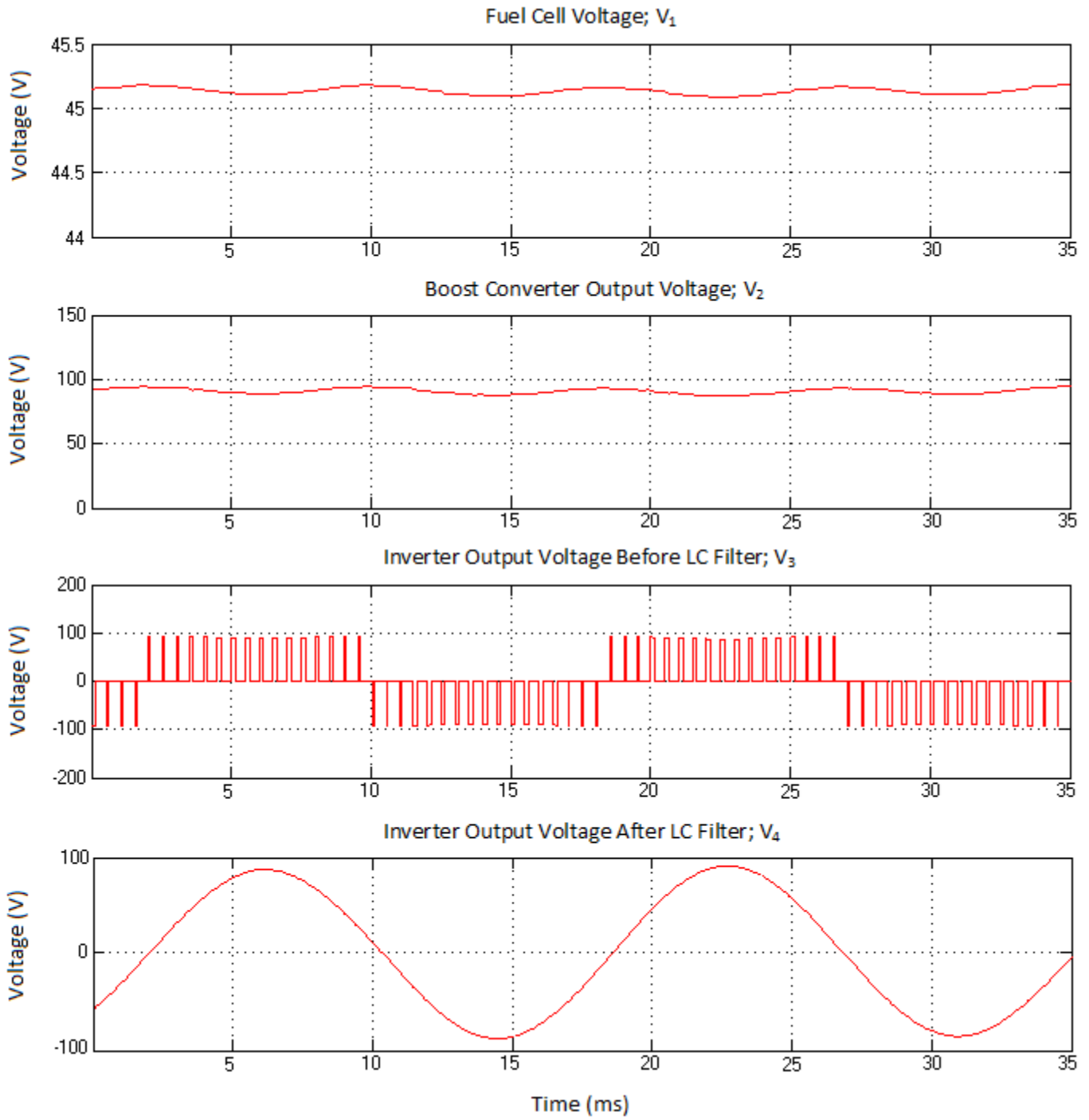


Figure 4.10 (a): Voltage Waveforms under Nonlinear Load of 240 W

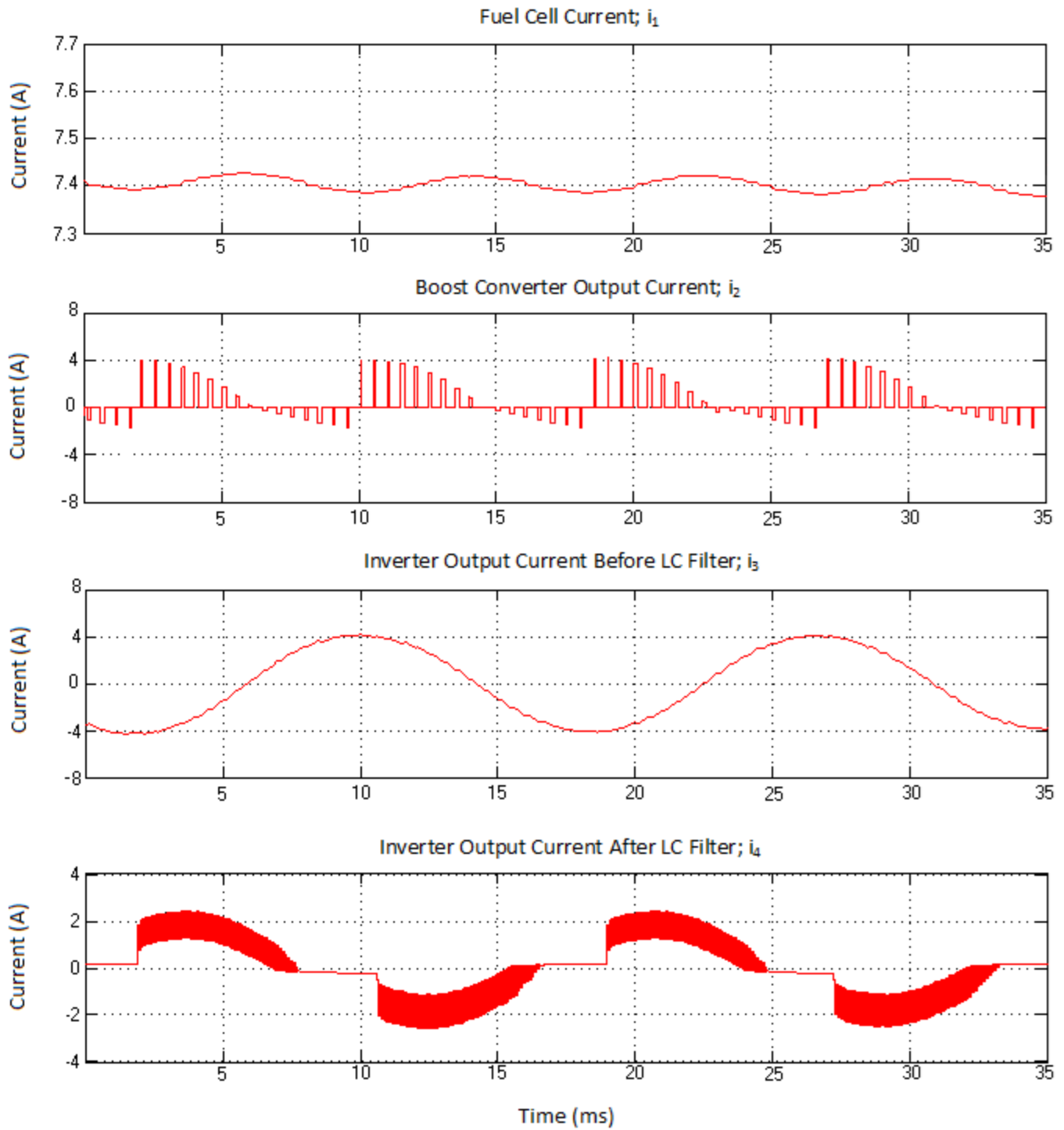


Figure 4.10 (b): Current Waveforms under Nonlinear load of 240 W

Though the fuel cell voltage waveform does show the presence of ripples, the magnitude of ripples is quite small. Due to this, the magnitude of fuel cell voltage has not altered a lot. The boost converter voltage also exhibits a low frequency ripple superimposed over the DC signal, but once again the ripple magnitude is not very high.

The nonsinusoidal shape of the waveform is explained by the increased nonlinear load magnitude. Since nonlinear loads draw currents in pulses, the increase in load magnitude increases the amount of current drawn by the load. The load is also responsible for adding harmonic current to the inverter. With higher harmonic content, the inverter current waveform appears only partially sinusoidal. Due to the increase of output harmonics there is a marked phase difference between the voltage and current waveforms. This causes an increase in DC side harmonics and their consequent propagation to the fuel cell.

The magnitude of propagating ripples is evidently higher in the fuel cell current as compared with a nonlinear load of 160 W. This is confirmed by the reduced magnitude of fuel cell current and is better explained by means of harmonic analysis.

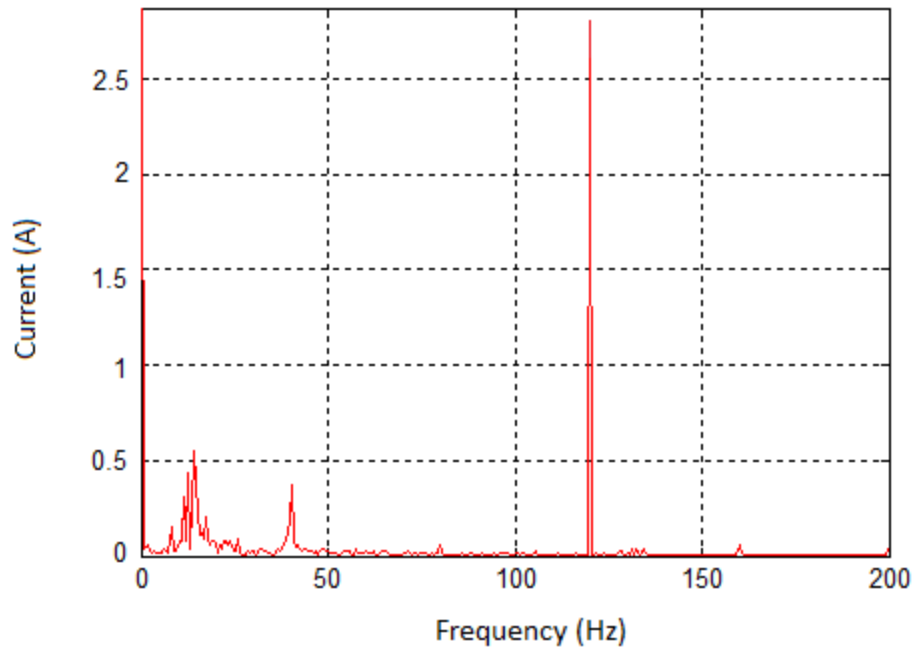


Figure 4.11: Harmonic Analysis of Fuel Cell Current under Nonlinear Load of 240 W

Harmonic analysis, as shown in Figure 4.11 reveals a higher magnitude of second harmonic. At 240 W, the second harmonic is 33.27 % of the DC component.

#### ***4.3.1.2 Load value of 400 Watts***

The nonlinear load is increased to 400 W. The voltage waveforms are given in Figure 4.12 (a), while the current waveforms are given in Figure 4.12 (b).

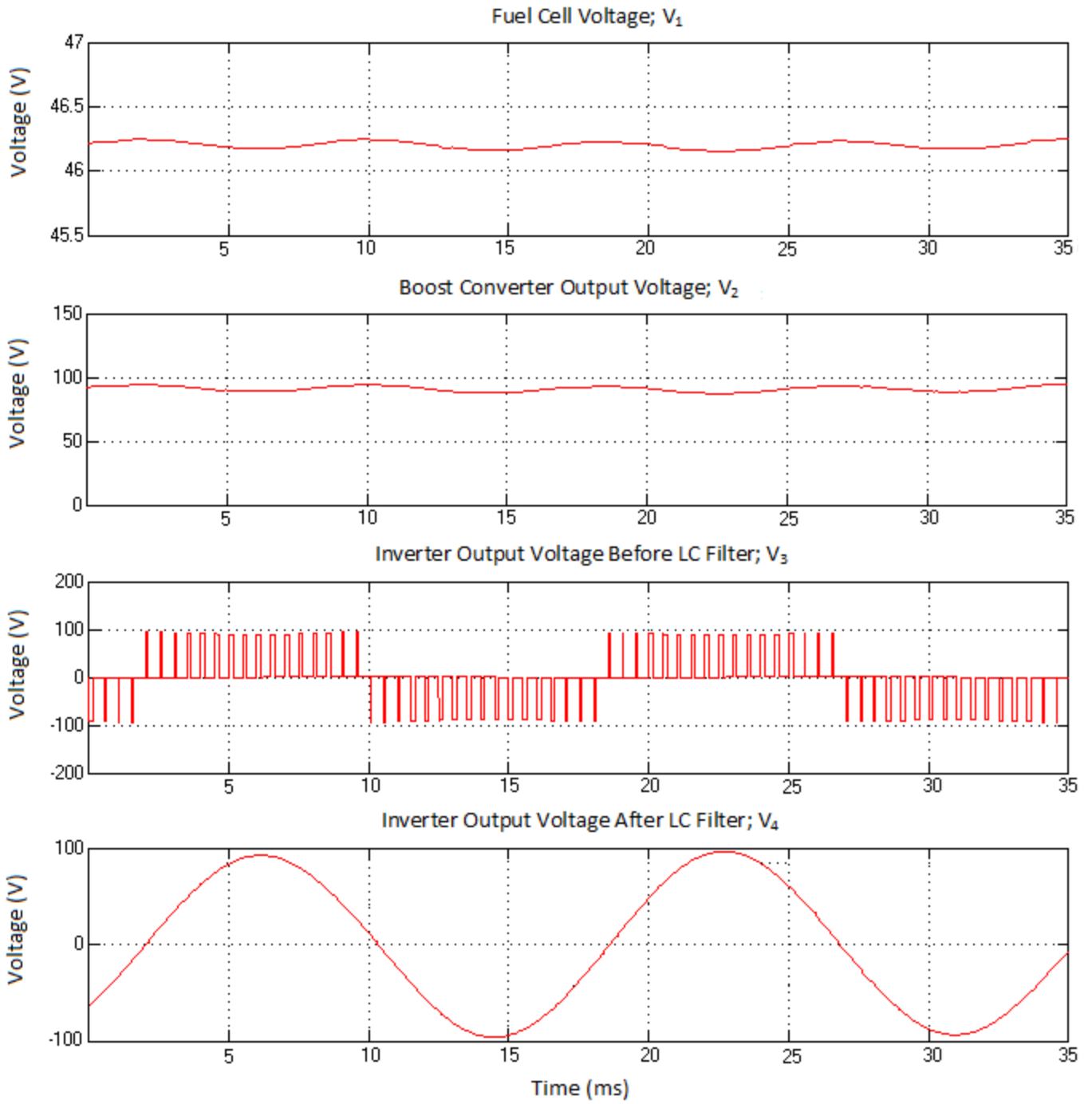


Figure 4.12 (a): Voltage Waveforms under Nonlinear Load of 400 W

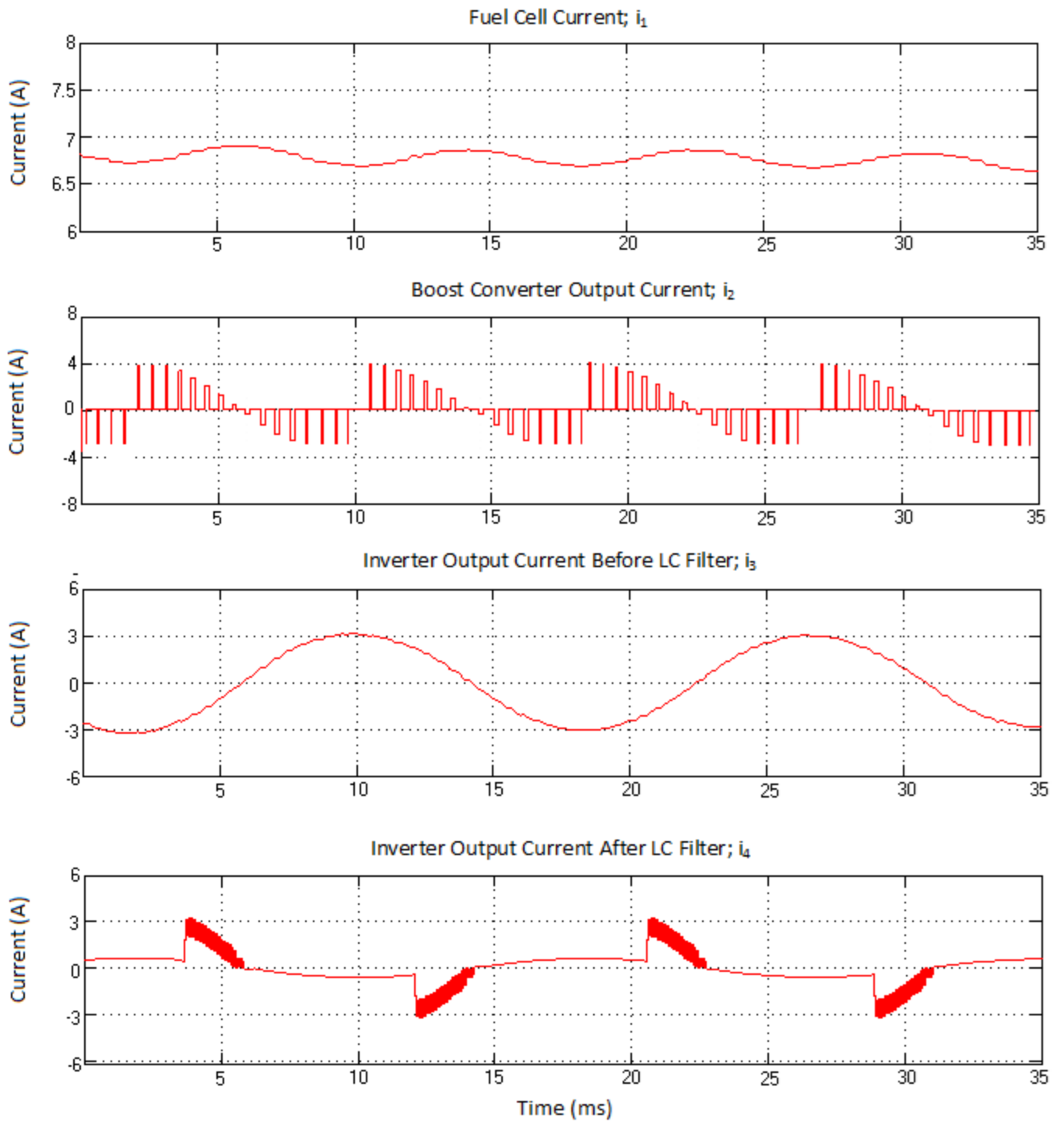


Figure 4.12 (b): Current Waveforms under Nonlinear Load of 400 W

The voltage waveforms differ marginally as compared to the previous case (Section 4.3.1.2). The low frequency ripples are clearly visible on both the boost converter and fuel cell voltages, but are not significantly high.

Based on the discussion on harmonic distortion caused by nonlinear loads, the shape of the inverter current waveform can be attributed to the presence of high magnitude harmonics, at frequencies other than the fundamental, causing evident phase difference between the current and voltage waveforms. This explains the reduced fuel cell current magnitude. The DC and other harmonic contents of fuel cell current are studied through harmonic analysis, as shown in Figure 4.13.

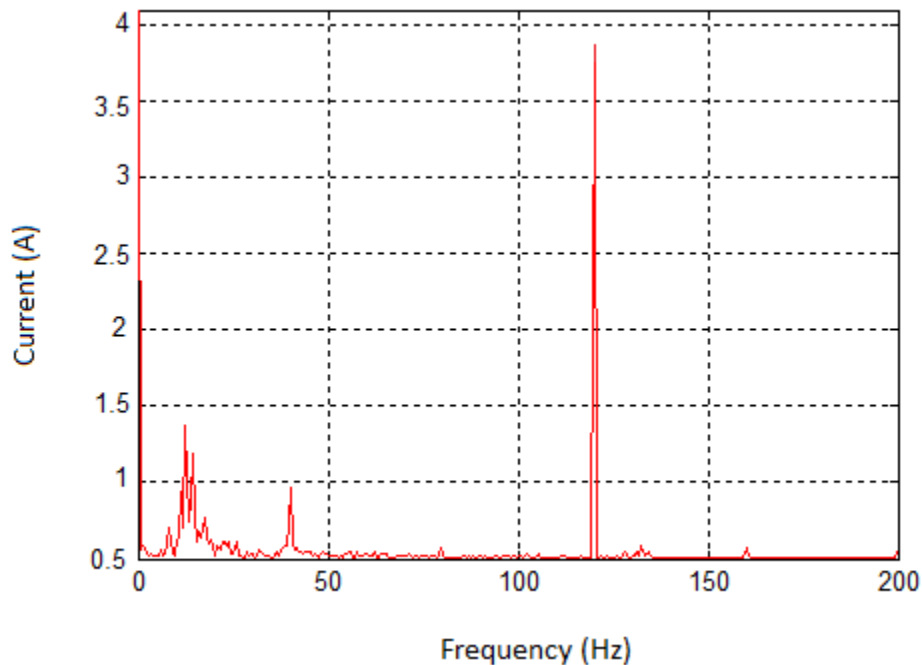


Figure 4.13: Harmonic Analysis of Fuel Cell Current under Nonlinear Load of 400 W

The harmonic analysis shows a second harmonic of 3.82 A, which is 44.37% of DC value. This is much higher than the harmonic measured for 160 and 240 W.

Table 4.4 records the DC, second harmonic component of the fuel cell current and the amount of power extracted from the fuel cell, under three nonlinear load conditions.

*Table 4.4: DC and Second Harmonic Magnitudes of Fuel Cell Current under Three Nonlinear Loads*

<b>Load Value (Watts)</b>	<b>Harmonic Order</b>	<b>Mag. (A)</b>	<b>%DC</b>	<b>Fuel Cell Power (Watts)</b>
160	DC	8.5	100	338.78
	2 <sup>nd</sup>	1.74	20.18	
240	DC	8.46	100	335.22
	2 <sup>nd</sup>	2.86	33.27	
400	DC	8.4	100	310.21
	2 <sup>nd</sup>	3.82	44.37	

Analyzing Table 4.4, it can be concluded that an increase in load magnitude increases ripple propagation and lowers the overall fuel cell current. As indicated by the power levels, an increase in the second harmonic component reduces the overall power that can be extracted from the fuel cell.

### **4.3.2 Frequency Variation**

In the previous sections, the inverter is operated at 60 Hz. As the effect of ripple propagation is also dependent on the operating frequency of the inverter (equation (4.11)), it is important to analyze the effects of frequency variation on ripple propagation.

For this purpose, the inverter is operated at frequencies of 120 and 240 Hz and the ripple propagation is assessed in the following sections (Section 4.3.2.1 & 4.3.2.2). A load of 160 W is maintained for both frequency variations.

### ***4.3.2.1 Frequency of 120 Hz***

The voltage waveforms are shown in Figure 4.14 (a), while the current waveforms are shown in Figure 4.14 (b).

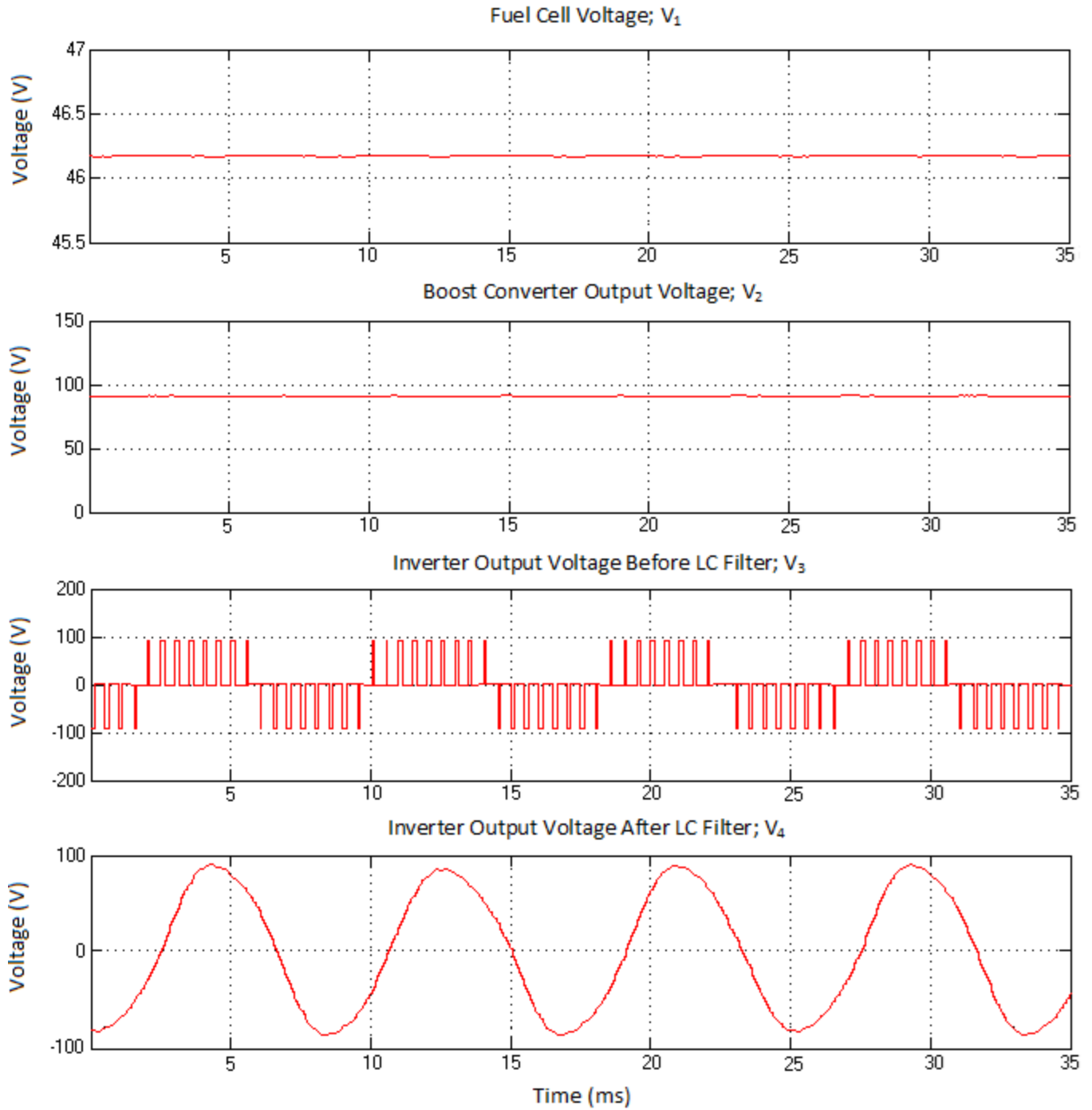


Figure 4.14 (a): Voltage Waveforms at Inverter Operating at 120 Hz under Nonlinear Load of 160 W

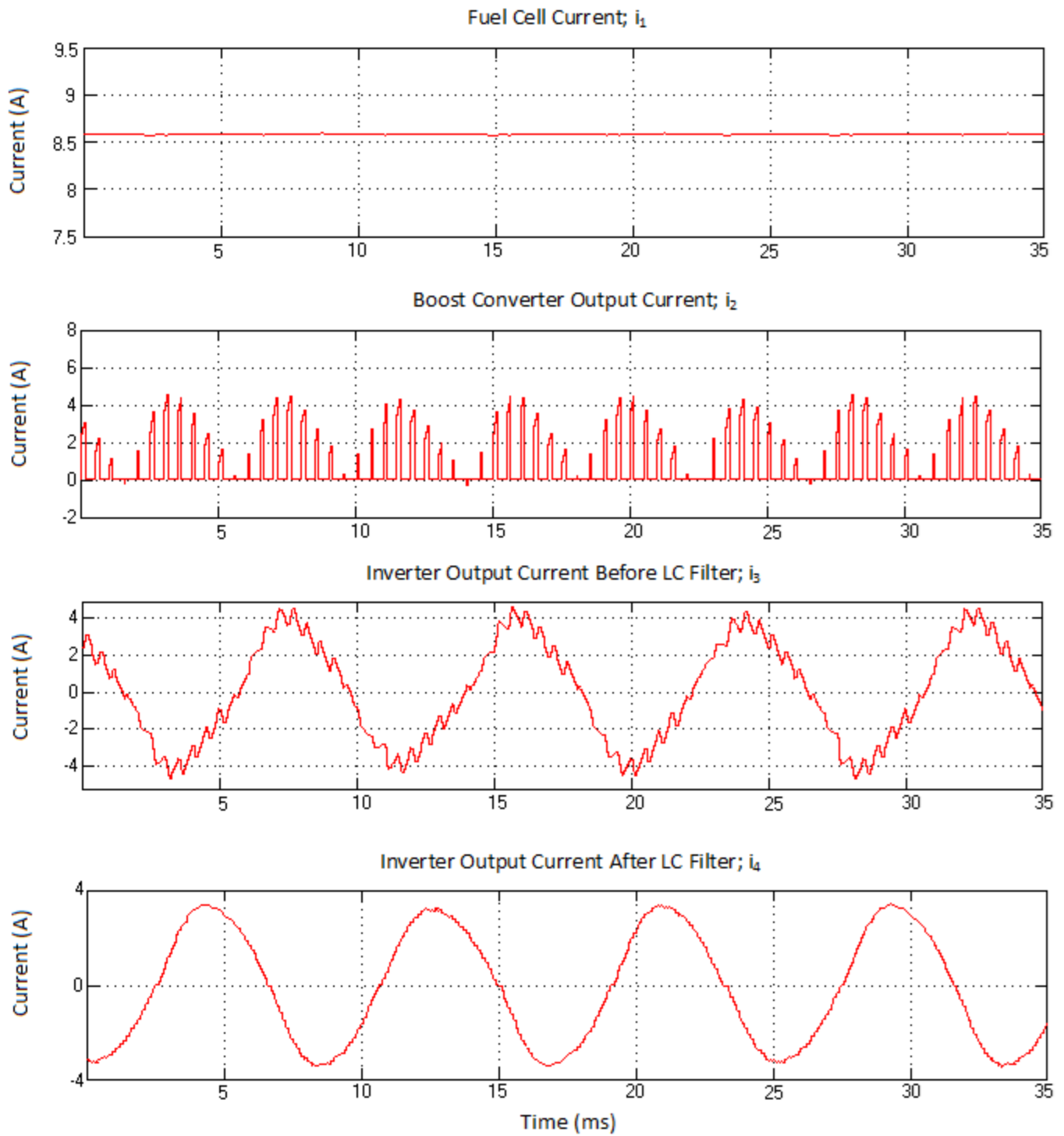


Figure 4.14 (b): Current Waveforms at Inverter Operating at 120 Hz under Nonlinear Load of 160 W

The voltage waveforms, for fuel cell and boost converter, show the presence of a low frequency ripple, but as compared to waveforms observed in Section 4.2.2, the ripples are very low in magnitude.

The inverter current displays slight distortions, and when compared with the voltage waveform, a small phase difference is observed. The fuel cell current shows minimum distortions and the current magnitude is higher than the one observed in Section 4.2.2. The percentage of harmonics and DC components is further analyzed using harmonic analysis, as shown in Figure 4.15.

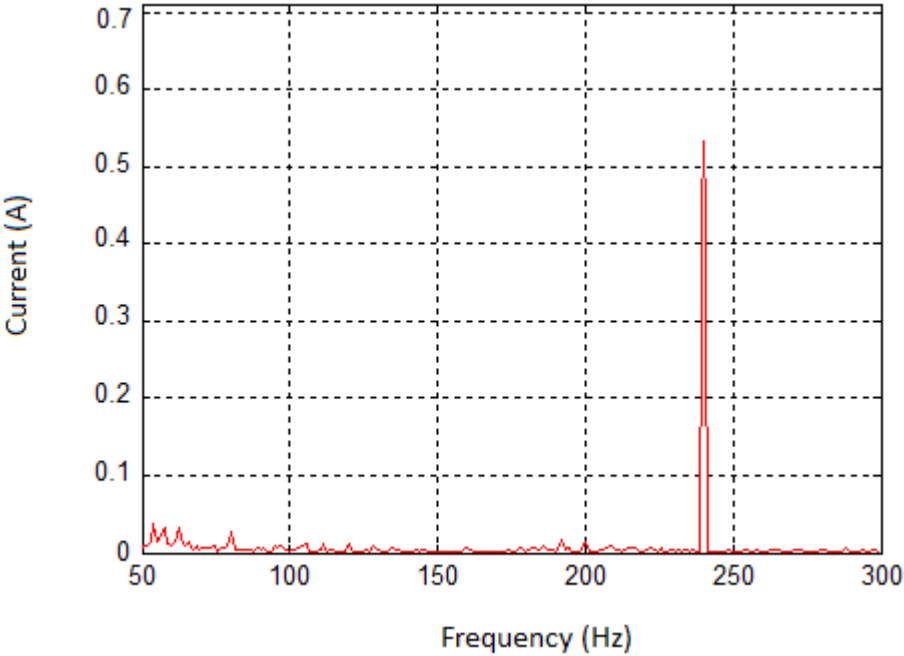


Figure 4.15: Harmonic Analysis of Fuel Cell Current under Nonlinear Load of 160 W and Operated at 120 Hz

The frequency spectrum analysis shows a second harmonic component of 0.53 A, which is 6.18 % of the DC value. The magnitude of the beat frequencies is lower than 0.02 A.

### ***4.3.2.2 Frequency of 240 Hz***

The voltage and current waveforms are shown in Figures 4.16 (a) and (b) respectively.

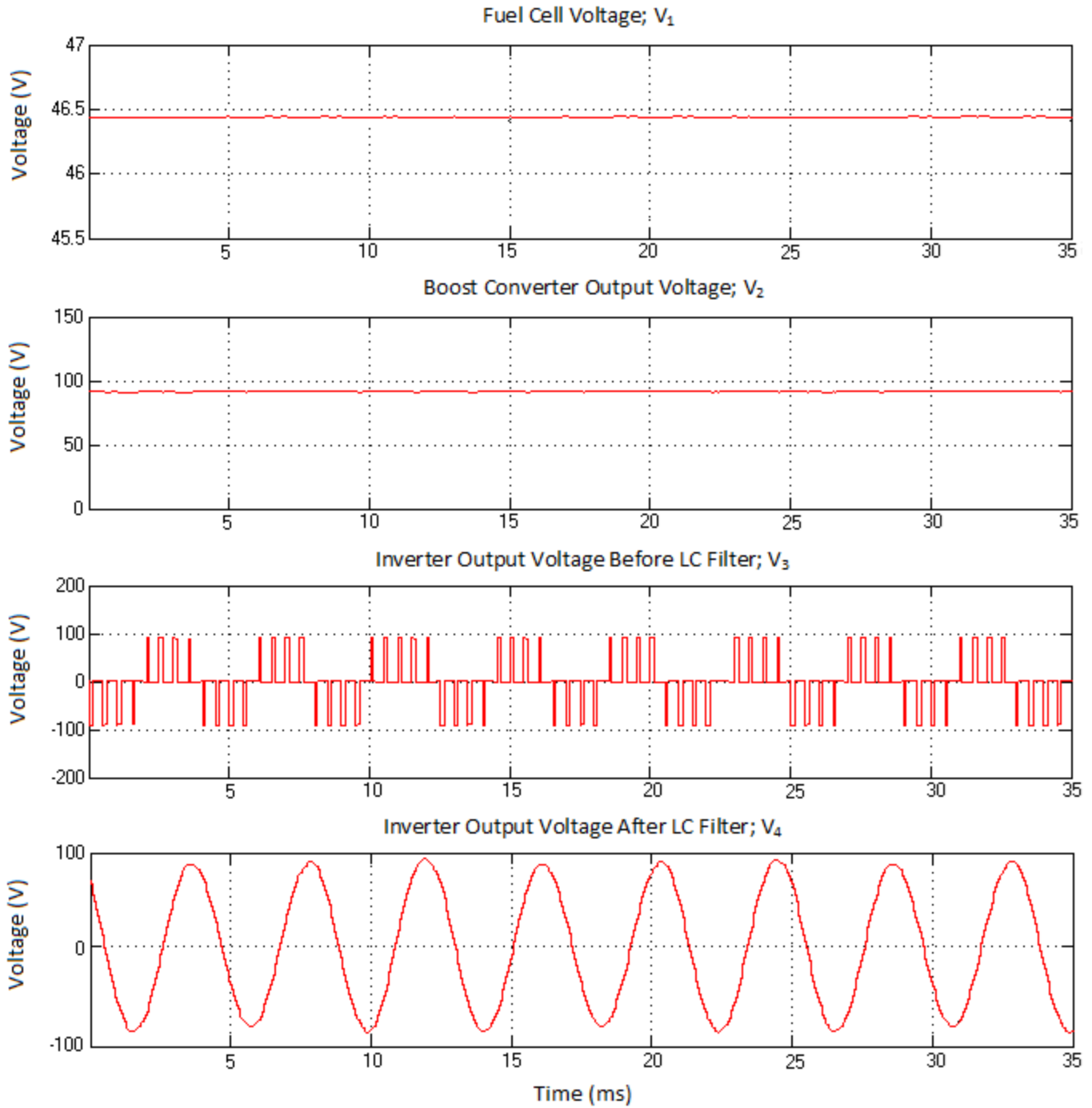


Figure 4.16 (a): Voltage Waveforms at Inverter Operating at 240 Hz under Nonlinear Load of 160 W

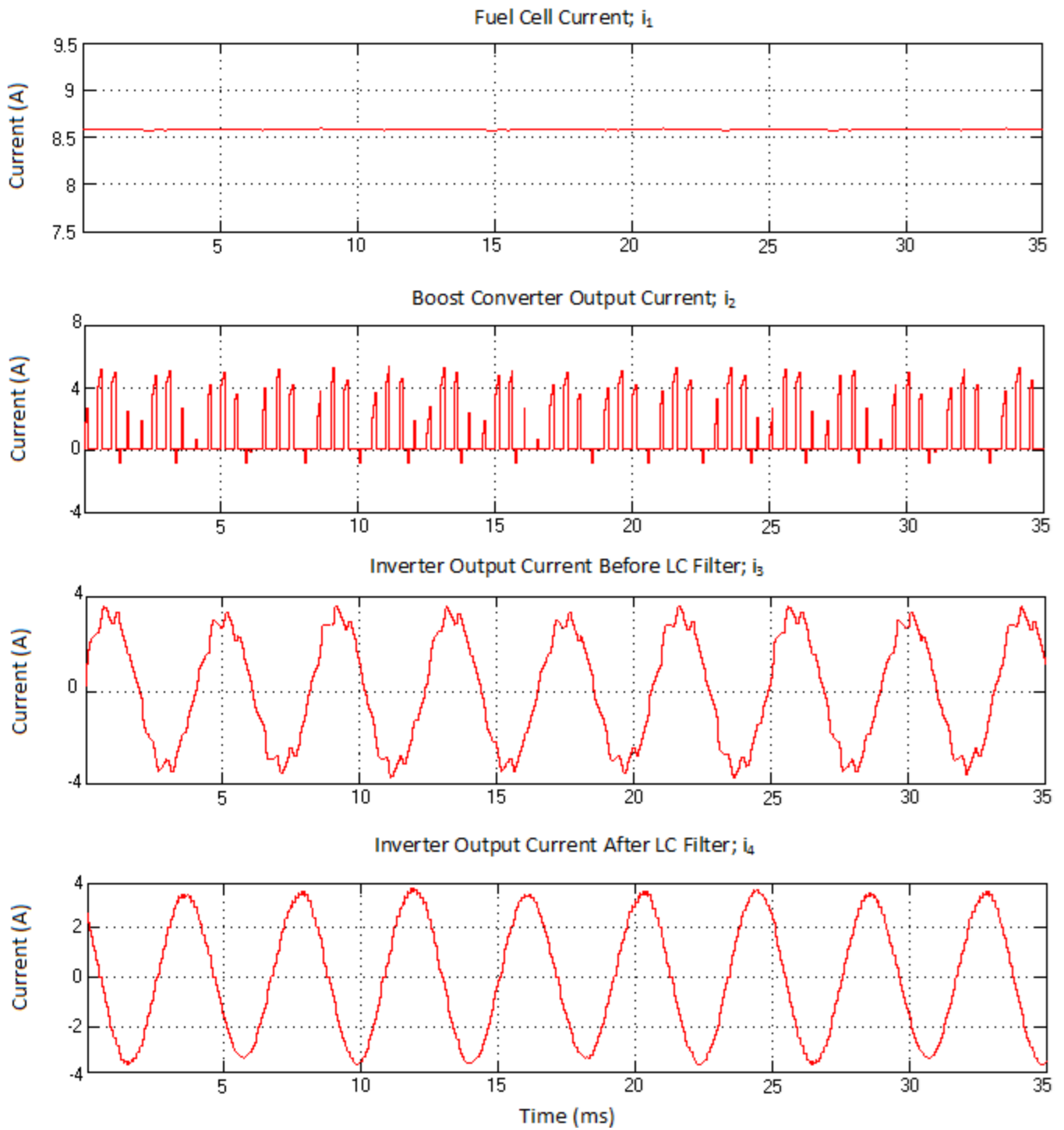


Figure 4.16 (b): Voltage Waveforms at Inverter Operating at 240 Hz under Nonlinear Load of 160 W

The fuel cell and boost converter voltage waveforms hardly show any ripples and appear almost like DC signals.

The inverter current appears purely sinusoidal and seems in phase with the inverter voltage. Due to this, minimal harmonics are present in the fuel cell current. Other than reduced ripple components, the fuel cell current magnitude has also increased. Harmonic analysis is used to confirm this.

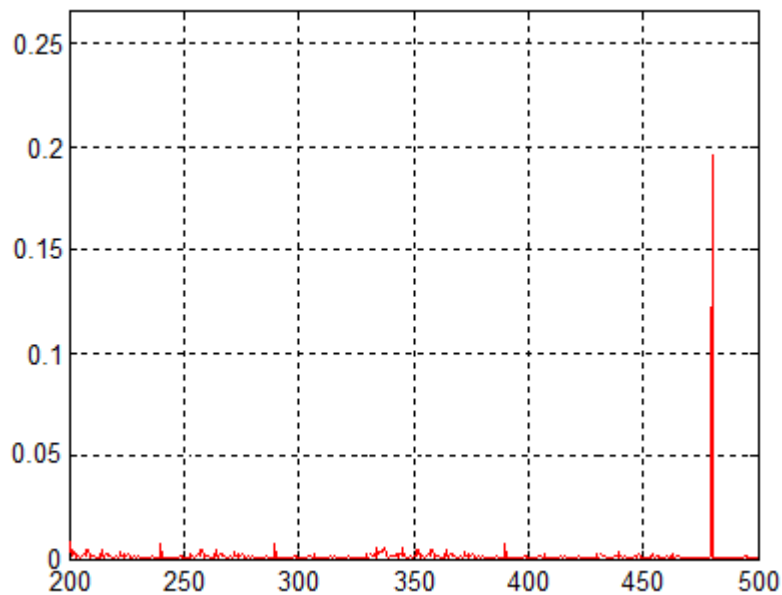


Figure 4.17: Harmonic Analysis of Fuel Cell Current under Nonlinear Load of 160 W and Operated at 240 Hz

The harmonic analysis shown in Figure 4.17 shows a second harmonic component of 0.20 A, which is 2.32% of the DC value. Other than the second harmonic, a single dominant beat frequency at a value lower than 0.02 A is also observed.

The harmonic contents of the fuel cell current under the three different frequencies are recorded in Table 4.5. Along with harmonic content, Table 4.5 also shows the effects of ripple

propagation on the amount of power that can be extracted from the fuel cell for the three inverter frequencies.

*Table 4.5: DC and Second Harmonic Magnitudes of Fuel Cell Current for Three Inverter Switching Frequencies*

<b><i>Frequency of Inverter (Hz)</i></b>	<b><i>Harmonic Order</i></b>	<b><i>Magnitude (A)</i></b>	<b><i>Percentage of DC (%)</i></b>	<b><i>Fuel Cell Power (Watts)</i></b>
60	DC	8.50	100	338.78
	2 <sup>nd</sup>	1.74	20.18	
120	DC	8.55	100	395.25
	2 <sup>nd</sup>	0.53	6.18	
240	DC	8.55	100	399.44
	2 <sup>nd</sup>	0.20	2.32	

Analyzing Table 4.5 it can be concluded that an increase in switching frequency can effectively reduce ripple propagation by pushing the inverter load harmonics to higher frequencies. Consequently, higher inverter switching frequency effectively increases the amount of power that can be extracted from the fuel cell.

However, high inverter switching frequency can result in higher switching losses. Hence, the choice of switching frequency should be decided based on the type of load that is being used. For the purpose of investigation, in this thesis, an inverter switching frequency of 60 Hz has been maintained.

## 4.7 Summary

Waveform and harmonic analysis are used to investigate ripple propagation in terms of magnitude and frequency. Under nonlinear load conditions, the ripples are more pronounced. With increasing load values, the propagating ripples also increase in magnitude. However, if the load is operated at higher frequencies, the magnitude of the propagating ripples decreases. The biggest concern for fuel cells is the presence of lower order harmonics. For a single-phase system, the second order harmonic of the inverter operating frequency is the most evident DC source harmonic, which propagates to the fuel cell and causes both physical and electrical damage. It can be expected that a high power load will always be present and hence, the need to reduce or eliminate the propagating ripples from the fuel cell is important. This is the subject of the investigation presented in the next chapter.

## **Chapter 5**

# **Fuel Cell System with Active Power Filter**

In the previous chapter, the source of harmonic propagation in a fuel cell system was identified. The presence of harmonics is more pronounced under nonlinear loads and low frequency operation of the inverter. In order to reduce the propagating ripples, large passive filters can be installed at the fuel cell output. A passive filter cannot respond to dynamic load changes and can also be the cause of harmonics due to resonance or improper filter design [76]. An active power filter is proposed as a solution to reduce the propagating ripples. In this chapter, the operation of active power filter and its implementation for the fuel cell system is described. The performance of the active power filter is evaluated in terms of its effectiveness in removing or reducing harmonic content from the fuel cell current.

## 5.1 Introduction to Active Power Filters

Unlike passive power filters, active power filters (APF) do not negate the harmonics by preventing their flow using large passive elements. Rather, an active power filter adds compensating harmonics into the system to effectively reduce the presence of disturbances [77]. Though an APF is more complex in design, its structure is compact and it is easier to tune. Since an APF actively adds compensating harmonics, variation of harmonic magnitude due to load changes can also be actively compensated.

APFs can be used as both DC and AC power systems. DC APFs are usually used only for high voltage DC applications. DC power filters can be considered as a special case of AC power filters. APFs are classified as series, shunt and hybrid filters based on their topology and function [78]. The various topologies are shown in Figure 5.1.

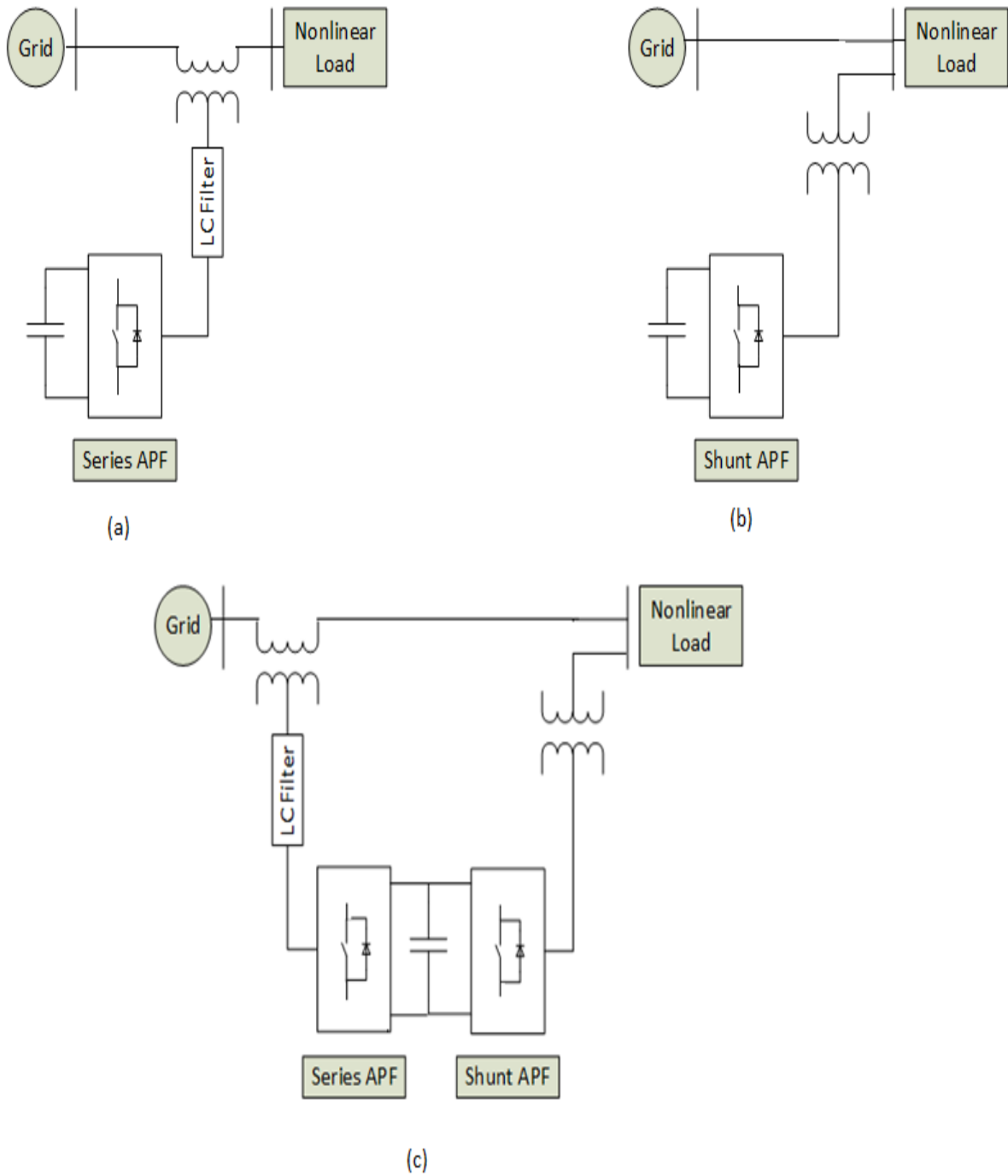


Figure 5.1: Various Active Power Filter Topologies (a) Series APF; (b) Shunt APF; (c) Hybrid APF

### **5.1.1 Series APF**

The series APF does not compensate or add current harmonics, but acts as a high impedance to current harmonics from the source side. The series topology is not commonly used because it would have to handle the full load current, which increases its current rating considerably. The main advantage of the series APF is its ability to eliminate harmonics from the voltage waveform.

### **5.1.2 Shunt APF**

The shunt APF carries only the compensating current and a small active fundamental current to compensate for system losses and sustain constant voltage [79]. Nevertheless, shunt APF can be used for reactive power compensation as well. This is the most commonly used APF configuration and can also be used for current harmonic compensation of harmonic voltage sources.

### **5.1.3 Hybrid APF**

Hybrid APFs combine shunt/series APF followed by a passive filter in order to improve the overall filter performance [80]. A series APF, which constitutes high impedance for high frequency harmonics can be combined with a parallel passive filter to provide a path for the harmonic currents of the load. Similarly, a shunt APF when combined with a parallel passive filter can effectively eliminate the bulk of lower order current harmonics [81]. Though the hybrid configuration improves the overall efficiency of the APF, it contains many power components, especially the passive filter. Since these filters are permanently connected to the system, this approach is only suitable for a single load with a predefined harmonic source.

In spite of all the advantages of the hybrid APF, the biggest disadvantage of the topology lies in its use of passive filters which makes the filter implementation stationary and would eventually require complex reconfiguration in case the system is upgraded or if a new element is added. Also, the added expenditure and maintenance of the passive filters would make the power system inappropriate for small scale applications.

#### **5.1.4 Modified Shunt Active Power Filter**

For the fuel cell system under investigation, the shunt topology is selected since it does not require a high current rating, carries only the compensating current, and is better suited for negating current harmonics. The main concern in this system is the presence of ripples in the fuel cell current, hence, the compensating current generated by the shunt active power filter should be effective in negating the ripple signal so that only the DC component remains. The main purpose of using a transformer for power filter applications is to provide a path for the compensating current to be safely added to the power system and also to remove high frequency ripples.

In order to simplify the power filter, a transformerless APF configuration can be considered. For large power systems, a transformer can be avoided if a hybrid filter is used [65]. Transformerless hybrid filters have been used in the past by researchers for various applications [82]-[87]. The added passive filter stage allows high frequency ripple elimination and can be designed for a higher frequency band to ensure minimum harmonic propagation along with the dynamic APF current compensation.

The APF current output can be directed by means of an LC filter and added in parallel to the power system [88]-[91]. Though this arrangement is similar to a hybrid power filter, it can be

considered as a shunt power filter since the passive elements are added to the converter stage as a replacement for the transformer. Hence the modified shunt APF configuration has been selected.

APF implementation involves three stages, beginning with the selection of converter topology, followed by the modulation technique and lastly the methodology used for harmonic extraction. All three stages will be discussed in detail in following sections.

## **5.2 The APF Converter Topology**

The choice of converter is based on the power requirements of the various types of nonlinear loads. The power circuit of APFs consists of a DC energy storage unit and a DC-AC converter (inverter). The DC energy storage consists of a DC source such as a battery in parallel with a capacitor. The capacitor minimizes the DC link ripple and also maintains a small ripple in steady state. For lower power applications, single-phase inverters can be used. But for higher power applications, where the amount of harmonics in the system is higher, three-phase or multi-level inverters are more suitable. The APF inverters can be further classified as “voltage source” or “current source” inverters. Since voltage source inverters are lighter, less complex and economically viable, they are commonly used as compared to current source inverters [92].

For the fuel cell system, the choice of converter differs as the converter would be required to remove harmonics from a DC signal as opposed to an AC signal. A DC-AC converter would generate a compensating signal that traverses on both positive and negative axes. This would be harmful for a DC system. Instead of using DC-AC converters, a DC-DC converter would be a better choice. A similar DC-DC converter was used by Glenting et al. [93] for removing harmonics from radar systems.

The DC-DC converter based APF uses a modified version of a DC-DC buck converter where the diode is replaced with another switching device. Figure 5.2 shows the modified shunt active power filter.

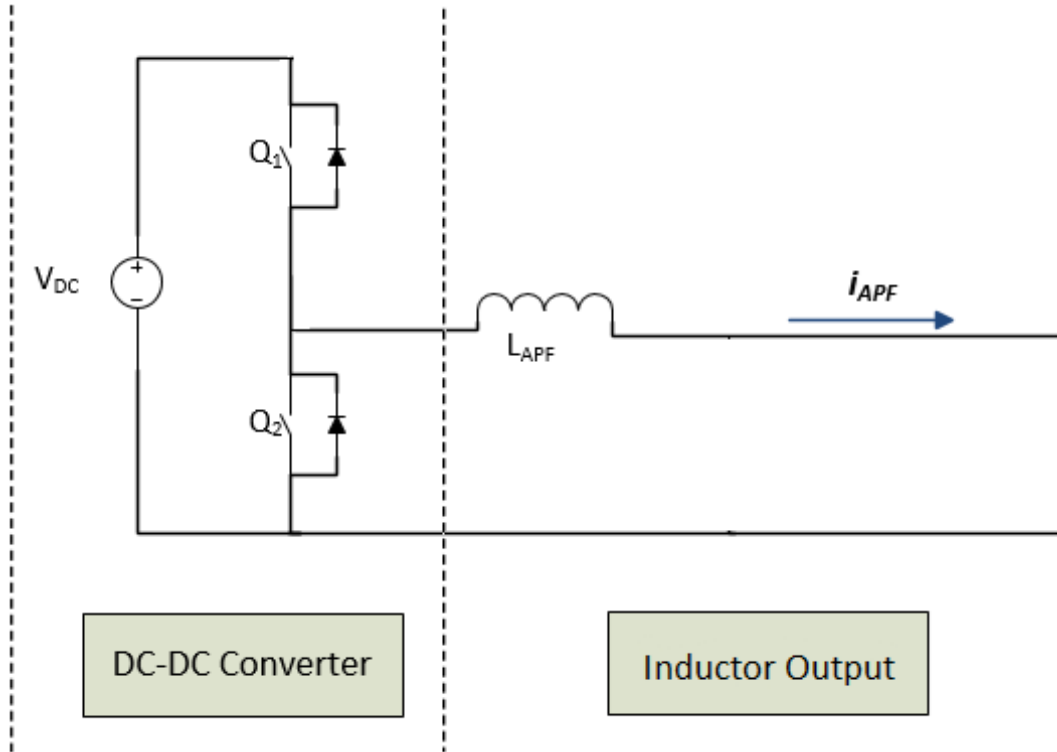


Figure 5.2: Modified Shunt Active Power Filter Circuit

Switch  $Q_1$  is responsible for regulating the energy storage of the inductor while switch  $Q_2$  maintains a constant output voltage so as to obtain a constant output current. Using the right switching signal, the current, when channeled through the inductor, will contain the required harmonic compensation. The voltage source is modeled to continuously carry a voltage that is equivalent to the fuel cell voltage. The inductor output is connected in parallel to the fuel cell source, thus, completing the transformerless APF configuration.

## 5.3 Generation of Switching Signal

The selection of an appropriate switching technique, that will switch the APF converter to produce an output current that is equal in magnitude and phase to the compensating current, is the next stage for realization of the modified shunt APF. With the correct control methodology, the APF converter can generate the compensating current and successfully negate the unwanted harmonics from the system. Of the many different processes, used for generating converter switching signals, the hysteresis current control is the least complex controller [94]. It has quick response, internal current limiting capacity and stability.

The basic principle for hysteresis current control is to control the switches of the converter such that it can force the current to ramp up or ramp down with respect to the reference current [94]. For the modified shunt APF, the reference signal is the extracted harmonic signal. The hysteresis current controller compares the extracted harmonic signal with the output of the APF converter to generate the reference signal.

If  $i_r$  is the reference signal and  $i_{APF}$  is the output current of the APF, then the error signal  $e_{hcc}$  is given by:

$$e_{hcc} = i_r - i_{APF} \quad (5.1)$$

The upper and lower limits are set based on the DC voltage that is supplied to the APF converter. If the error signal attains the upper limit of the hysteresis band, then the switching sequence is modified so as to lower the APF output current. Similarly, when the error signal is near the lower band the APF converter is switched to increase the output current. For the proposed

modified shunt APF, the hysteresis band is set between the minimum and maximum limits of the extracted harmonic current. Figure 5.4 shows a typical hysteresis band.

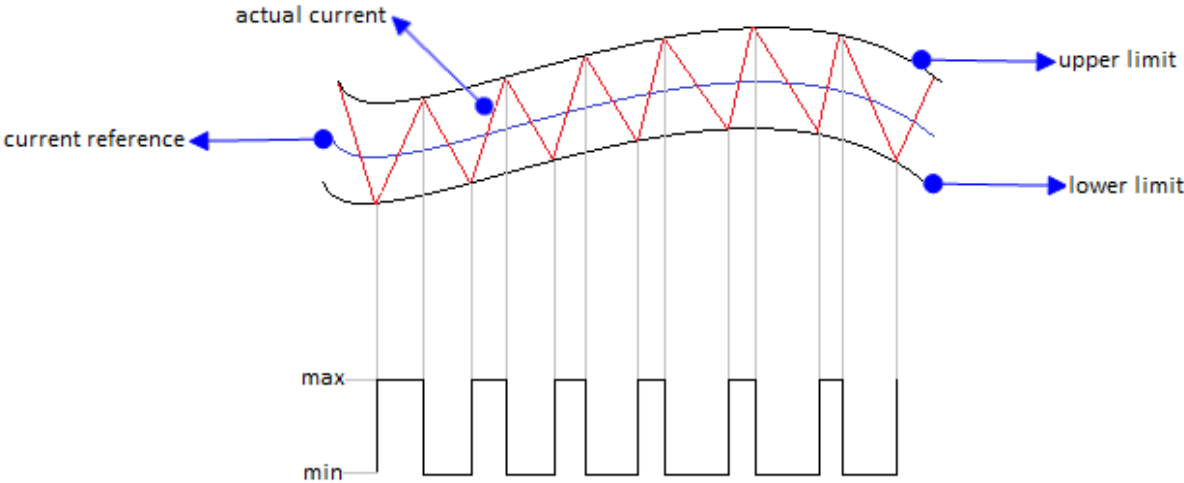


Figure 5.3: Principle of Hysteresis Current Control

Figure 5.4 shows the realization of the hysteresis current controller for the modified shunt APF.

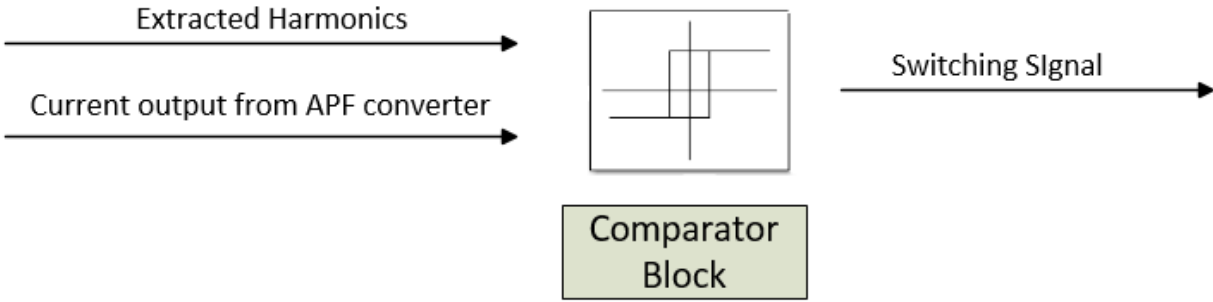


Figure 5.4: Structure of Hysteresis Current Controller

A comparator block has been used to set the hysteresis limit. The comparator block compares the output from the harmonic extractor and APF converter and decides on the switching

signal, needed to force the converter to follow the extracted harmonic waveform, as closely as possible. This ensures that the converter output and extracted harmonic waveforms are the same in magnitude and phase.

## 5.4 Harmonic Extraction

In order to compensate the harmonics present in the fuel cell current, the modified shunt APF generates a current waveform, which contains harmonics of the same magnitude and phase as the one that needs to be negated. Since the compensating current is generated by means of a converter, the switching signal responsible for operating the converter is determined from the system harmonics. Hence, the process of harmonic extraction is essential for the operation of the modified shunt APF.

Most harmonic extraction methodologies are designed for three phase systems, of which the PQ [95] and dq [96] frame harmonic extractions are commonly used. Since the fuel cell current is a DC component, the aforementioned harmonic extraction methods will not be suitable. A proposed modified PQ reference harmonic extraction, for single phase systems, does not adapt to DC signals [97]. In order to extract the harmonics from the DC signal, a method that can use DC signals as reference has to be considered. Wagh et al [98] have used a DC estimation methodology to extract DC signals from power transformer inrush currents. The advantage of this method is that the signal is decomposed into two components, DC and other harmonic components, which makes the extraction process easier. Jou et al. [99] used a similar method to implement an active power filter for removing load harmonics in a single-phase AC power system. The method, referred to as

“sine wave multiplication,” uses a sine wave reference signal to aid in extracting the sinusoidal component. This method has been modified for DC signals and is used to extract the harmonics from the fuel cell current.

The fuel cell current comprises both DC and other harmonic components, with the second order harmonic of single-phase inverter output frequency, being the dominant harmonic component. Consequently, the fuel cell current can be expressed mathematically as:

$$i_1 = I_1 + I_{12} \sin(2\omega t + \theta_2) + \sum_{n=2}^{\infty} I_{12n} \sin(2n\omega t + \theta_{2n}) \quad (5.2)$$

where,  $I_1$  is the DC current and is already known,  $I_{12}$  is the second harmonic component and the remaining terms represent the summation of even harmonics that may have consequently propagated to the fuel cell.

Ideally, the fundamental signal would be used as the reference signal, but since the fuel cell current is a DC signal, the harmonic signal that has to be extracted is selected as the reference signal as given by (5.3).

$$i_r = \sin(2\omega t) \quad (5.3)$$

From the analysis carried out in the previous chapter, the ripples are caused by the second harmonic component, hence, the reference signal is selected at twice the frequency at which the inverter is operated.

In order to identify the magnitude of the harmonic signal, Fourier transform is carried out on the product of the reference signal and the fuel cell current. This is given by:

$$I_x = \frac{1}{t} \int_0^t i_1 i_r dt \quad (5.4)$$

Since the magnitude of the harmonic component is known, the harmonic signal is thus obtained by multiplying the magnitude with the reference signal.

$$i_s = I_x i_r \tag{5.5}$$

The harmonic analysis in the previous chapter (Chapter 4) revealed that other than the DC component the second harmonic is the most prominent harmonic order. Hence, in order to increase the fuel cell’s power rating, it will be adequate to remove only the second harmonic from the fuel cell current.

The entire process of harmonic extraction is shown in Figure 5.5.

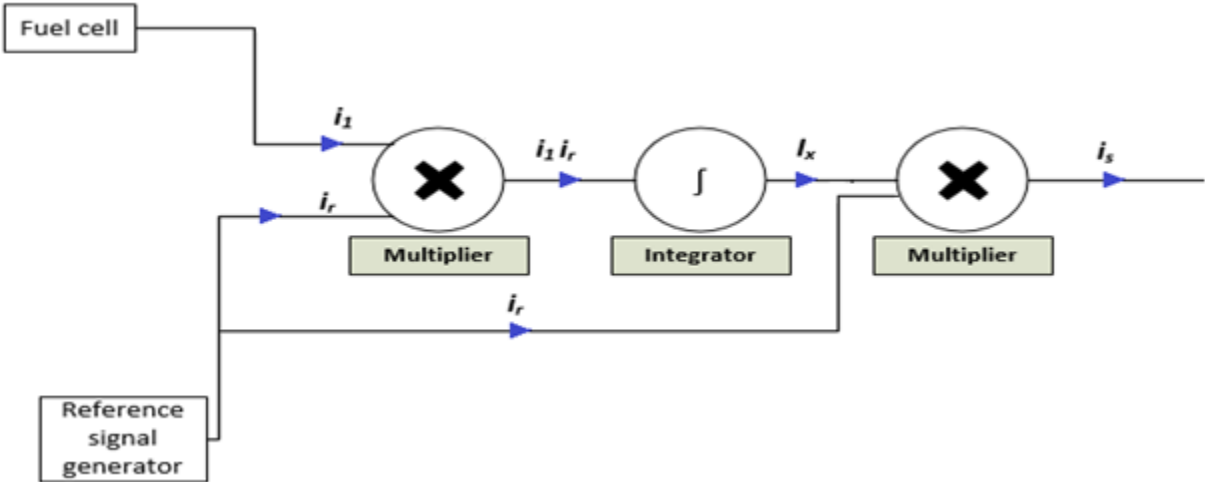


Figure 5.5: Algorithm for Harmonic Extraction

The extracted harmonic waveform, for a nonlinear load of 160 W, is shown in Figure 5.6.

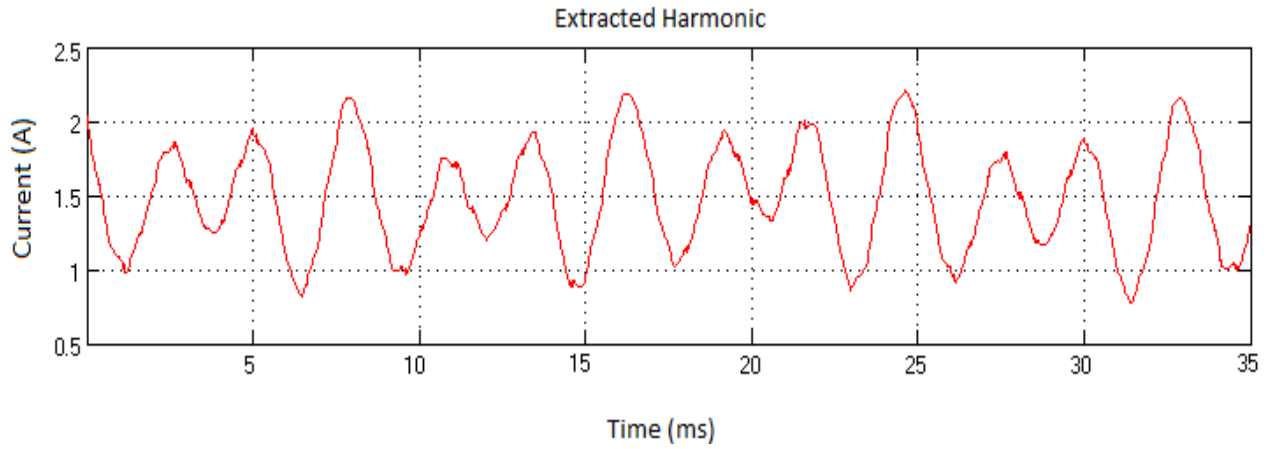


Figure 5.6: Extracted Harmonic Waveform from Fuel Cell Current under Nonlinear load of 160 W, 60 Hz

## 5.5 Implementation of the Modified Shunt APF

The APF parameters are given in Table 5.1. Figure 5.7 shows the implemented APF circuit.

Table 5.1: Modified Shunt APF Parameters

<i>Parameter</i>	<i>Value</i>
<i>Switch</i>	<i>IGBT</i>
<i>Hysteresis Limit</i>	<i>Upper Band = 2</i>
	<i>Lower Band = 1</i>
<i>V<sub>DC</sub></i>	<i>46.5 V</i>
<i>L<sub>APF</sub></i>	<i>2.5mH</i>

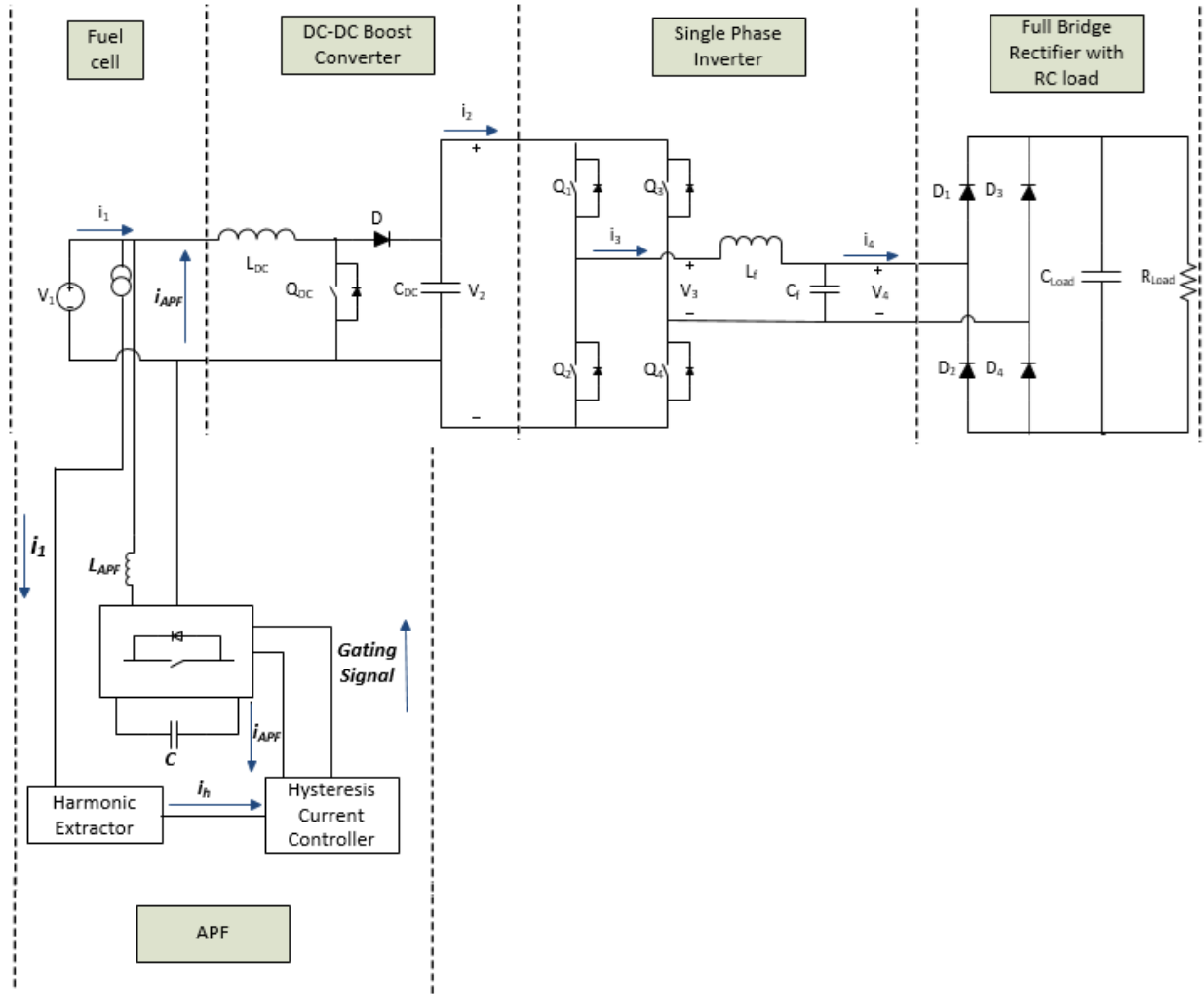


Figure 5.7: Fuel Cell System with Modified Shunt Active Filter

The performance of the complete fuel cell system with the APF is evaluated for three different load magnitude conditions. Figure 5.8 compares the modified shunt APF output current with the extracted harmonic, under nonlinear load of 160 W.

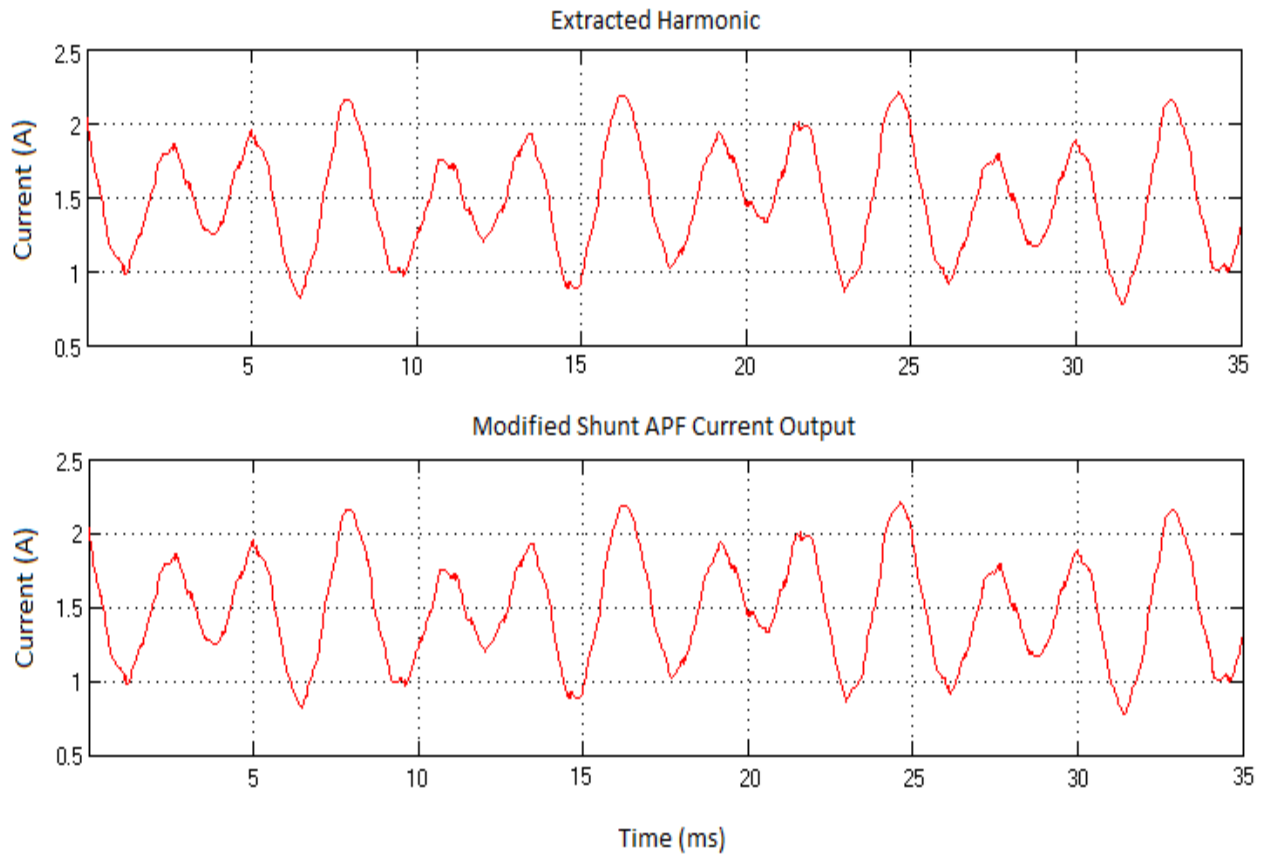


Figure 5.8: Extracted Fuel Cell Harmonic Current and Modified Shunt APF Current Output under nonlinear load of 160 Watts, 60 Hz

In order to provide effective compensation, it is essential that the extracted harmonic signal and the APF current output be equal in magnitude and phase. The modified shunt APF current and the extracted harmonics, as shown in Figure 5.8, have the same magnitude and phase. This should be effective in compensating the harmonics from the fuel cell source.

The modified shunt APF is now evaluated against three nonlinear loads. The APF parameters, as given in Table 5.1, are maintained constant for all the three loads.

### **5.5.1 Load Value of 160 Watts**

Figures 5.9 (a) & (b) show the system waveforms after APF implementation.

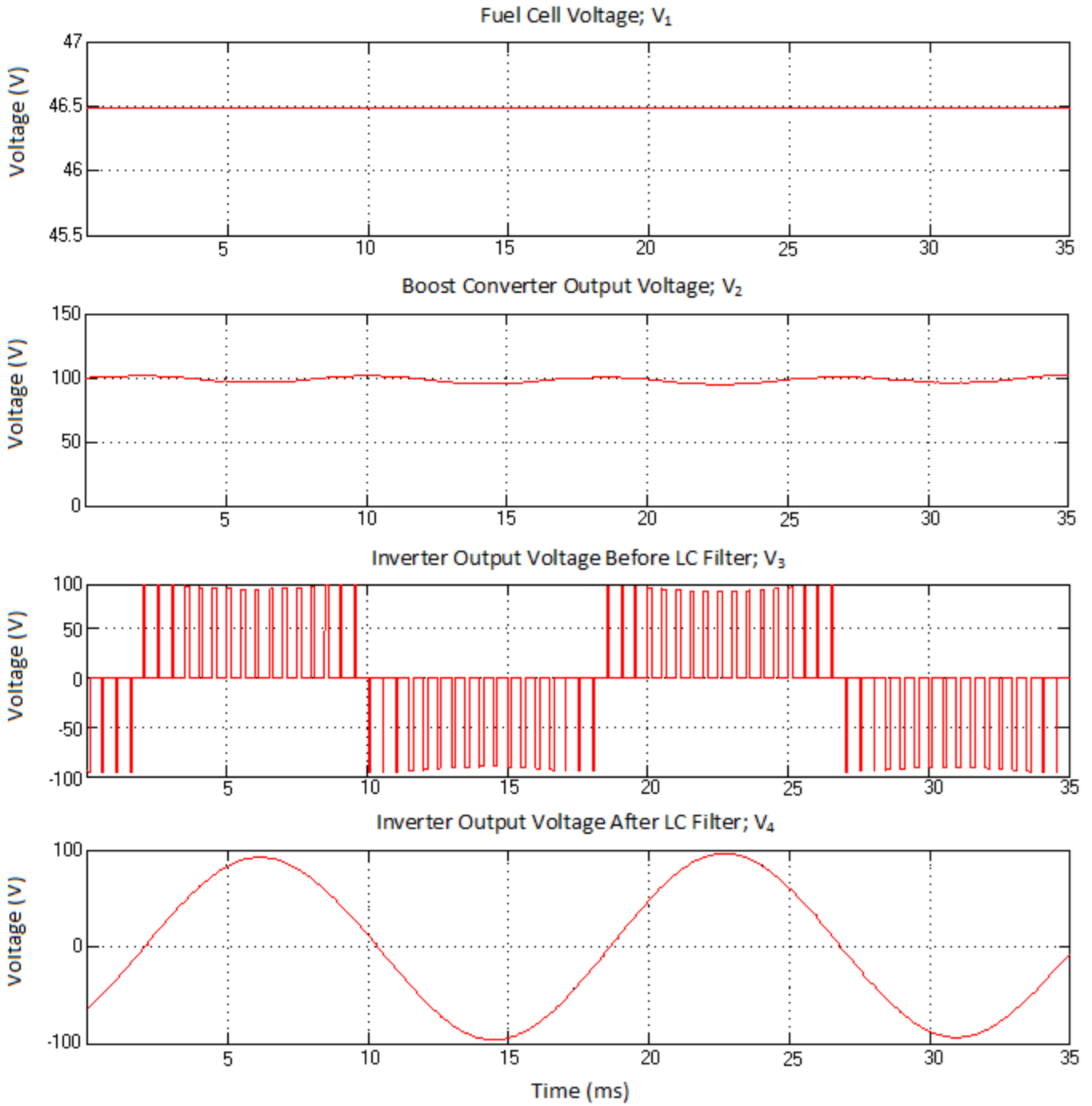


Figure 5.9 (a): Voltage Waveforms under Nonlinear Load of 160 W after APF Implementation

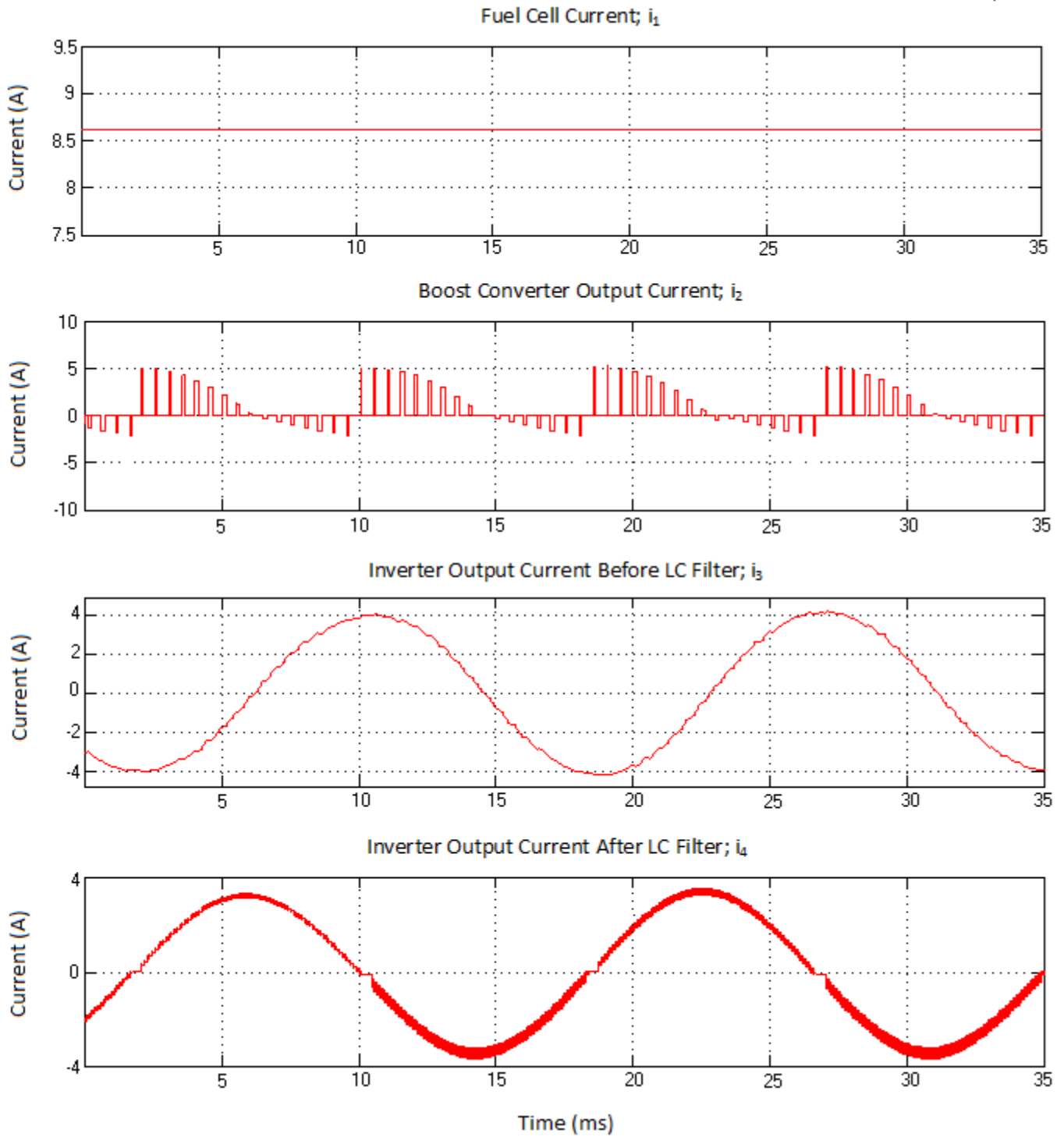
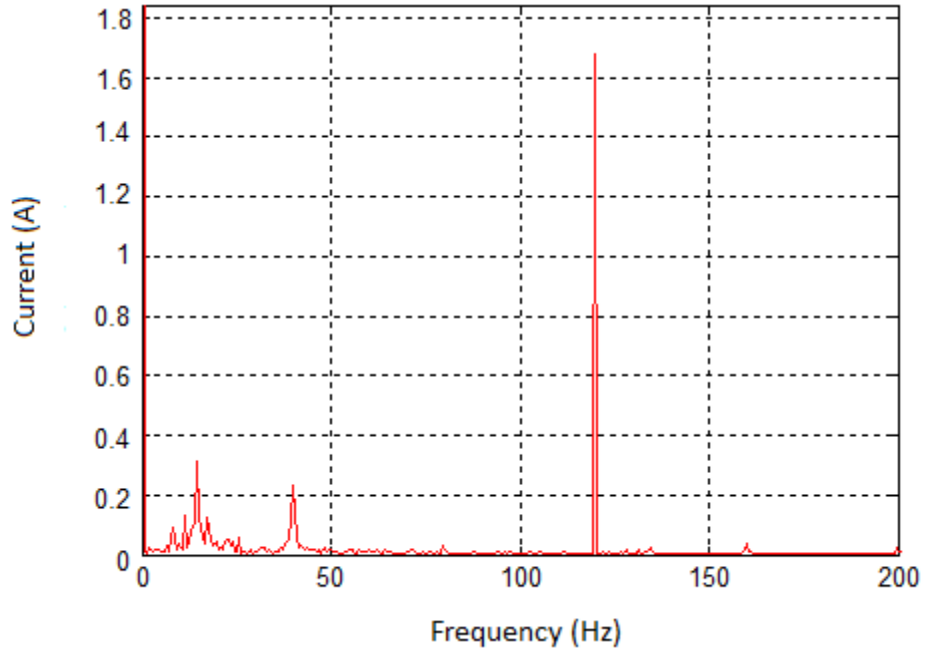


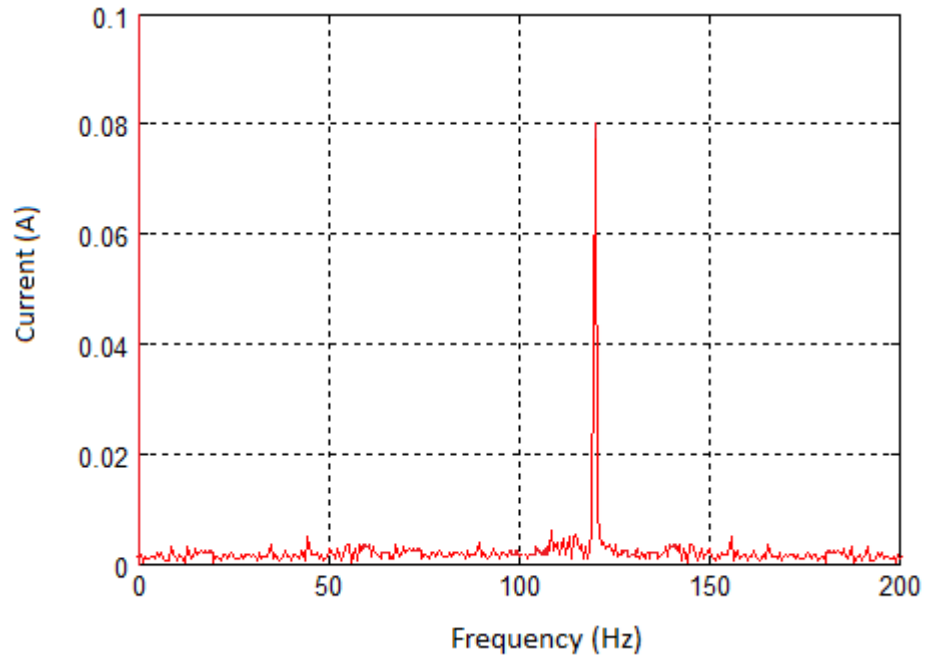
Figure 5.9 (b): Current Waveforms under Nonlinear Load of 160 W after APF

Implementation

In chapter 4, steady state ripple analysis at a load power of 160 W exhibited a fuel cell ripple of constant magnitude with an average fuel cell current of 7.5 A. After APF implementation, the average fuel cell current has increased to 8.59 A, while the voltage has stabilised at 46.4 V. The magnitude of the second harmonic is identified using harmonic analysis, as shown in Figure 5.10, for before and after APF implementation.



(a)



(b)

Figure 5.10 Harmonic Analysis of Fuel Cell Current under Nonlinear Load of 160 W (a) Before APF implementation (b) After APF Implementation

It is observed from Figure 5.10 that the second harmonic component is only 0.93% of the DC component as compared to 20.18% of DC without filter implementation.

### **5.5.2 Load Value of 240 Watts**

The system waveforms, after APF implementation, are shown in Figures 5.11 (a) and (b).

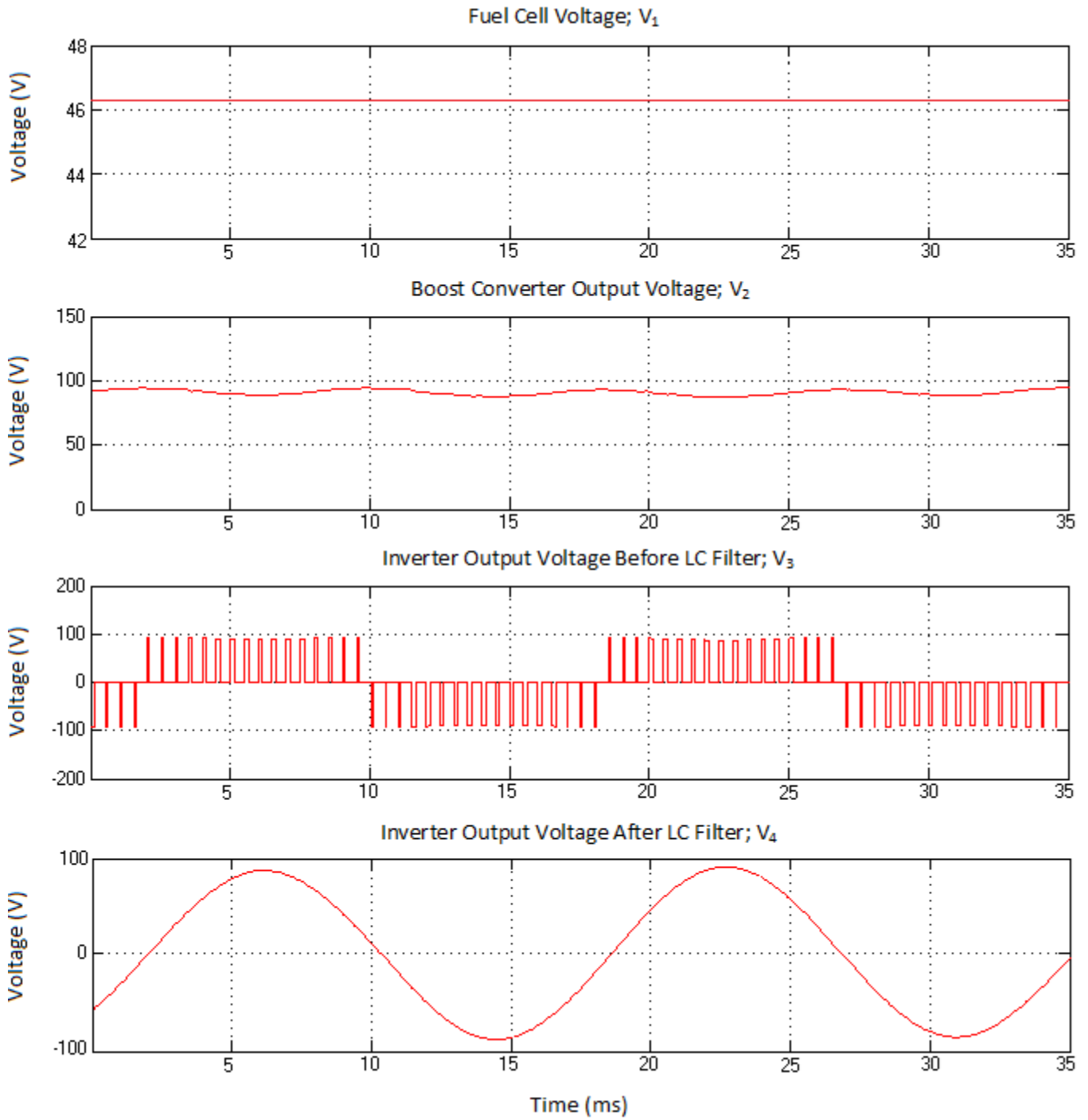


Figure 5.11 (a): Voltage Waveforms under Nonlinear Load of 240 W after APF Implementation

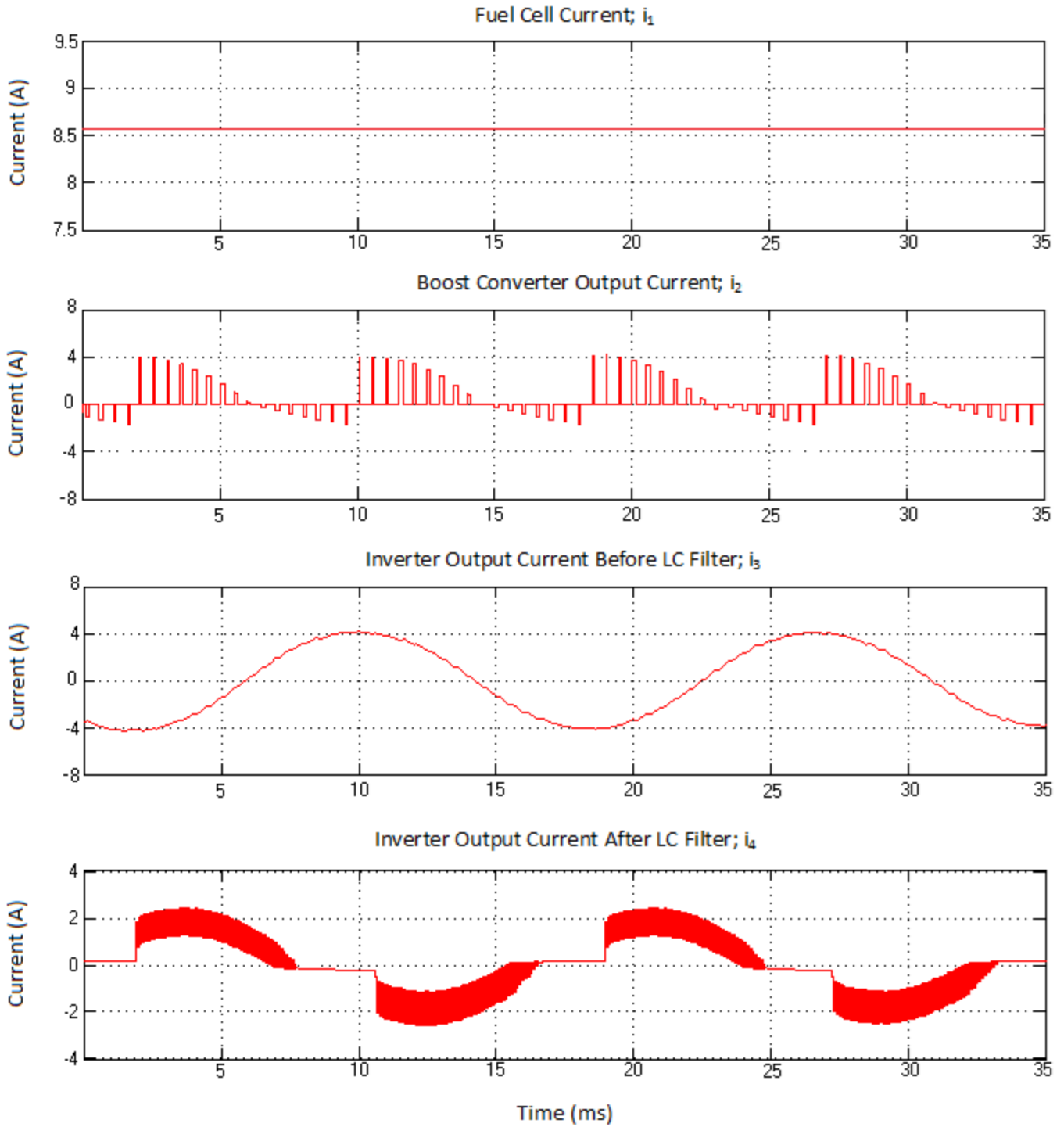
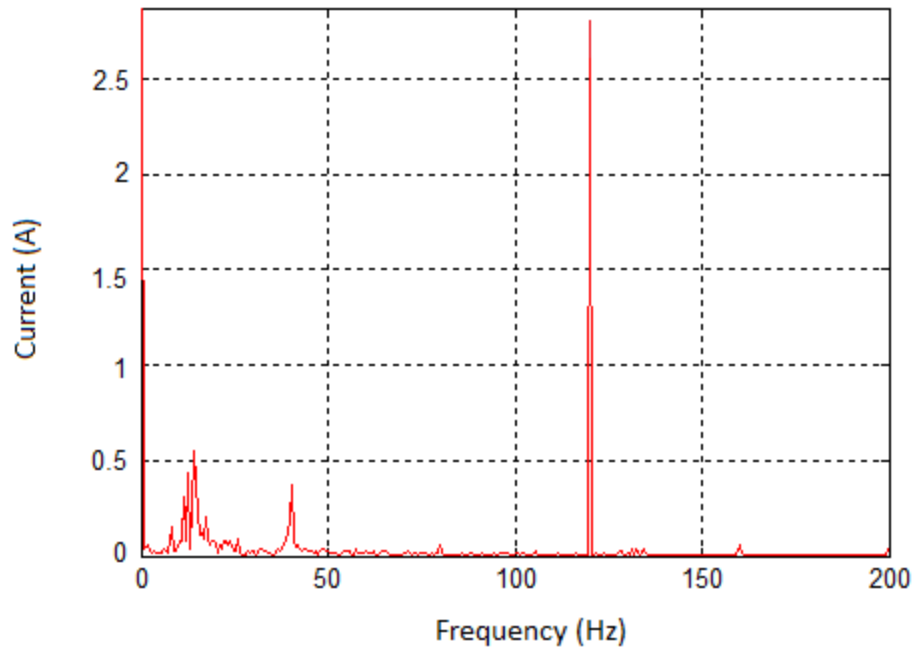
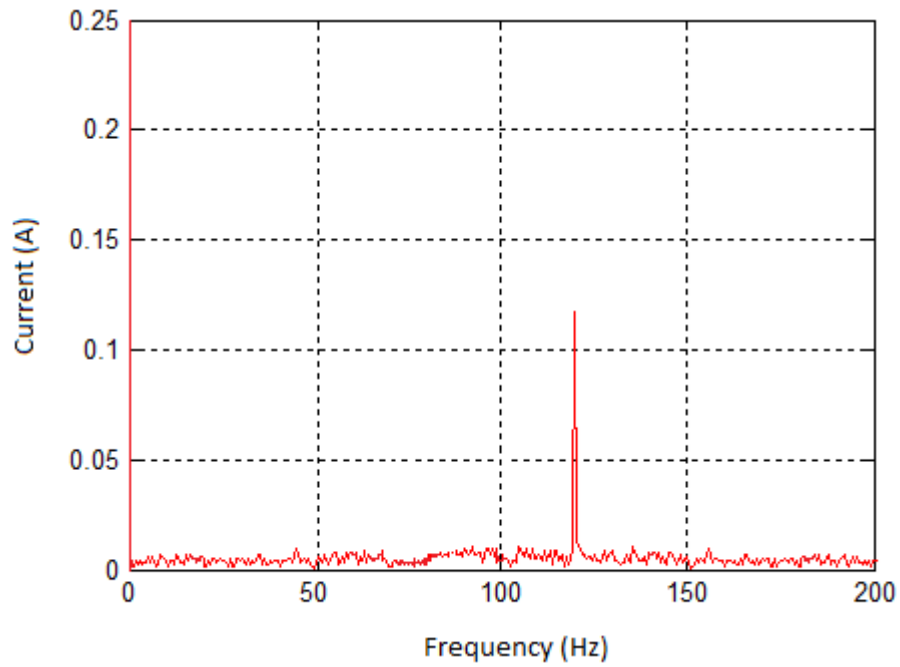


Figure 5.11 (b): Current Waveforms under Nonlinear Load of 240 W after APF Implementation

From Figure 5.11 (a) and (b) it is clear that though the nonlinear load still produces DC link harmonics, these harmonics are no longer visible on the fuel cell voltage and current waveforms. The fuel cell voltage is a constant DC signal of 46.5 V, while the current is measured at 8.57 A. Although, both the voltage and current waveforms appear to be DC signals, it is necessary to measure the second harmonic to demonstrate the effectiveness of the APF. Figure 5.12 shows the harmonic analysis of the fuel cell before and after the APF implementation.



(a)



(b)

Figure 5.12: Harmonic Analysis of Fuel Cell Current under Nonlinear Load of 240 W (a) Before APF implementation (b) After APF implementation

After APF implementation, the second harmonic is reduced to only 1.39% of the DC fuel cell current. This is a great improvement as compared to the second harmonic content of the fuel cell current before APF implementation.

### **5.5.3 Load Value of 400 Watts**

Finally, the system waveforms under a nonlinear load of 400 W, after APF implementation are given in Figures 5.13 (a) and (b).

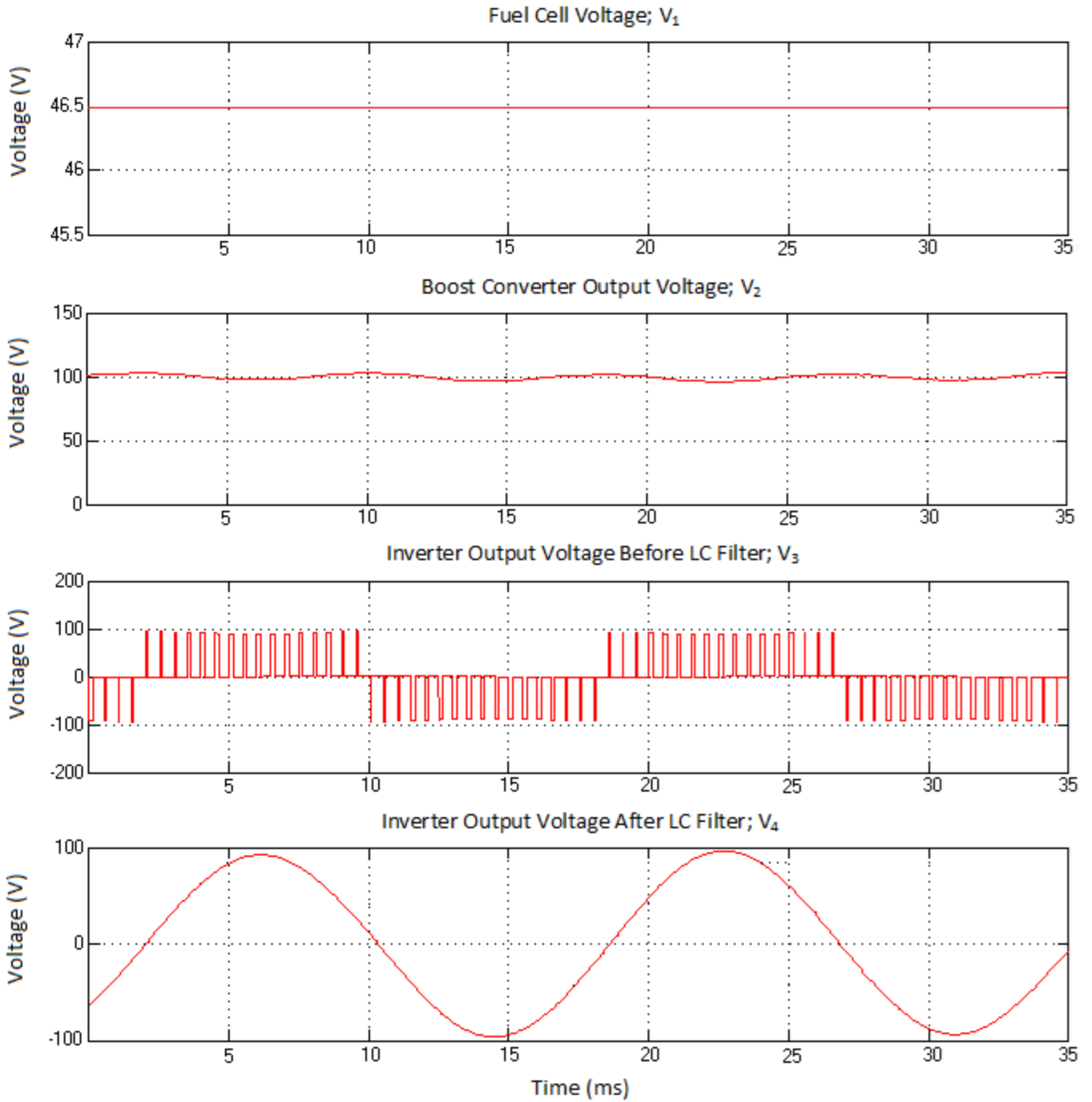


Figure 5.13 (a): Voltage Waveforms under Nonlinear Load of 400 W after APF Implementation

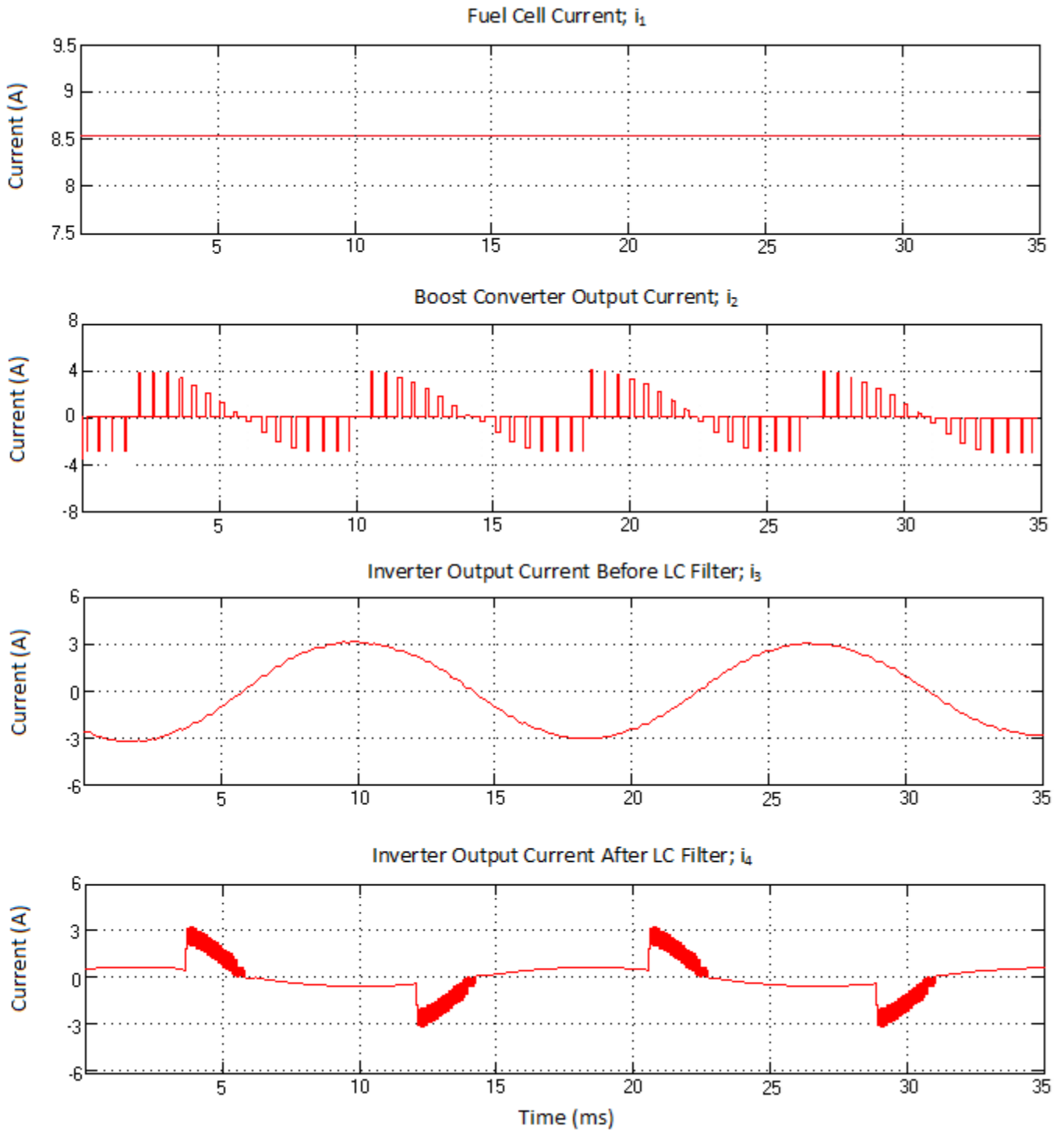
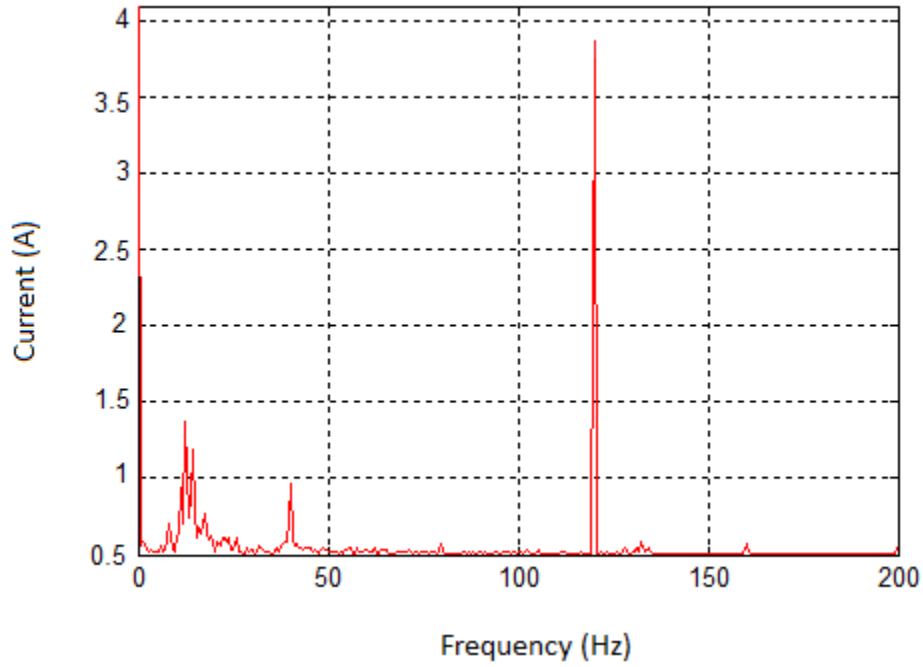


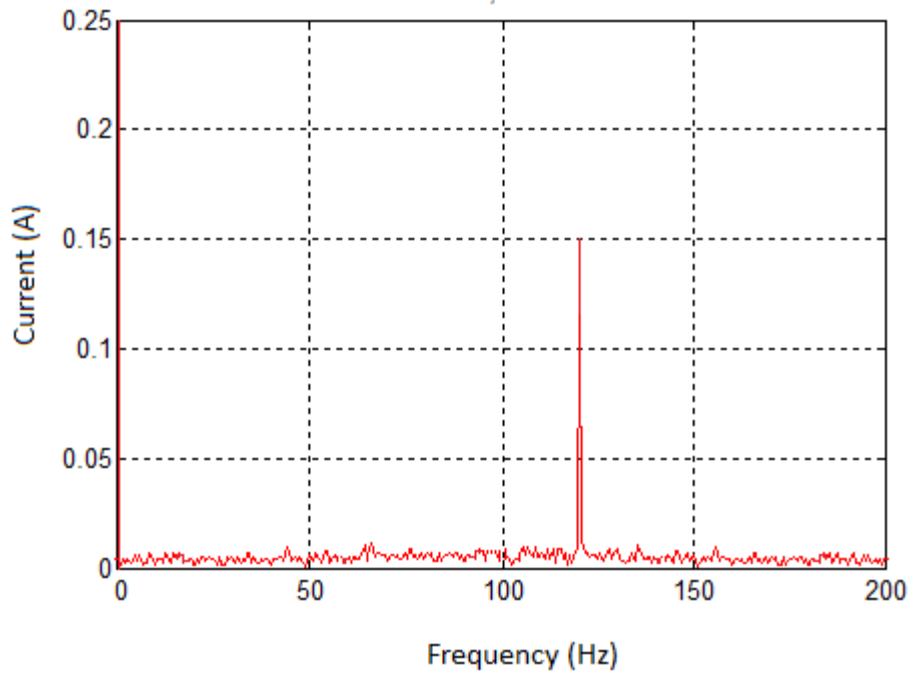
Figure 5.13 (b): Current Waveforms under Nonlinear Load of 400 W after APF

Implementation

Previously, the highest magnitude of fuel cell current ripples were observed under nonlinear load of 400 W. The use of an APF has reduced the presence of ripples on both fuel cell voltage and current waveforms. The fuel cell voltage is now 46.5 V with fuel cell current of 8.55 A. The actual harmonic content is determined using harmonic analysis as shown in Figure 5.14.



(a)



(b)

Figure 5.14: Harmonic Analysis of Fuel Cell Current under Nonlinear Load of 400 (a) Before APF Implementation (b) After APF Implementation

The harmonic analysis shows that the second harmonic has now reduced from 44.37% to 1.74% and the other harmonic components are smaller than 0.5 mA.

The second harmonic content for each load condition before and after the APF has been implemented is summarized in Table 5.2.

*Table 5.2: Harmonic Comparison Before and After APF Implementation for Three Nonlinear Load Conditions*

<i>Load Value (Watts)</i>	<i>Harmonic Order</i>	<b>Before APF</b>			<b>After APF</b>		
		<i>Mag. (A)</i>	<i>% DC</i>	<i>Fuel Cell Power (Watts)</i>	<i>Mag. (A)</i>	<i>% DC</i>	<i>Fuel Cell Power (Watts)</i>
160	DC	8.5	100	338.78	8.55	100	399.73
	2 <sup>nd</sup>	1.74	20.18		0.08	0.93	
240	DC	8.46	100	335.22	8.5	100	398.56
	2 <sup>nd</sup>	2.86	33.27		0.12	1.39	
400	DC	8.4	100	310.21	8.48	100	398.01
	2 <sup>nd</sup>	3.82	44.37		0.15	1.74	

The results for the three load conditions presented above show that the shunt active power filter successfully reduces the propagating harmonics and thus increases the amount of power that can be extracted from the fuel cell. By removing the propagating ripple, the magnitude of the fuel cell current becomes constant. The modified shunt APF minimizes the harmonic content to less than 1.2% of the DC value. Overall, the APF has been successful in reducing 98.26% of the ripple content from the fuel cell current.

The unique DC design makes the APF usable for most renewable energy sources that exhibit the phenomenon of ripple propagation, such as PV panels [74]. The transformerless APF makes implementation easy and less complicated. Hence, it can be used for small fuel cell systems.

In order to use the transformerless design for medium or large fuel cell systems, the passive filter design will have to be modified not only in terms of magnitude but also in terms of the passive components that can be included at the output of the modified shunt APF.

## **5.6 Summary**

The process of removing harmonic disturbances from the fuel cell can be achieved using either passive or active power filters. Although passive power filters are easy to implement, their uses are limited due to the design limitations that do not account for adaptable ripple filtering. Unlike the passive filter, active power filters approach the problem of ripple mitigation solely from the perspective of ripple compensation. This feature makes the active power filter ideal for fuel cell systems, where the propagation of ripples is of primary concern. Weighing the pros and cons of various active filter topologies, a transformerless modified shunt active filter, suitable for DC use, has been proposed and implemented for the fuel cell system. The fuel cell system with the modified shunt APF has been implemented for three steady state load conditions and evaluated against the results obtained in the previous chapter. The implemented filter successfully removes over 98.26% of ripple content from the fuel cell current.

# Chapter 6

## Conclusion

This thesis has discussed the features of a solid oxide fuel cell and has elaborated the process by which such a fuel cell can be modeled to predict both DC and AC behavior. Through the modeling process it is revealed that fuel cells, unlike other DC sources, reacts nonlinearly to AC loads which are capable of producing DC source harmonics. The nonlinearity is a function of the frequency at which the system harmonics are propagated to the fuel cell source and the load current. At low ripple frequencies, a marked phase difference is observed between the fuel cell voltage and fuel cell current waveforms. This phase difference causes the fuel cell voltage to lag with respect to the current. At high ripple frequencies the phase difference decreases and the fuel cell polarization curve starts to resemble the DC polarization curve.

The nature of ripple propagation is further analyzed, in this thesis, using a fuel cell based power system. The fuel cell power system includes a DC-DC boost converter, a single-phase inverter and a rectifier with an RC load. The fuel cell voltage and current waveforms are observed under varying load magnitude and frequency conditions. The analysis reveals that with increasing

load magnitude, the magnitude of the propagating ripples also increases. However, with increasing switching frequency the DC source harmonics are less and hence, the magnitude of propagating ripples also decreases. Harmonic analysis was used to determine the magnitude of each harmonic frequency, with emphasis on lower order frequencies.

The final section of this thesis introduced the concept of Active Power Filters (APF). Various topologies of APFs were discussed along with their relative usage. In order to implement an APF for fuel cell applications, a modified shunt APF was proposed, which included an approach to extract harmonics from a DC signal as opposed to harmonic extraction from sinusoidal signals. A simple hysteresis current controller was implemented to operate the APF. The APF was evaluated for three load magnitudes, under steady state condition. The simulation results demonstrated that the APF was successful in reducing 98.26% of ripples present in the fuel cell current.

## **6.1 Original Contribution**

The research conducted in this thesis is unique in the sense that it investigates the use of an active power filter to reduce the propagated ripple currents in a fuel cell output current. The main contributions of this thesis can be summarized as follows:

1. Fuel cell parameters and equations have been properly detailed so that similar fuel cell models can be developed for future research. Although the fuel cell model uses previously ascertained equations, the inclusion of double-layer capacitance can be considered an extension of the DC model as proposed by Santarelli et al. [51] and is unique because of its modeling details.

2. The extensive ripple analysis provides a deeper insight into the phenomenon of ripple propagation in fuel cells. Although, research has been conducted on the effects of ripple propagation, it has not been conducted for both magnitude and inverter frequency variations. The frequency variations validate the polarization curve which shows that at higher inverter frequencies, lesser ripples will propagate to the fuel cell source.
3. The most important aspect of this thesis, is the implementation of an active power filter that can effectively reduce the presence of propagating ripples from the fuel cell current. For small power systems, the use of large filter capacitance and multilevel topologies are not feasible, hence, the use of a single APF, for the purpose of maintaining ripple-free fuel cell current, is a more feasible solution. The control of the APF is modified to support the extraction of ripple currents from a DC system. Also by implementing the APF at the output of the fuel cell, it is possible to modify the other power stages, while ensuring stable power extraction from the fuel cell.

The work presented in this thesis provides a comprehensive analysis of ripple currents and their impact on the output power produced by the fuel cell in a small fuel cell power system. The improved power levels clearly indicate the advantages of using an APF for the sole purpose of removing ripples from fuel cell current. The approach provides a basis for the ripple current characterization of a medium or large fuel cell power system.

## **6.2 Future work**

In this work, a simple hysteresis current controller is used to demonstrate the feasibility of the APF implementation. However, the hysteresis current controller leaves a broad margin for

comparison, which decreases its effectiveness in adjusting to the expected output value. Since the frequency of the propagating harmonics remains constant, the hysteresis current controller was successful in operating the APF. For variable inverter frequencies, the hysteresis controller may prove to be ineffective. Hence, as part of future development, a more advanced control methodology can be considered.

The second aspect of improvement is the process of harmonic extraction. The harmonic extraction from the fuel cell current waveform is based on the assumption that frequency of operation of the single-phase inverter is known so that only the second harmonic current propagates to the fuel cell. For variable inverter frequencies the harmonic extraction method will be ineffective. Further research to address this issue is required. For example, a dynamically adaptable algorithm that can detect the inverter operating frequency and adjust the harmonic extraction procedure can be considered.

Finally, all the discussion in this thesis pertains to steady state conditions, where the load magnitude or frequency is manually varied. In a more practical scenario, the load varies randomly causing the ripple content to fluctuate. This transient behavior has not been studied in this thesis. A detailed examination of the dynamic operation of the fuel cell system, under dynamic load conditions would complete the full characterization of the fuel cell.

# References

- [1] G. C. Congress. Toyota pops the hood on the technology of the fuel cell mirai at SAE world congress. *April 29*pp. 2015. 2015.
- [2] G. Jones, "Ramea report," Nalcor Energy, St. John's; NL, 2010.
- [3] M. C. Williams, J. P. Strakey and W. A. Surdoval. U.S. department of energy's solid oxide fuel cells: Technical advances. *International Journal of Applied Ceramic Technology* 2(4), pp. 295-300. 2005.
- [4] R. P. O'Hayre, S. Cha, W. Colella and F. B. Prinz. *Fuel Cell Fundamentals* 2006.
- [5] D. Bloomfield, N. Hassett and J. Stedman. *Regenerative Fuel Cell* 1974.
- [6] M. Müller. Regenerative Fuel Cells. *Fuel Cell Science and Engineering: Materials, Processes, Systems and Technology* pp. 219-245. 2012.
- [7] V. S. Bagotsky. *Fuel Cells: Problems and Solutions* 201256.
- [8] T. Fuller and K. Gallagher. Phosphoric acid fuel cells. *Mater Fuel Cells* pp. 209-247. 2008.
- [9] E. Gülzow. Alkaline fuel cells. *Fuel Cells* 4(4), pp. 251-255. 2004.
- [10] A. L. Dicks. Molten carbonate fuel cells. *Current Opinion in Solid State and Materials Science* 8(5), pp. 379-383. 2004.
- [11] S. Singhal. Advances in solid oxide fuel cell technology. *Solid State Ionics* 135(1), pp. 305-313. 2000.
- [12] J. Amphlett, R. Baumert, R. Mann, B. Peppley, P. Roberge and A. Rodrigues. Parametric modelling of the performance of a 5-kW proton-exchange membrane fuel cell stack. *J. Power Sources* 49(1), pp. 349-356. 1994.

- [13] J. C. Amphlett, R. Baumert, R. F. Mann, B. A. Peppley, P. R. Roberge and T. J. Harris. Performance modeling of the ballard mark IV solid polymer electrolyte fuel cell I. mechanistic model development. *J. Electrochem. Soc.* 142(1), pp. 1-8. 1995.
- [14] R. Ferrero, M. Marracci, M. Prioli and B. Tellini. Simplified model for evaluating ripple effects on commercial PEM fuel cell. *Int J Hydrogen Energy* 37(18), pp. 13462-13469. 2012.
- [15] P. R. Pathapati, X. Xue and J. Tang. A new dynamic model for predicting transient phenomena in a PEM fuel cell system. *Renewable Energy* 30(1), pp. 1-22. 2005.
- [16] L. Zhu, L. Zhang and A. V. Virkar. A parametric model for solid oxide fuel cells based on measurements made on cell materials and components. *J. Power Sources* 291pp. 138-155. 2015.
- [17] W. Choi, P. Enjeti, J. W. Howze and G. Joung. An experimental evaluation of the effects of ripple current generated by the power conditioning stage on a proton exchange membrane fuel cell stack. *Journal of Materials Engineering and Performance* 13(3), pp. 257-264. 2004.
- [18] W. Choi, J. W. Howze and P. Enjeti. Development of an equivalent circuit model of a fuel cell to evaluate the effects of inverter ripple current. *J. Power Sources* 158(2), pp. 1324-1332. 2006.
- [19] D. Cheddie and N. Munroe. Review and comparison of approaches to proton exchange membrane fuel cell modeling. *J. Power Sources* 147(1-2), pp. 72-84. 2005.
- [20] (2015.02.24). *Development of Next-Generation Solid Oxide Fuel Cell Stack for Residential Fuel Cell Systems in Existing Apartments*. Available: <http://www.ecobyfco.com/newsroom/174/?la=en>.
- [21] (2016.01.26). *Fuel Cells x Combined Heat and Power*. Available: <http://enefield.eu/category/field-trials/technology/>.
- [22] Q. L. Liu, K. A. Khor and S. H. Chan. High-performance low-temperature solid oxide fuel cell with novel BSCF cathode. *J. Power Sources* 161(1), pp. 123-128. 2006.
- [23] Y. Leng, S. H. Chan and K. A. Khor. Development of YDB/GDC composite electrolyte for low-temperature solid oxide fuel cells. Presented at Proceedings-Electrochemical Society. 2005.
- [24] H. Yu, F. Zhao, A. V. Virkar and K. Fung. Electrochemical characterization and performance evaluation of intermediate temperature solid oxide fuel cell with  $\text{La}_{0.75}\text{Sr}_{0.25}\text{CuO}_{2.5-\delta}$  cathode. *J. Power Sources* 152, pp. 22-26. 2005.
- [25] M. E. Schenck, J. Lai and K. Stanton. Fuel cell and power conditioning system interactions. Presented at Applied Power Electronics Conference and Exposition, 2005. APEC 2005. Twentieth Annual IEEE. 2005.

- [26] K. Acharya, S. Mazumder, R. Burra, R. Williams and C. Haynes. System-interaction analyses of solid-oxide fuel cell (SOFC) power-conditioning system. Presented at Industry Applications Conference, 2003. 38th IAS Annual Meeting. Conference Record of the. 2003.
- [27] H. Chiu and L. Lin. A bidirectional DC-DC converter for fuel cell electric vehicle driving system. *Power Electronics, IEEE Transactions on* 21(4), pp. 950-958. 2006.
- [28] J. Kim, G. Choe, H. Kang and B. Lee. Effect of load modeling on low frequency current ripple in fuel cell generation systems. *Journal of Electrical Engineering & Technology* 5(2), pp. 307-318. 2010.
- [29] J. Kim, H. Kang, B. Lee and W. Lee. Analysis of low frequency current ripples of fuel cell systems based on a residential loads modeling. Presented at Electrical Machines and Systems, 2007. ICEMS. International Conference on. 2007, .
- [30] R. Ferrero, M. Marracci and B. Tellini. Single PEM fuel cell analysis for the evaluation of current ripple effects. *Instrumentation and Measurement, IEEE Transactions on* 62(5), pp. 1058-1064. 2013.
- [31] W. Kim, V. Duong, T. Nguyen and W. Choi. Analysis of the effects of inverter ripple current on a photovoltaic power system by using an AC impedance model of the solar cell. *Renewable Energy* 59pp. 150-157. 2013.
- [32] S. Moon, J. Lai, S. Park and C. Liu. Impact of SOFC fuel cell source impedance on low frequency AC ripple. Presented at Power Electronics Specialists Conference, 2006. PESC'06. 37th IEEE. 2006, .
- [33] R. S. Gemmen. Analysis for the effect of inverter ripple current on fuel cell operating condition. *Journal of Fluids Engineering* 125(3), pp. 576-585. 2003.
- [34] P. M. Biesheuvel, A. A. Franco and M. Z. Bazant. Diffuse charge effects in fuel cell membranes. *J. Electrochem. Soc.* 156(2), pp. B225-B233. 2009.
- [35] M. W. Fowler, R. F. Mann, J. C. Amphlett, B. A. Peppley and P. R. Roberge. Incorporation of voltage degradation into a generalised steady state electrochemical model for a PEM fuel cell. *J. Power Sources* 106(1-2), pp. 274-283. 2002.
- [36] A. Utz. *The Electrochemical Oxidation of H<sub>2</sub> and CO at Patterned Ni Anodes of SOFCs* 201120.
- [37] W. Zhu and S. Deevi. Development of interconnect materials for solid oxide fuel cells. *Materials Science and Engineering: A* 348(1), pp. 227-243. 2003.
- [38] J. Kim, G. Choe, H. Kang and B. Lee. Robust low frequency current ripple elimination algorithm for grid-connected fuel cell systems with power balancing technique. *Renewable Energy* 36(5), pp. 1392-1400. 2011.

- [39] A. E. Auld, K. M. Smedley, F. Mueller, J. Brouwer and G. S. Samuelsen. Load-following active power filter for a solid oxide fuel cell supported load. *J. Power Sources* 195(7), pp. 1905-1913. 2010.
- [40] S. K. Mazumder, R. K. Burra and K. Acharya. A ripple-mitigating and energy-efficient fuel cell power-conditioning system. *Power Electronics, IEEE Transactions on* 22(4), pp. 1437-1452. 2007.
- [41] J. -. Itoh and F. Hayashi. Ripple current reduction of a fuel cell for a single-phase isolated converter using a DC active filter with a center tap. *Power Electronics, IEEE Transactions on* 25(3), pp. 550-556. 2010.
- [42] J. Kwon, E. Kim, B. Kwon and K. Nam. High-efficiency fuel cell power conditioning system with input current ripple reduction. *Industrial Electronics, IEEE Transactions on* 56(3), pp. 826-834. 2009.
- [43] Changrong Liu and Jih-Sheng Lai. Low frequency current ripple reduction technique with active control in a fuel cell power system with inverter load. Presented at Power Electronics Specialists Conference, 2005. PESC '05. IEEE 36th. 2005
- [44] B. Han and J. Lee. Highly-efficient power-conditioning system for grid-tied fuel cell power generation.
- [45] T. M. Gür, M. Homel and A. V. Virkar. High performance solid oxide fuel cell operating on dry gasified coal. *J. Power Sources* 195(4), pp. 1085-1090. 2010.
- [46] M. Homel, T. M. Gür, J. H. Koh and A. V. Virkar. Carbon monoxide-fueled solid oxide fuel cell. *J. Power Sources* 195(19), pp. 6367-6372. 2010. .
- [47] J. M. Ogden, T. G. Kreutz and M. Steinbugler. *Fuels for Fuel Cell Vehicles: Vehicle Design and Infrastructure Issues* 1998.
- [48] A. Lazzaretto, A. Toffolo and F. Zanon. Parameter setting for a tubular SOFC simulation model. *Journal of Energy Resources Technology* 126(1), pp. 40-46. 2004.
- [49] P. Sharma and T. Bhatti. A review on electrochemical double-layer capacitors. *Energy Conversion and Management* 51(12), pp. 2901-2912. 2010.
- [50] M. Iwata, T. Hikosaka, M. Morita, T. Iwanari, K. Ito, K. Onda, Y. Esaki, Y. Sakaki and S. Nagata. Performance analysis of planar-type unit SOFC considering current and temperature distributions. *Solid State Ionics* 132(3), pp. 297-308. 2000.
- [51] M. Santarelli and P. Leone. *Advanced Methods of Solid Oxide Fuel Cell Modeling* 2011.
- [52] L. Zhang, L. Zhu and A. V. Virkar. Electronic conductivity measurement of yttria-stabilized zirconia solid electrolytes by a transient technique. *J. Power Sources* 302pp. 98-106. 2016

- [53] H. Lim and A. V. Virkar. Thermoelectric power of gd-doped CeO<sub>2</sub> (Gd<sub>0.1</sub>Ce<sub>0.9</sub>O<sub>2-δ</sub>) (GDC10): Measurements on porous samples. *J. Power Sources* 161(1), pp. 676-684. 2006
- [54] A. V. Virkar. Theoretical analysis of the role of interfaces in transport through oxygen ion and electron conducting membranes. *J. Power Sources* 147(1-2), pp. 8-31. 2005
- [55] A. V. Virkar. Transport of H<sub>2</sub>, O<sub>2</sub> and H<sub>2</sub>O through single-phase, two-phase and multi-phase mixed proton, oxygen ion, and electron hole conductors. *Solid State Ionics* 140(3-4), pp. 275-283. 2001.
- [56] W. Wang and A. V. Virkar. Ionic and electron-hole conduction in BaZr<sub>0.93</sub>Y<sub>0.07</sub>O<sub>3-δ</sub> by 4-probe dc measurements. *J. Power Sources* 142(1-2), pp. 1-9. 2005
- [57] F. Zhao and A. V. Virkar. Dependence of polarization in anode-supported solid oxide fuel cells on various cell parameters. *J. Power Sources* 141(1), pp. 79-95. 2005.
- [58] B. Conway and W. Pell. Double-layer and pseudocapacitance types of electrochemical capacitors and their applications to the development of hybrid devices. *J. Solid State Electrochem* 7(9), pp. 637-644. 2003.
- [59] X. Ge, C. Fu and S. H. Chan. Double layer capacitance of anode/solid-electrolyte interfaces. *Physical Chemistry Chemical Physics* 13(33), pp. 15134-15142. 2011.
- [60] J. Larminie, A. Dicks and M. S. McDonald. *Fuel Cell Systems Explained* 20032.
- [61] J. Kim, M. Jang, J. Choe, D. Kim, Y. Tak and B. Cho. An experimental analysis of the ripple current applied variable frequency characteristic in a polymer electrolyte membrane fuel cell. *Journal of Power Electronics* 11(1), pp. 82-89. 2011.
- [62] R. Bove and S. Ubertini. *Modeling Solid Oxide Fuel Cells: Methods, Procedures and Techniques* 2008
- [63] R. W. Erickson and D. Maksimovic. *Fundamentals of Power Electronics* 2007.
- [64] D. W. Hart. *Power Electronics* 2011.
- [65] H. Akagi. Trends in active power line conditioners. *Power Electronics, IEEE Transactions on* 9(3), pp. 263-268. 1994.
- [66] S. Banerjee and G. C. Verghese. *Nonlinear Phenomena in Power Electronics* 1999.
- [67] N. Mohan. *Power Electronics: A First Course* 2012.
- [68] N. Mohan and T. M. Undeland. *Power Electronics: Converters, Applications, and Design* 2007.

- [69] A. Cross, P. Evans and A. Forsyth. DC link current in PWM inverters with unbalanced and non-linear loads. *IEE Proceedings-Electric Power Applications* 146(6), pp. 620-626. 1999.
- [70] J. Irwin, M. P. Kazmierkowski, R. Krishnan and F. Blaabjerg. *Control in Power Electronics: Selected Problems* 2002.
- [71] C. R. Bush and B. Wang. A single-phase current source solar inverter with reduced-size DC link. Presented at Energy Conversion Congress and Exposition, 2009. ECCE 2009. IEEE. 2009.
- [72] S. Dasgupta, S. K. Sahoo and S. K. Panda. Single-phase inverter control techniques for interfacing renewable energy sources with microgrid—Part I: Parallel-connected inverter topology with active and reactive power flow control along with grid current shaping. *Power Electronics, IEEE Transactions on* 26(3), pp. 717-731. 2011.
- [73] A. Kirubakaran, S. Jain and R. Nema. A review on fuel cell technologies and power electronic interface. *Renewable and Sustainable Energy Reviews* 13(9), pp. 2430-2440. 2009.
- [74] S. Lee, T. An and H. Cha. Mitigation of low frequency ac ripple in single-phase photovoltaic power conditioning systems. *Journal of Power Electronics* 10(3), pp. 328-333. 2010.
- [75] M. H. Rashid. *Power Electronics Handbook: Devices, Circuits and Applications* 2010.
- [76] J. Das. Passive filters-potentialities and limitations. Presented at Pulp and Paper Industry Technical Conference, 2003. Conference Record of the 2003 Annual. 2003.
- [77] H. Kawahira, T. Nakamura, S. Nakazawa and M. Nomura. Active power filters. Presented at Proc. JIEE IPEC-Tokyo. 1983.
- [78] H. Akagi. New trends in active filters for power conditioning. *Industry Applications, IEEE Transactions on* 32(6), pp. 1312-1322. 1996.
- [79] G. A. Ramos, R. Costa-Castelló and J. M. Olm. "Shunt active power filter," in *Digital Repetitive Control Under Varying Frequency Conditions*, 2013.
- [80] H. Akagi. Modern active filters and traditional passive filters. *Bulletin of the Polish Academy of Sciences, Technical Sciences* 54(3), 2006.
- [81] H. Fujita and H. Akagi. The unified power quality conditioner: The integration of series and shunt-active filters. *Power Electronics, IEEE Transactions on* 13(2), pp. 315-322. 1998.
- [82] A. M. Al-Zamil and D. Torrey. A passive series, active shunt filter for high power applications. *Power Electronics, IEEE Transactions on* 16(1), pp. 101-109. 2001.
- [83] A. C. Chow and D. J. Perreault. Active EMI filters for automotive motor drives. Presented at Power Electronics in Transportation, 2002. 2002.

- [84] H. Fujita, T. Yamasaki and H. Akagi. A hybrid active filter for damping of harmonic resonance in industrial power systems. *Power Electronics, IEEE Transactions on* 15(2), pp. 215-222. 2000.
- [85] J. Häfner, M. Aredes and K. Heumann. A shunt active power filter applied to high voltage distribution lines. *Power Delivery, IEEE Transactions on* 12(1), pp. 266-272. 1997.
- [86] M. L. Heldwein, H. Ertl, J. Biela and J. W. Kolar. Implementation of a transformerless common-mode active filter for offline converter systems. *Industrial Electronics, IEEE Transactions on* 57(5), pp. 1772-1786. 2010.
- [87] R. Inzunza and H. Akagi. A 6.6-kV transformerless shunt hybrid active filter for installation on a power distribution system. *Power Electronics, IEEE Transactions on* 20(4), pp. 893-900. 2005.
- [88] H. Fujita and H. Akagi. A practical approach to harmonic compensation in power systems-series connection of passive and active filters. *Industry Applications, IEEE Transactions on* 27(6), pp. 1020-1025. 1991.
- [89] C. Lam and M. Wong. A capacitive-coupled transformerless active power filter with coupling current feedback control. Presented at Circuits and Systems, 2008. APCCAS 2008. IEEE Asia Pacific Conference on. 2008.
- [90] J. Wu, N. He and D. Xu. Design and application of transformerless shunt hybrid active power filter. *Proceedings-Chinese Society of Electrical Engineering* 28(12), pp. 88. 2008.
- [91] J. Zheng, C. Meng, P. Li and Y. Hong. The study of transformerless shunt hybrid active power filter compensation for unbalanced load. Presented at Power Electronics and Motion Control Conference (IPEMC), 2012 7th International. 2012.
- [92] H. Akagi. Active harmonic filters. *Proc IEEE* 93(12), pp. 2128-2141. 2005.
- [93] D. Glenting and D. Samuel. Digitally controlled active power filter for AESA radar. *Energy and Environment, Chalmers University of Technology, Gothenburg* 2013.
- [94] D. M. Brod and D. W. Novotny. Current control of VSI-PWM inverters. *Industry Applications, IEEE Transactions on* (3), pp. 562-570. 1985.
- [95] H. Kim and H. Akagi. The instantaneous power theory on the rotating pqr reference frames. Presented at Power Electronics and Drive Systems, 1999. PEDS'99. Proceedings of the IEEE 1999 International Conference on. 1999.
- [96] M. Saitou, N. Matsui and T. Shimizu. A control strategy of single-phase active filter using a novel dq transformation. Presented at Industry Applications Conference, 2003. 38th IAS Annual Meeting. Conference Record of the. 2003.

[97] A. Massoud, S. Finney and B. Williams. Review of harmonic current extraction techniques for an active power filter. 2004.

[98] S. R. Wagh, S. Kumar and V. Sreeram. Extraction of DC component and harmonic analysis for protection of power transformer. Presented at Industrial Electronics and Applications (ICIEA), 2013 8th IEEE Conference on. 2013.

[99] H. Jou, J. Wu and H. Chu. New single-phase active power filter. *IEE Proceedings-Electric Power Applications* 141(3), pp. 129-134. 1994.

# **Appendix A**

## **SOFC Model Parameters**

The fuel cell considered in this work consists of Ni–YSZ (Yttrium Stabilized Zirconium) electrodes and denser YSZ electrolyte. Table A.1 describes the YSZ parameters for both electrodes and electrolyte.

Table A.1: YSZ Parameters

<b>Parameter</b>	<b>Value</b>
<i>Area of electrode</i>	<i>1 cm<sup>2</sup></i>
<i>Area specific resistance (S/cm<sup>2</sup>)</i>	<i>0.25 @ 600 °C</i>
	<i>0.15 @ 700°C</i>
	<i>0.085 @ 800°C</i>
<i>Cell internal ionic resistance(S/cm<sup>2</sup>)</i>	<i>4 @ 600 °C</i>
	<i>4.5 @ 700 °C</i>
	<i>5.5 @ 800 °C</i>
<i>Electrode thickness</i>	<i>0.0008 cm</i>
<i>Fuel flow</i>	<i>2.333 * 10<sup>-6</sup> m<sup>3</sup>/s (140 ml/min)</i>
<i>Air flow</i>	<i>9.167x10<sup>-6</sup> m<sup>3</sup>/s (550 ml/min)</i>
<i>Pressure</i>	<i>0.1 Bar</i>

# Appendix B

## MATLAB Code for Single Cell SOFC at 800°C

```
%-----  
% name: SOFC modeling  
% created on: 02/01/2014  
%-----  
clear;  
clc;  
%-----State constants-----  
  
R = 8.3144621;  
Na = 6.0221413 *10^23;  
F = 96485;  
e = 1.6021761 *10^(-19);  
  
%-----input variables-----  
  
P = 1;  
P_atm = 1*10^5;  
T = (800+273.15);  
VH2 = 140;  
VH2_m = 0.000002333;  
VO2 = 550;  
VO2_m = 0.000009167;  
Electrolyte_thickness = 0.0008;  
ASR = 0.085;  
Area = 0.5;  
i = [0.6 0.7 0.8 0.9 1 1.1 1.2 1.3 1.4 1.5 1.6 1.7 1.8 1.9 2 2.1 2.2 2.3 2.4  
2.5 2.6 2.7 2.8 2.9 3];  
CIER = 5.5;
```

```

%-----calculation of maximum current density -----
for current = 1:length(i);
    curnt = i(current);

nH2 = (P_atm*VH2_m)/(R*T);
imax_f = (2*F*nH2)/Area;
imax_o = 2*imax_f*(VO2/VH2)*0.21;

%-----fuel utilisation factor -----

Uf = curnt/imax_f;
Uo = curnt/imax_o;

%-----area specific internal ionic resistance-----

Conductivity_actual = 390.95*exp((-87.806*10^3)/(R*T));
ASIR = (Electrolyte_thickness/Conductivity_actual)+ASR;

%-----partial pressures-----

pH2_anode_out = (1-Uf);
pH2O_anode_out = Uf;
pO2_cathode_out = 0.21*(1-Uo);

%-----maximum voltage (Nernst Voltage)-----

Factor_A =
log((pH2_anode_out*sqrt(pO2_cathode_out))/(pH2O_anode_out*sqrt(P)));
Factor_B = Factor_A*R*T;
Factor_C = Factor_B/(2*96485);
E_max = ((246*10^3)/(2*F))+((R*T*log(1.44*10^(-3)))/(2*F))+Factor_C;

%-----fuel cell voltage -----

Factor_D = imax_f*ASIR*Uf;
Factor_E = ASIR/CIER;
Factor_F = Factor_E*(1-Uf);
Factor_G = E_max - Factor_D;
Factor_H = Factor_F+1;
E_SOFC = Factor_G/Factor_H;
P = curnt*real(E_SOFC);
x2(current,1) = real(E_SOFC);
y(current,1) = P;
end
plot(i,x2);

```

# Appendix C

## Simulink Screenshots

### C.1 Simulink Simulation Parameters

The solver parameters, used in this research are given in Table C.1. The same solver parameters are maintained throughout this research. The actual passive parameters for each power stage has been mentioned in the previous Chapters.

*Table C.1: Simulink Solver Parameters*

<b>Parameter</b>	<b>Value</b>
<i>Simulation Type</i>	<i>Discrete</i>
<i>Solver</i>	<i>Tustin</i>
<i>Sample time (s)</i>	<i>50e-6</i>

# C.2 DC-DC Boost Converter

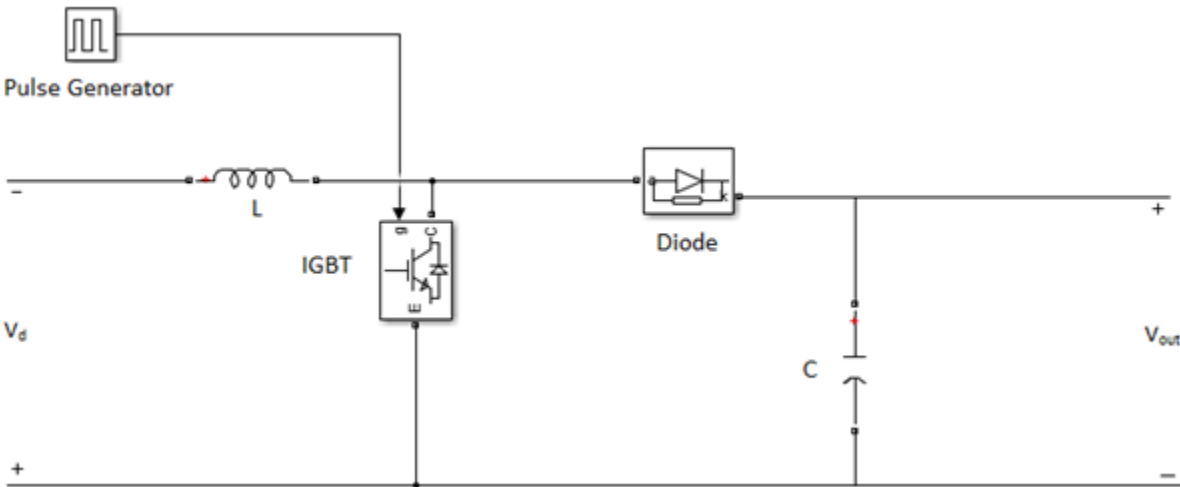


Figure C.1: Simulink Schematic of DC-DC Boost Converter

### C.3 Single-phase Full-bridge Inverter

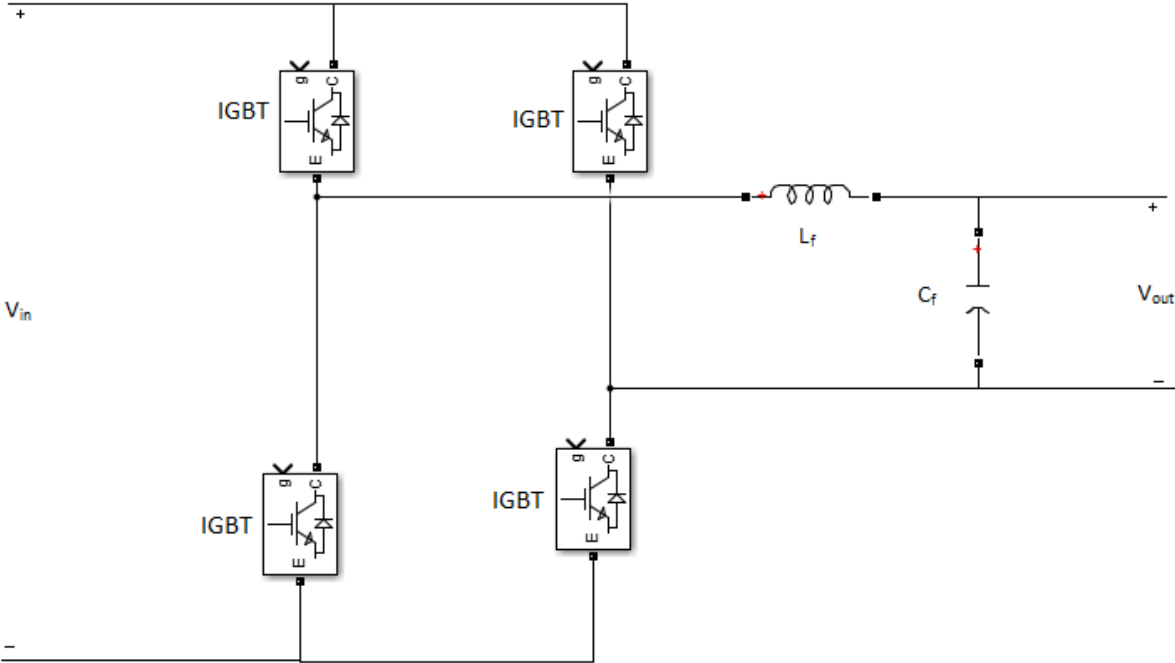


Figure C.2: Simulink Schematic of Single-phase Full-bridge Inverter

# C.4 Full-bridge Diode Rectifier with RC Load

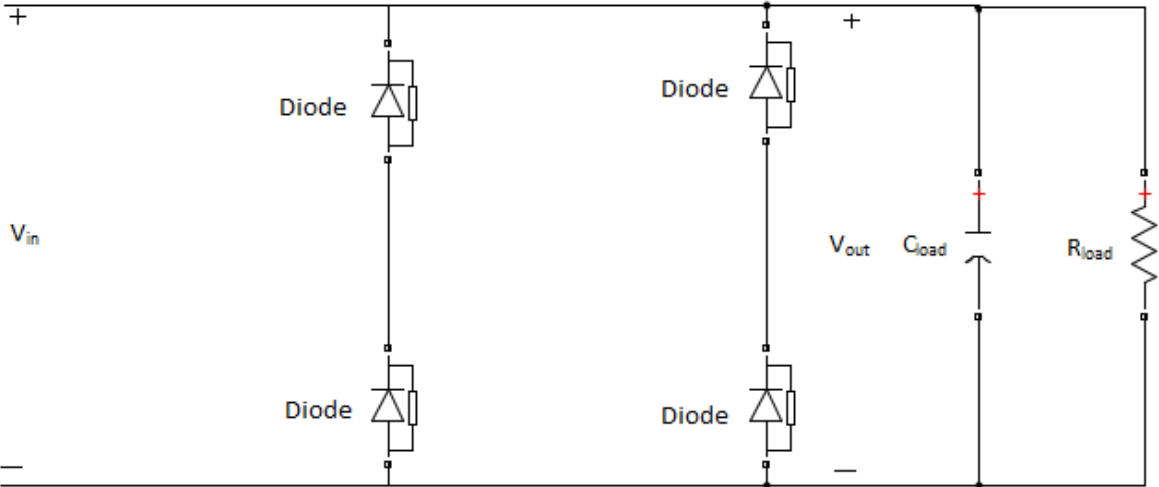


Figure C.3: Simulink Schematic of Full-bridge Diode Rectifier

# C.5 Modified Shunt APF Converter

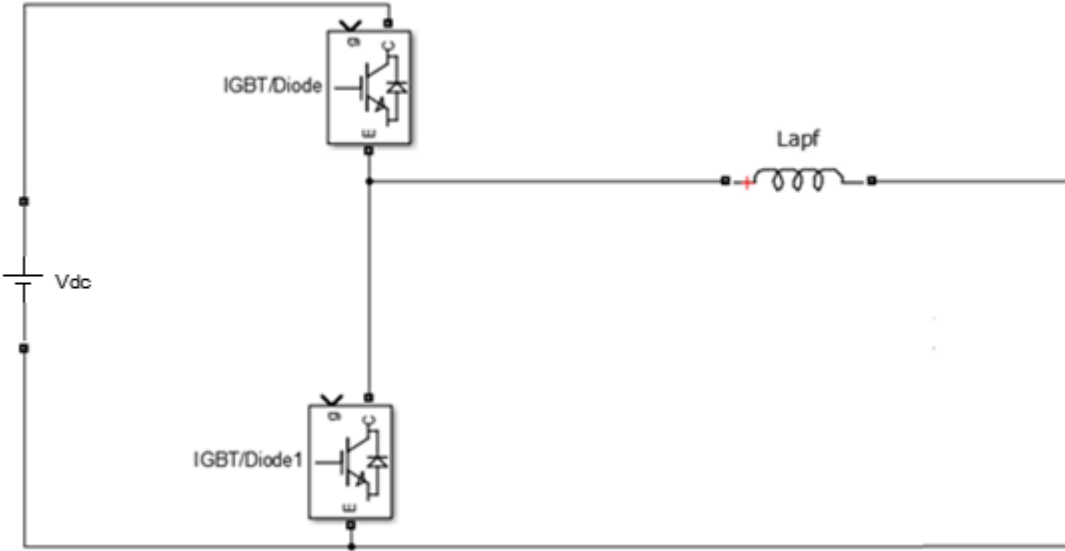


Figure C.4: Simulink Schematic of Modified Shunt APF Converter

# C.6 Fuel Cell Power System with Implemented Modified Shunt APF

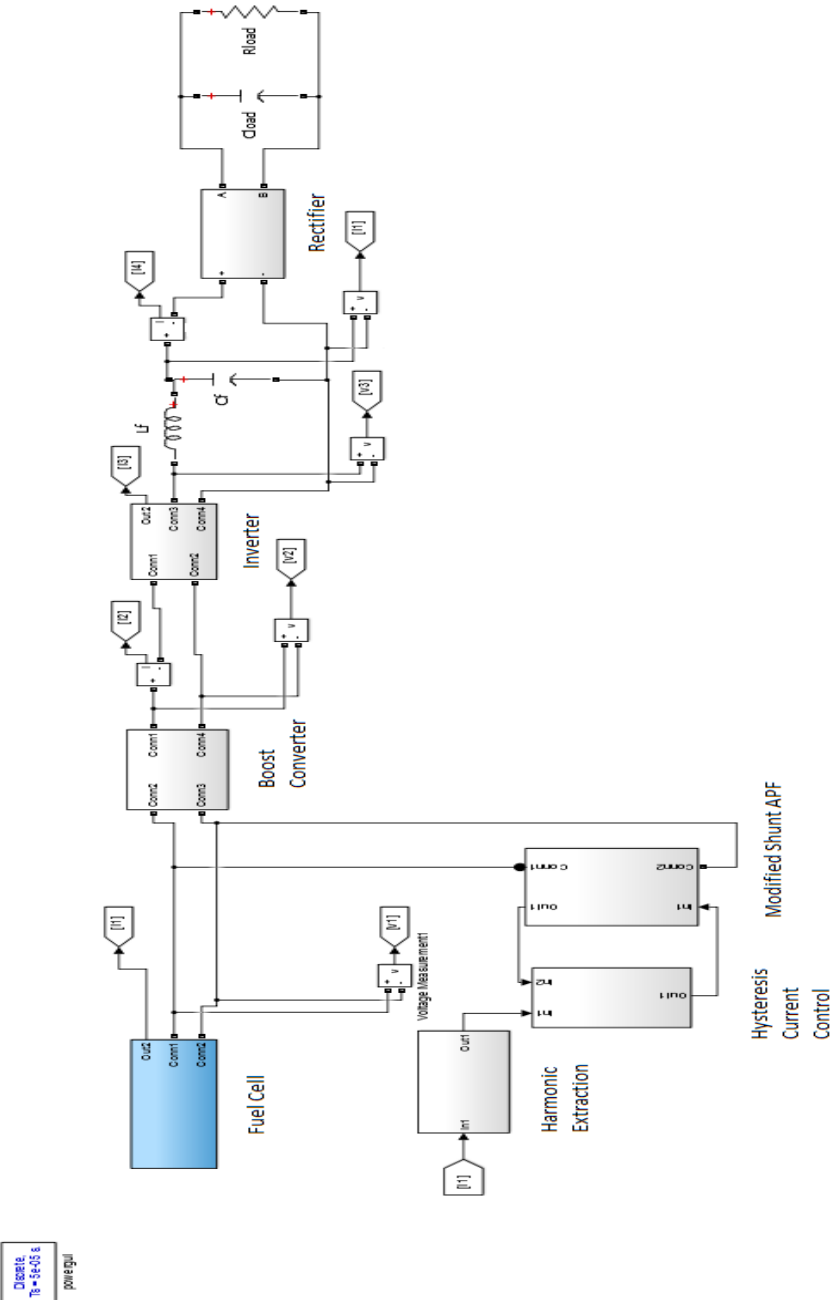


Figure C.5: Simulink Schematic of Fuel Cell System with Implemented Modified Shunt APF